UC San Diego
UC San Diego Electronic Theses and Dissertations

Title
Spatial and temporal modulation of internal waves and thermohaline structure

Permalink
https://escholarship.org/uc/item/2z9113n9

Author
Cole, Sylvia T.

Publication Date
2010

Peer reviewed|Thesis/dissertation

UNIVERSITY OF CALIFORNIA, SAN DIEGO

Spatial and temporal modulation of internal waves and thermohaline structure

A dissertation submitted in partial satisfaction of the
requirements for the degree
Doctor of Philosophy

in

Oceanography

by

Sylvia T. Cole

Committee in charge:

       Professor Daniel L. Rudnick, Chair
       Professor Michael Landry
       Professor Stefan Llewellyn-Smith
       Professor Lynne Talley
       Professor William R. Young

2010

The dissertation of Sylvia T. Cole is approved, and it is acceptable in quality and form for publication on microfilm and electronically:

_____

_____

_____

_____

_____
Chair

University of California, San Diego

2010

iii

TABLE OF CONTENTS

LIST OF FIGURES AND TABLES

ACKNOWLEDGEMENTS

I would like to thank Dan Rudnick for his encouragement, comments, and guidance. He was always willing to help and did not give up until I had it right. In particular, his patience and dedication to teaching me to write well stand out.

I would like to thank all of my committee members for their time and comments. Their questions and suggestions have improved this thesis, and they have always been available when needed. I would like to acknowledge the efforts of the Instrument Development Group at Scripps Institution of Oceanography and its director Russ Davis for building, deploying, operating, and recovering the Spray gliders used in Chapter 4. I would also like to acknowledge those involved with collecting and publicizing the additional data used in this thesis, oxygen observations at station ALOHA and along 152°W as well as sea surface temperature and salinity.

Chapter 2, in full, is a reproduction of the material as it appears in the Journal of Physical Oceanography, 2009, by S. T. Cole, D. L. Rudnick, B. A. Hodges, and J. P. Martin, Vol. 39, pp. 421-436. The dissertation author was the primary investigator and author of this paper. I would like to thank the American Meteorological Society for permission to include it in this thesis.

Chapter 3, in full, is a reproduction of the material as it appears in the Journal of Geophysical Research Oceans, 2010, by S. T. Cole, D. L. Rudnick, and J. A. Colosi, Vol. 115, C04012. The dissertation author was the primary investigator and author of this paper. I would like to thank the American Geophysical Union for permission to include it in this thesis.

Chapter 4, in part, is currently being prepared for submission for publication of the material. S. T. Cole and D. L Rudnick. The dissertation author was the primary investigator and author of this paper.

VITA

2004	B.S., Physics, University of Maryland at College Park
2004-2010	Graduate student researcher, Scripps Institution of Oceanography, University of California, San Diego
2010	Ph.D., Oceanography Scripps Institution of Oceanography, University of California, San Diego

PUBLICATIONS

Cole, S. T., D. L. Rudnick, and J. A. Colosi, 2010: "Seasonal evolution of upper ocean horizontal structure and the remnant mixed layer." *J. Geophys. Res.*, C04012, doi:10.1029/2009JC005654.

Cole, S. T., D. L. Rudnick, B. A. Hodges, and J. P. Martin, 2009: "Observations of tidal internal wave beams at Kauai Channel, Hawaii." *J. Phys. Oceanogr.*, 39, 421-436.

FIELDS OF STUDY

Major Field: Physical Oceanography

Studies in Descriptive Physical Oceanography
Professors M. C. Hendershott, P. E. Robbins, D. H. Roemmich, and
L. D. Talley

Studies in Fluid Dynamics and Turbulence
Professors S. Sarkar and C. D. Winant

Studies in Geophysical Fluid Dynamics
Professors P. Cessi and R. Salmon

Studies in Linear and Nonlinear Waves

Professors R. T. Guza, M. C. Hendershott, and W. K. Melville

Studies in Applied Mathematics
Professors G. Ierley, D. Tartakovsky, and W. R. Young

Studies in Data Analysis
Professors S. Gille, R. Pinkel, and D. L. Rudnick

Studies in Oceanographic Instrumentation
Professor U. Send

Studies in Biological Oceanography
Professor P. J. S. Franks

Studies in Atmospheric Physics
Professor J. Norris

ABSTRACT OF THE DISSERTATION

Spatial and temporal modulation of internal waves and thermohaline structure

by

Sylvia T. Cole

Doctor of Philosophy in Oceanography

University of California, San Diego, 2010

Professor Daniel L. Rudnick, Chair

Repeated horizontal sections at tidal and seasonal timescales are analyzed and show the two-dimensional (x-z) spatial patterns of internal waves and thermohaline structure. These spatial patterns give information about internal wave properties on tidal timescales, and the history of stirring and mixing on seasonal timescales.

The across-ridge structure of tidal internal waves at Kauai Channel, Hawaii was observed using 300 km SeaSoar and Doppler sonar sections perpendicular to the Hawaiian ridge. M_2 tidal beams and their reflection off of the surface were observed in velocity and displacement variance and several covariances. Covariances were

consistent with internal wave generation at the ridge flanks and corresponded to internal wave propagation away from the ridge. Energy flux was found to exceed dissipation almost everywhere across the ridge. Interactions between upward and downward tidal beams are shown to cause momentum flux divergences and mean flows.

The seasonal evolution of upper ocean thermohaline structure was studied using observations of a North Pacific section taken in winter, spring, and summer with 3-14 km horizontal resolution. In the mixed layer, seasonal modulations in the size of horizontal temperature and salinity differences as well as their tendency to compensate in density were observed. Water left behind after the mixed layer restratified inherited its thermohaline structure from the winter mixed layer, was most similar to the mixed layer in spring, and to the region just below in summer. Spectra of isopycnal depth and temperature showed seasonal variations at 30-370 km wavelengths. Effective isopycnal diffusivity was estimated by treating salinity anomalies as a tracer.

Thermohaline structure at 5-1300 km scales in the upper 1000 m was analyzed along a section north of Hawaii observed 16 times with autonomous gliders over 2.5 years. A spatial modulation of thermohaline fluctuations along isopycnals was observed that persisted over the observation period and reflects the history of horizontal stirring and mixing. Temporal modulations in thermohaline structure were observed in the mixed layer, including the subtropical frontal regions, and the water left behind after restratificaiton, where perturbation magnitude decayed with time once isolated from the mixed layer.

Chapter 1

Introduction

The distribution of properties throughout the global ocean, which influences our climate, is affected by a wide range of processes including stirring and mixing that take place at smaller horizontal scales. Stirring occurs when property gradients are stretched and folded on scales from meters to 1000's of kilometers. The ocean is stirred by global scale and basin scale currents such as the meridional overturning circulation and ocean gyres, mesoscale features such as closed eddies and the meandering of ocean fronts, and submesoscale features such as filaments and the edges of eddies. Mixing occurs when water properties such as heat and salt are exchanged on molecular and slightly larger scales. In numerical models, the effects of processes like horizontal stirring and mixing that occur at scales smaller than the model resolution are parameterized (Dimotakis 2005; Garrett 2006). At the scale of contemporary regional and global models, 10-100 km, the effects of internal waves that enhance vertical mixing as well as and mesoscale and submesoscale features that enhance horizontal stirring and mixing are not always resolved. The incomplete understanding of the net effects of smaller-scale ocean features causes a large uncertainty in predicting future climate with numerical models: this dissertation adds to our understanding of these smaller-scale ocean processes.

Internal waves and thermohaline structure are analyzed from repeated

horizontal sections. Horizontal sections through the ocean allow the spatial structure and statistics of small-scale features to be determined. Repeated sections allow the time evolution of these features and statistics to be analyzed. We consider sections repeated on the tidal and seasonal timescale, with these timescales determined by instrument capabilities and phenomena of interest. Three different instruments were used to collect the observations in this thesis: SeaSoar, which is a towed platform (Pollard 1986); an underway conductivity-temperature-depth instrument (UCTD), which is dropped and recovered from a moving ship (Rudnick and Klinke 2007); and Spray gliders, which are autonomous platforms (Sherman et al. 2001; Rudnick et al. 2004). All three instruments provide observations at a horizontal resolution of 3-14 km, allowing smaller-scale features to be studied. At the tidal timescale, the internal wave energy cascade that concludes in vertical mixing is studied from 18 repeated SeaSoar sections across the Hawaiian ridge (Ch. 2). At the seasonal timescale, stirring, mixing and the history of the water are addressed from three repeated SeaSoar and UCTD sections taken in late winter, late spring, and late summer (Ch. 3) as well as 16 repeated Spray glider sections taken over 2.5 years (Ch. 4). At tidal and seasonal timescales, the approach is similar but the phenomena studied are different.

Chapter 2 addresses the internal wave energy cascade and its spatial structure. Internal waves, which are vertical oscillations of density surfaces, are found throughout the ocean at all latitudes, longitudes, and depths (Garrett and Munk 1979). Internal waves have an interesting spatial modulation as they propagate in three dimension (x, y, and z) in spatially compact regions of energy called internal wave

beams (Mowbray and Rarity 1967; Prinsenberg et al. 1974; Sutherland et al. 2000). Internal waves are generated by basin scale tides and winds, and then propagate throughout the ocean before dissipating into turbulence. The transfer of energy from basin-scale motions to kilometer-scale motions to turbulence is referred to as the internal wave energy cascade. Internal waves supply the energy needed to maintain open ocean stratification with approximately equal contributions from tidal and wind sources (Munk and Wunsch 1998). For tidal sources, analysis of satellite altimetry observations have shown that energy is transferred to tidal internal waves near topography (Egbert and Ray 2001). Open questions include 1) how much is dissipation elevated over open ocean values near the generation sites, and 2) what fraction of the energy transferred to internal waves propagates into the open ocean to dissipate (Garrett and Kunze 2007). The Hawaiian Ocean Mixing Experiment (Rudnick et al. 2003), which included the observations in Ch. 2, was designed to address these questions. The repeated horizontal sections presented show the spatial structure of tidal internal wave beams and the energy cascade.

Chapters 3 and 4 address 5-1300 km scale thermohaline structure. Thermohaline structure refers to temperature (θ) and salinity (S) fluctuations on depth or density surfaces. At the surface of the ocean, θ-S fluctuations are primarily created by evaporation, precipitation, and heat fluxes, and are then enhanced by horizontal stirring and weakened by horizontal mixing. θ and S may or may not compensate in their effects on density. Below the surface, θ-S fluctuations are found on depth and density surfaces. On density surfaces, θ-S fluctuations are commonly referred to as

spice flucutaions as they are exactly compensated in density with hot and salty water next to cold and fresh water (Veronis 1972; Munk 1981). θ or S on density surfaces has been examined for decades at the basin scale providing information about basin-scale circulation (eg. Reid 1997). Spice is a tracer that is both passive and conservative, and reflects the history of horizontal stirring and mixing.

Seasonal modulations in thermohaline structure are addressed from sections repeated at seasonal timescales. At the surface, seasonal changes in the amount of solar heating affect the strength of winds blowing over the ocean and the heat input to the upper ocean. Wind strength affects the depth of the mixed layer, with deepest mixed layers and strongest winds in winter and early spring. Mixed layer depths in subtropical oceans are approximately 10 m when shallow and 100-200 m when deepest. The upper 100-200 m is therefore seasonally modulated. Because of instrument limitations and the expense of ships, a small but growing number of observations can address the seasonal modulation of 10 km scale features including ship based studies (Strass et al. 1992; Joyce et al. 1998; James et al. 2002) and glider based studies (Davis et al. 2008; Glenn et al. 2008; Nicholson et al. 2008; Perry et al. 2008). The repeated sections analyzed in Ch. 3 and 4 add to these observations and show the temporal modulation of smaller-scale thermohaline structure in the upper ocean.

Spatial modulations in thermohaline structure can be treated like a tracer. The ocean contains many tracers, which are properties set at a specific location and then advected throughout the ocean while being stirred and mixed. Physical and

geochemical tracers, such as salinity or oxygen, have extrema over a specific region that indicates which parts of the ocean are connected by currents or mixing. The spatial structure of thermohaline fluctuations is a type of tracer for which regions with similar histories have similar fluctuation magnitudes. The spatial modulation can potentially show where perturbations were largest at the surface, where water was older, where stirring was largest, and where the largest gradients available to stir were located. The repeated sections analyzed in Ch. 4 show the characteristic spatial pattern (x-z) of thermohaline structure, and give information about horizontal stirring, mixing, and the history of the water. As glider observations become more numerous, the spatial modulation of thermohaline structure will continue to be studied.

Chapter 2

Observations of Tidal Internal Wave Beams at Kauai Channel, Hawaii

Abstract of Chapter 2

To observe the across-ridge structure of internal tides, density and velocity were measured using SeaSoar and a Doppler sonar over the upper 400-600 m of the ocean extending 152 km on each side of the Hawaiian Ridge at Kauai Channel. Eighteen sections were completed in about 18 days with sampling intentionally detuned from the lunar semi-diurnal (M_2) tide so that averaging over all sections was equivalent to phase averaging the M_2 tide. Velocity and displacement variance and several covariances involving velocity and displacement showed one M_2 internal wave beam on each side of the ridge and reflection of the beams off of the surface. Theoretical ray slopes aligned with the observed beams and originated from the sides of the ridge. Energy flux was in agreement with internal wave generation at the ridge. Inferred turbulent dissipation was elevated relative to open ocean values near tidal beams. Energy flux was larger than total dissipation almost everywhere across the ridge. Internal wave energy flux and dissipation at Kauai Channel were 1.5-2.5 times greater than the average location along the Hawaiian Ridge. The upper 400-600 m was about 1/3 to 1/2 as energetic as the full depth ocean. Tidal beams interact with each other over the entire length of the beams causing gradients along beams in almost all

covariances, momentum flux divergences, and mean flows. At Kauai Channel, momentum flux divergences corresponded to mean flows of 1-4 cm s^{-1}.

2.1 Introduction

Vertical mixing in the deep ocean, which keeps the ocean stratified and helps to maintain global overturning circulation, is primarily accomplished by the dissipation of internal waves. Internal waves are forced by basin-scale winds and tides and dissipate energy to small-scale turbulence. Tidal and wind dissipation are estimated to be of roughly equal importance to maintaining open ocean stratification (Munk and Wunsch 1998; Wunsch and Ferrari 2004; Garrett and Kunze 2007). We focus on the tidal energy cascade, from basin-scale barotropic tides to internal waves to turbulence, because tides have discrete frequencies that are convenient to observe. The lunar semi-diurnal (M_2) tide is the dominant frequency of the barotropic tide over most of the ocean.

Internal waves of tidal frequency, or internal tides, are generated by the barotropic tide flowing over topography, propagate as internal wave beams, and dissipate over large distances. Flow of the barotropic tide over any topographic slope, such as continental shelves, ridges, and seamounts, generates internal tides. The amount of energy transferred to internal tides is largest for topography occupying a large fraction of the water column, topographic slope equal to or exceeding internal wave slope, and strong barotropic tides (Holloway and Merrifield 1999; Khatiwala 2003; Llewellyn-Smith and Young 2003; Munroe and Lamb 2005; Legg and Huijts

2006). Theoretical, numerical, and laboratory studies have shown that internal tides propagate as internal wave beams, spatially compact and coherent regions of energy with slopes that depend on frequency (Mowbray and Rarity 1967; Prinsenberg et al. 1974; Sutherland et al. 2000; Merrifield and Holloway 2002; Llewellyn-Smith and Young 2003; Khatiwala 2003; St Laurent et al. 2003; Legg and Huijts 2006). Internal tides are susceptible to dissipation and energy transfer to other frequencies, particularly at surface and bottom boundaries, the thermocline, or when intersecting other internal wave beams (Thorpe 1998; Sutherland 1999; Davies and Xing 2003; Lamb 2004; Tabaei et al. 2005; Gerkema et al. 2006a; Gerkema et al. 2006b). Internal tide dissipation occurs over hundreds to thousands of kilometers (Dushaw et al. 1995; Ray and Mitchum 1996; Egbert and Ray 2001; Lozovatsky et al. 2003). Large-scale velocity and density fields vary over this distance, changing the direction of wave propagation and decreasing coherence along a beam (Müller 1976; Rainville and Pinkel 2006b).

Internal wave beams generated by tidal flow over topography have been observed. Full depth measurements with coarse horizontal resolution provide evidence of M_2 tidal beams over 50-100 km horizontal distances (Pingree and New 1989; Pingree and New 1991; Althaus et al. 2003). Finely spaced horizontal measurements have captured 5-15 km segments of M_2 tidal beams (Lueck and Mudge 1997; Petruncio et al. 1998; Lien and Gregg 2001; Kitade and Matsuyama 2002; Lam et al. 2004) and segments at Kauai Channel, Hawaii of 50 km (Martin et al. 2006) and 20 km (Nash et al. 2006). The previous studies have collectively observed internal wave

beams in several quantities including: displacement and velocity magnitude, internal wave phase, turbulent kinetic energy density, energy flux, velocity shear, and turbulent dissipation.

We will show observations of internal wave beams along one section across the Hawaiian Ridge. The Hawaiian Ridge is an efficient generator of internal tides because of steep topography and barotropic tidal flows perpendicular to the ridge. The Hawaii Ocean Mixing Experiment (HOME) focused on how internal tide properties varied along and across the ridge. The locations with largest internal tide energy and dissipation were: French Frigate Shoals, west of Nihoa Island, and Kauai Channel (Merrifield and Holloway 2002; Klymak et al. 2006; Lee et al. 2006; Martin et al. 2006). This paper uses observations at Kauai Channel, the most geographically convenient location with enhanced energy and dissipation. One section across the ridge was repeatedly observed with timing intentionally detuned from the M_2 tide so that the M_2 tide could be phase averaged. A representative picture was obtained of the across-ridge structure of internal wave propagation and dissipation over a substantial potion of a tidal beam.

The remainder of this paper is constructed as follows. Section 2.2 presents the observations. Section 2.3 discusses velocity variance, displacement variance, velocity shear, and turbulent dissipation. The relationship between the tidal beams and topography is determined. Section 2.4 focuses on covariances, including energy flux, momentum flux, and interactions between tidal beams. The relationships between internal wave energy density, energy flux, and dissipation are discussed. Conclusions

are presented in Section 2.5.

2.2 Observations and Methods

From 2-19 October 2002, SeaSoar and a Doppler sonar were used to measure velocity and density along one section across the ridge. The 50 kHz Doppler sonar gave usable velocity data from 45-585 m. SeaSoar is a towed platform that cycled from 20-400 m in less than 12 minutes and had a horizontal resolution finer than 3.3km. The M_2 frequency was the dominant frequency at the Hawaiian Ridge, and the desired horizontal coverage was one wavelength of a mode one M_2 internal wave, 150 km, on each side of the ridge. With a towing speed for SeaSoar of 4 m s^{-1}, less than 90 km could be traveled in half an M_2 period and tidal frequencies were not resolved. A range of tidal phase was observed by completing eighteen sections along a 304 km track (Fig. 2.1). The center of the cruise track was roughly the midpoint of the ridge. The sections were intentionally timed to detune from the M_2 tide. The sampling pattern was successful, with observations within 152 km of the ridge crest approximately equally spaced in tidal phase (Fig. 2.2). Averaging over all sections (i.e. averaging in the vertical in Fig. 2.2) approximates averaging over M_2 phase.

SeaSoar and Doppler sonar observations were processed according to Martin et al. (2006). The 24 Hz raw SeaSoar density measurements were averaged into one-second records, and then SeaSoar and Doppler sonar data were averaged into 12-minute profiles. Profiles had an 8.6 m constant vertical spacing. Horizontal spacing averaged over all profiles was 2.81 km with a standard deviation of 0.22 km.

An across-ridge (x, positive toward northeast), along-ridge (y, positive toward northwest), vertical (z, positive upwards) coordinate system is aligned with the direction of the cruise track, 34.2°T. The cruise track was chosen based on topography and models to coincide with the direction of maximum energy flux (Merrifield and Holloway 2002). A sample section during spring tide shows that across-ridge velocity was stronger than along-ridge velocity and both were largest within 100 km of the ridge (Fig. 2.3). Velocity was surface-intensified but commonly greater than 10 cm s^{-1} at all depths. Large internal waves were observed throughout the section. M_2 internal wave ray paths calculated from linear theory are shown and discussed further in Section 2.3.

We perform an average over all sections and into 8 km horizontal bins, denoted by $\langle \ \rangle$, maintaining the 8.6 m vertical spacing. Density bins from 45-330 m and all velocity bins contained 40-55 observations within 152 km of the ridge. All bins with less than 25 observations were ignored. Perturbations from the average are denoted as primed variables, for example, $v' = v - \langle v \rangle$, where v is along-ridge velocity. Displacement, ζ', is the deviation of each isopycnal from its mean depth. Barotropic fields were not removed from the perturbation fields in any way. Averaged quantities have time scales larger than 18 days. Perturbations have time scales shorter than 18 days, and include semi-diurnal, diurnal, and inertial motions. Mean buoyancy frequency, $\langle N^2 \rangle$, was largest at the base of the mixed layer, which was in the upper 100m, and decreased below the mixed-layer base (Fig. 2.4). Mean density, $\langle \rho \rangle$, had horizontal density gradients, which were presumably in geostrophic balance as they

persisted for at least 18 days.

2.3 Variance

2.3.1 Velocity and Displacement Variance

Total velocity variance, $\left\langle (u')^2 + (v')^2 \right\rangle$, and displacement variance, $\left\langle (\zeta')^2 \right\rangle$ had

some similarities in across-ridge structure (Fig. 2.5). Velocity and displacement

variance were largest on either side of the ridge crest (x=0 km) and approximately

symmetric in pattern and magnitude about the ridge crest. Both had a minimum over

the ridge crest that was widest near the surface. Below 400 m, velocity variance was

elevated over the ridge crest. Velocity variance was surface intensified and

displacement variance was large deeper in the water column because density surfaces

are displaced by a larger amount where N^2 is smaller. Many regions of elevated

velocity and displacement variance coincided with each other. There were locations

where either velocity or displacement variance was elevated, such as at ±125 km.

M$_2$ ray slopes coincided with regions of elevated velocity and displacement

variance. The ray slope, $|\mu|$, a consequence of the internal wave dispersion relation, is:

$$\frac{dx}{dz} = \sqrt{\frac{\left\langle N^2 \right\rangle - \omega^2}{\omega^2 - f^2}} \tag{2.1}$$

with constant Coriolis parameter, f, and $2\pi/\omega$=12.42 h for the M$_2$ frequency. A

distinction will be made between the terms "tidal beam" and "ray path or ray slope".

"Ray path or ray slope" will refer to the curve calculated from (2.1). "Tidal beam" will

refer to features of velocity or density fields that coincide with a ray path. Tidal beams

have a width and amplitude while ray paths do not. M_2 ray slopes were placed in the horizontal to coincide best with total velocity variance (Fig. 2.5a). These ray paths are repeated in subsequent figures placed at the same location to facilitate comparisons between figures and with theoretical M_2 ray slopes. The region of low variance directly over the ridge corresponded to the region between the ray paths. Regions with largest variance were consistent with M_2 ray paths and are M_2 tidal beams. Both velocity and displacement variance showed M_2 tidal beams and their reflection off of the surface. Considering individual sections (for example, Fig. 2.3 during spring tide), ray slopes agreed well with observed features. Locations where either velocity OR displacement variance were elevated, such as ± 125 km, were far from the M_2 ray paths and did not correspond to tidal beams as variances were mainly vertically coherent. Only M_2 beams were apparent even though velocity and displacement variance included all frequencies less than 18 days. The M_2 frequency could have been dominant for two reasons: 1) M_2 motions had larger amplitudes than other motions, such as diurnal and near-inertial motions, and 2) the sampling pattern allowed for effective averaging over M_2 phase, but not over diurnal or near-inertial phase.

Ray paths were extended below 355 m to determine their relationship with the topography. Ray slopes below 355 m were calculated using the mean buoyancy frequency of HOME (Klymak et al. 2006). Ray paths intersect the sides of the ridge (Fig. 2.6), consistent with internal wave generation at the ridge (Baines 1982; Holloway and Merrifield 1999; Lamb 2004; Petrelis et al. 2006).

2.3.2 Velocity Shear and Turbulent Dissipation

Mean-square vertical shear of horizontal velocity, $\left\langle (u_z)^2 \right\rangle + \left\langle (v_z)^2 \right\rangle$, was elevated near the ridge. Velocity shear was largest in the upper ocean and decayed away from the ridge at all depths (Fig. 2.7a). Beams in velocity shear were harder to distinguish than in velocity variance. Mean-square shear from mean velocity was less than one tenth of mean-square shear from velocity perturbations.

Velocity shear is used to parameterize the turbulent dissipation rate, ε, and diapycnal eddy diffusivity, K_ρ. Along the Hawaiian Ridge, dissipation from microstructure measurements agreed better with parameterizations from Gregg (1989) (within a factor of 2 for K_ρ) than with Gregg et al. (2003) both with and without shear-strain ratio and latitude factors (Martin and Rudnick 2007). From Gregg (1989):

$$\varepsilon = 6.73 \cdot 10^{-10} \frac{N^2}{N_0^2} \left(\frac{S_{OBS}^2}{S_{GM}^2} \right)^2$$

$$K_\rho = 0.2 \frac{\varepsilon}{N^2} \tag{2.2}$$

where $N_0 = 5.24 \cdot 10^{-3}$ s^{-1} is a reference buoyancy frequency, S_{GM} is the total variance in vertical shear for the Garrett-Munk (GM) spectrum at wavelengths less than 10 m (Cairns and Williams 1976; Gregg and Kunze 1991), and S_{OBS}^2 is the observed vertical shear (Fig. 2.7a) multiplied by a correction factor to account for averaging from the Doppler sonar (Martin and Rudnick 2007).

Dissipation and diffusivity were elevated relative to open ocean values (Fig. 2.7b-c). Maximum values below 95 m were $1.3 \cdot 10^{-7}$ W kg^{-1} and $3.6 \cdot 10^{-4}$ m^2 s^{-1}

compared with open ocean values of 10^{-10} W kg^{-1} and 10^{-5} m^2 s^{-1} respectively. Both quantities decayed to open ocean values tens of kilometers from the tidal beams. Tidal beams were most apparent in K_ρ (Fig. 2.7c) because of appropriate scaling by N^2.

2.3.3 Variance Ratios

Energy density and shear-strain ratios give information about the frequency content of internal waves. For a hydrostatic two-dimensional inviscid plane wave or internal wave, denoted by ^ variables, energy density and shear-strain ratios are:

$$\frac{\left\langle (\hat{u})^2 + (\hat{v})^2 \right\rangle}{\left\langle N^2 \right\rangle \left\langle (\hat{\xi})^2 \right\rangle} = \frac{\left\langle (\hat{u}_z)^2 + (\hat{v}_z)^2 \right\rangle}{\left\langle N^2 \right\rangle \left\langle (\hat{\xi}_z)^2 \right\rangle} = \frac{\omega^2 + f^2}{\omega^2 - f^2} \qquad (2.3)$$

which is 1.34 for the M_2 frequency, where $\frac{1}{2}\rho_0 \left\langle N^2 \right\rangle \left\langle (\hat{\xi})^2 \right\rangle$ is potential energy density,

$\frac{1}{2}\rho_0 \left\langle (\hat{u})^2 + (\hat{v})^2 \right\rangle$ is kinetic energy density, and $\left\langle N^2 \right\rangle \left\langle (\hat{\xi}_z)^2 \right\rangle$ is vertical strain

(Fofonoff 1969; Lien and Müller 1992). ρ_0=1026 kg m^{-3} is a reference density used throughout this analysis. Energy density and shear-strain ratios have a value of 3 for a GM spectrum of internal waves (Munk 1981). Observations of internal tides at the Hawaiian ridge (Lee et al. 2006; Martin et al. 2006) and other locations (Toole et al. 1997; Kunze et al. 2002) have corresponded to the M_2 frequency for both ratios in (2.3).

The observed shear-strain ratio showed that the M_2 frequency was dominant. A scatter plot of vertically integrated shear versus strain clustered around the M_2 ratio from (2.3) (Fig. 2.8). There was little variation in the ratio even though locations

where beams had been observed (within 68 km of the ridge; Figs. 2.5-2.6) and where

beams had not been observed (68-152 km from the ridge) were included, as well as

locations north and south of the ridge. Integrated shear and strain was largest where

beams were observed. The energy density ratio (not shown) also clustered around the

M_2 ratio, but had more scatter as it contained larger vertical scales. Larger vertical

scales include variability such as geostrophic motions and barotropic tides in addition

to internal waves. The M_2 energy density and shear-strain ratios were consistent with

our observations of M_2 tidal beams and other HOME observations showing increased

energy at the M_2 frequency (Aucan et al. 2006; Rainville and Pinkel 2006a).

2.4 Covariances

Tidal beams were evident in several covariances (Figs. 2.9-2.10). $\langle u'\zeta' \rangle$,

$\langle u'\zeta'_x \rangle$, and $\langle u'_x\zeta' \rangle$ showed beams with equal magnitudes along all portions of the ray

paths (Figs. 2.9a, 2.10a-b). Beams in $\langle u'v'_x \rangle$ and $\langle u'_xv' \rangle$ were thinner and more

variable, and had strongest magnitudes along the portions of ray paths closest to the

ridge (Fig. 2.10c-d). $\langle u'\zeta' \rangle$, $\langle u'v'_x \rangle$, and $\langle u'_xv' \rangle$ had different signs north and south of

the ridge (Fig. 2.9a, 2.10c-d). $\langle u'\zeta'_x \rangle$ and $\langle u'_x\zeta' \rangle$ changed signs where the beams

reflected off of the surface (Fig. 2.10a-b). $\langle v'\zeta' \rangle$ was smaller in magnitude than $\langle u'\zeta' \rangle$

and did not have clear tidal beams (Fig. 2.9). Tidal beams in other covariances, such as

$\langle u'\zeta'_z \rangle$ or $\langle u'v'_z \rangle$, were evident but not as uniform as those in figures 2.9-2.10. These

phase-averaged observations clearly show tidal beams and changes in sign at the ridge

and upon reflection from the surface.

To interpret covariances, internal tides at Kauai Channel are modeled as linear, hydrostatic, two-dimensional, and inviscid. Nonlinear terms are neglected as the relevant non-dimensional parameter was at most 0.01 (Martin et al. 2006). The hydrostatic approximation is valid as $\omega^2/N^2 = O(10^{-4})$. Neglecting dissipation and along-ridge gradients, the basic equations of motion are:

$$u_t^* - fv^* = -\frac{1}{\rho_0}P_x^* \tag{2.4a}$$

$$v_t^* + fu^* = 0 \tag{2.4b}$$

$$0 = -\frac{1}{\rho_0}P_z^* - N^2\zeta^* \tag{2.4c}$$

$$\zeta_t^* = w^* \tag{2.4d}$$

$$u_x^* + w_z^* = 0 \tag{2.4e}$$

with the bottom boundary condition:

$$\left(u^* + \tilde{u}\right)\frac{dh}{dx} + \left(w^* + \tilde{w}\right) = 0 \tag{2.4f}$$

where P^* is the pressure perturbation, $h(x)$ is the boundary, $(\tilde{u},\tilde{w})$ are barotropic velocities, and asterisks distinguish theoretical fields, which are baroclinic, from observed perturbation fields, which include barotropic fields (Gill 1982). If motions with a single frequency are averaged over a complete cycle, covariances are independent of time: $\langle v^*v^* \rangle_t = \frac{1}{2}\langle v^*v_t^* \rangle = 0$ for example. Motions consistent with (2.4) and appropriately averaged over a tidal cycle will have $\langle u^*v^* \rangle = 0$ (multiply (2.4b) by

v^* and average) and $\langle u^* v_x^* \rangle = -\langle u_x^* v^* \rangle$. Observed $\langle u'v' \rangle$ was small in magnitude and did not have clear tidal beams (not shown), and only minor differences between $\langle u'v_x' \rangle$ and $-\langle u_x'v' \rangle$ were found (Fig. 2.10c-d) indicating that the dynamics of (2.4) are sensible, and that the observations and averaging procedure were adequate.

The barotropic tide is included in the observed perturbation fields but showed no clear effect on covariances. For a barotropic tide of the form $\tilde{u} = U_0 \cos(\omega t)$, $\langle \tilde{u}\tilde{u} \rangle$ is a background field with no beam pattern. Covariances between baroclinic fields and $\tilde{u}$, $\langle \tilde{u}\zeta_x^* \rangle$ for example, have beam patterns and may differ in sign from covariances with u^*. Magnitudes of u^* and $\tilde{u}$ are equal at the top of a ridge. As barotropic transport, $U_0 h(x)$, is constant because of mass conservation, $\tilde{u}$ becomes smaller than u^* as water depth increases and covariances involving the barotropic tide would have magnitudes dependent on water depth. The observed covariances, $\langle u'u' \rangle$, $\langle u'\zeta' \rangle$, $\langle u'\zeta_x' \rangle$, and $\langle u'v_x' \rangle$ (Figs. 2.5a, 2.9a, 2.10a, 2.10c), and variance ratios (Section 2.3.3, Fig. 2.8) showed no obvious dependence on water depth, so the barotropic tide did not apparently affect covariances. Observed covariances are interpreted as resulting from the baroclinic tide.

Velocity components parallel and perpendicular to the direction of wave propagation are uncorrelated. Along the cruise track, 34.2°T, the correlation of u' with v' was 0.1±0.3 over 95-585 m. Rotated along 31.7°T, the correlation was 0.0±0.3 over 95-585 m. North and south of the ridge, zero correlation was obtained for directions of 36.8°T and 27.0°T, respectively. The direction of internal wave propagation was

within eight degrees of the cruise track.

2.4.1 $\langle u'\zeta' \rangle$ *and Interactions Between Tidal Beams*

Tidal flow over steep topography generates upward and downward beams that can interact and covary with each other. Following Llewellyn-Smith and Young (2003), a streamfunction is introduced into (2.4) where $\tilde{u} = U_0 \cos(\omega t)$, $(u^*, w^*) = (-\psi_z, \psi_x)$, and:

$$\psi = U_o \mathrm{Re}\left[\phi(x,z)e^{-i\omega t}\right] = U_0\left[\phi^R \cos(\omega t) + \phi^I \sin(\omega t)\right]. \tag{2.5}$$

For a knife-edge ridge at $x=0$ with height h_0:

$$\phi^R = H(2\pi)^{-1}\sum_n n^{-1}A_n\left[\sin\left(nZ - n|X|\right) + \sin\left(nZ + n|X|\right)\right]$$

$$\phi^I = H(2\pi)^{-1}\sum_n n^{-1}A_n\left[\cos\left(nZ - n|X|\right) - \cos\left(nZ + n|X|\right)\right] \tag{2.6}$$

where X=πx/μH and Z=πz/H are non-dimensional variables, $n = 1,2,3...\infty$ is a mode number, and H is total water depth (Llewellyn-Smith and Young 2003). The coefficients A_n are determined from boundary conditions. ϕ^R and ϕ^I each contain two terms that correspond to beams with upward and downward energy flux. Using horizontal energy flux as an example, covariances have the form:

$\langle u^* P^* \rangle = \langle u_\uparrow^* P_\uparrow^* \rangle + \langle u_\downarrow^* P_\downarrow^* \rangle + \langle u_\uparrow^* P_\downarrow^* \rangle + \langle u_\downarrow^* P_\uparrow^* \rangle$, where brackets denote phase averaging, and subscript arrows refer to upward and downward beams. Covariances between components in the same vertical direction, for example $\langle u_\uparrow^* P_\uparrow^* \rangle$ and $\langle u_\downarrow^* P_\downarrow^* \rangle$, will be referred to as beams acting in isolation and are equivalent to a single beam extending

infinitely in one direction. Covariances between upward and downward components, for example $\langle u_\uparrow^* P_\downarrow^* \rangle$ and $\langle u_\downarrow^* P_\uparrow^* \rangle$, will be referred to as beam interactions. Beams traveling in different vertical directions can result from different beams, or the same beam that has reflected off of the surface or bottom. Beam interactions can occur for gently sloping topography, which generates only upward beams, provided beams reflect off of the surface. Interactions between beams are possible because there are oscillating fields within and far from each beam.

Energy flux is an illustrative example of beam interactions. A knife-edged ridge has four beams originating from the top of the ridge (x=0 km, z=3200 m), with one initially sloping upwards and one downwards on each side of the ridge (Fig. 2.11). Total energy flux (Fig. 2.11a) is largest along the tidal beams, positive north of the ridge, and negative south of the ridge. Energy flux from isolated beams is constant in magnitude along all of the beams (Fig. 2.11b). Energy flux from beam interactions varies in sign and magnitude along all of the beams and abruptly changes sign where two beams intersect (Fig. 2.11c). The magnitudes of energy flux from beam interactions and isolated beams are similar. Total energy flux (Fig. 2.11a) has gradients along each beam, which are largest where beams intersect, because of beam interactions.

$\langle u^* \zeta^* \rangle$ is zero for isolated beams but not for interacting beams. From (2.4)-(2.5), $\langle u^* \zeta^* \rangle = U_0^2 \omega^{-1} \left[-\phi_x^R \phi_z^I + \phi_z^R \phi_x^I \right]$, and is zero if $\left(\phi_z^R, \phi_z^I \right) \propto \left(\phi_x^R, \phi_x^I \right)$. For a single beam (for example, only the upward beams in (2.6)), as in a plane wave, horizontal and vertical derivatives are proportional and displacement and across-ridge velocity

are uncorrelated. Physically, internal wave oscillations parallel ray paths so that

maximum across-ridge and vertical displacements coincide and across-ridge velocity

is zero when vertical displacement is a maximum. With multiple beams, as in (2.6),

horizontal and vertical derivatives are not proportional and $\langle u^*\zeta^* \rangle \neq 0$. $\langle u^*\zeta^* \rangle$ is

largest along tidal beams and varies in magnitude and sign along tidal beams (Fig.

2.12) because the covariance is caused entirely by beam interactions.

The sign of $\langle u^*\zeta^* \rangle$ in the upper ocean (Fig. 2.12) agrees with observed $\langle u'\zeta' \rangle$

(Fig. 2.9a) suggesting that beam interactions are a reasonable explanation for the

observed covariance. A knife-edge ridge was used because this simple topography

leads to tractable solutions. A model with more realistic topography would have

covariances with different magnitudes, but similar signs. The processes of internal

wave propagation are essentially the same, so a knife-edge ridge is an adequate model.

2.4.2 Interpretation of $\langle u^*\zeta_x^* \rangle$ and $\langle u^*v_x^* \rangle$

$\langle u^*\zeta_x^* \rangle$, $\langle u_x^*\zeta^* \rangle$, $\langle u^*v_x^* \rangle$, and $\langle u_x^*v^* \rangle$ show the direction of energy flux along the

beams. For a knife-edge ridge, horizontal energy flux changes sign at the ridge and is

positive in the positive x-direction (Fig. 2.11a), and vertical energy flux changes sign

at surface and bottom reflections and is initially positive (negative) along upward

(downward) sloping beams (Fig. 2.13). $\langle u^*v_x^* \rangle$ and $-\langle u_x^*v^* \rangle$ (Fig. 2.14c-d) have the

same signs as horizontal energy flux (Fig. 2.11a), and $-\langle u^*\zeta_x^* \rangle$ and $\langle u_x^*\zeta^* \rangle$ (Fig. 2.14a-

b) have the same signs as vertical energy flux (Fig. 2.13). $\langle u^*\zeta_x^* \rangle$, $\langle u_x^*\zeta^* \rangle$, $\langle u^*v_x^* \rangle$, and

$\langle u_x^* v^* \rangle$ have barely perceptible gradients along the beams, in contrast to $\langle u^* P^* \rangle$ and

$\langle w^* P^* \rangle$, because beam interactions are an order of magnitude smaller than covariances

from isolated beams. The direction, but not the magnitude, of energy flux can be

obtained from $\langle u^* \zeta_x^* \rangle$, $\langle u_x^* \zeta^* \rangle$, $\langle u^* v_x^* \rangle$, and $\langle u_x^* v^* \rangle$. The observed covariances (Fig.

2.10) resemble the covariances for a knife-edged ridge in the upper ocean (Fig. 2.14)

in having: 1) the same sign and 2) only minor differences between $-\langle u' \zeta_x' \rangle$ and $\langle u_x' \zeta' \rangle$

as well as $\langle u' v_x' \rangle$ and $-\langle u_x' v' \rangle$. At Kauai Channel, horizontal energy flux was directed

away from the ridge (Fig. 2.10c-d), and vertical energy flux was initially upward

nearest the ridge and then downward after reflection off of the surface (Fig. 2.10a-b),

consistent with internal wave generation at the ridge.

2.4.3 Across-Ridge Energy Flux, $\langle u'P' \rangle$

Pressure perturbations were determined by fitting displacement to vertical

modes (Gill 1982). Using vertical modes enforces the constraint that pressure

perturbations vertically integrate to zero over the full ocean depth. Vertical modes

were calculated from full depth buoyancy frequency using observed horizontally

averaged buoyancy frequency above 355m and the mean buoyancy frequency of

HOME (Klymak et al. 2006) below 355 m. Velocity and displacement were fit to

baroclinic modes by minimizing a cost function that included measures of misfit and

magnitudes of the modal coefficients. The barotropic mode was not included in the fit.

Magnitudes of the modal coefficients were minimized so that pressure perturbations

did not become unrealistically large below 355m. Ten modes were used in the fit as vertically integrated energy flux using 4-10 modes was essentially the same (averaged across the ridge, the rms variation over modes 4-10 was 10% of the total), and ten modes showed the beam pattern better than four modes. Misfits between observed and fitted u' and ζ' averaged over all bins were 0.03 m s^{-1} and 3 m, respectively compared with magnitudes of 0.08 m s^{-1} and 9 m. Misfits were largely baroclinic and mainly had vertical scales smaller than can be represented with 10 modes. Including across-ridge variations in depth or N^2 did not change the results significantly.

Across-ridge energy flux was away from the ridge and largest along M_2 ray paths (Fig. 2.15a), consistent with internal wave generation at the ridge. Energy flux was meaningful over 50-355 m where observations of density perturbations were available, and over 0-50m because properties were uniform with depth in the mixed layer. The largest energy fluxes on both sides of the ridge occurred near the surface reflections of the ray paths. Vertically integrated energy flux is considered over two depth ranges: 0-335 m, which is the largest range with meaningful energy flux, and 95-355 m, which is below the mixed-layer base. Vertically integrated energy flux over 95-355 m and 0-355 m had reasonable magnitudes and across-ridge structures (Fig. 2.15b). Maximum energy flux integrated over 0-355 m was 6.7 kW m^{-1} and -4.7 kW m^{-1} north and south of the ridge respectively, compared to 3.5 kW m^{-1} and -2.3 kW m^{-1} over 95-355 m.

Errors in energy flux arose from several sources. A formal error in $\langle u'P' \rangle$ was estimated by assuming random errors in u' and ζ' equal to the magnitude of the

misfits between the observations and the fit to modes. For vertically uncorrelated

errors in u' and ζ', the formal error was 0.25 kW m^{-1} over 95-355 m, and 0.39 kW m^{-1}

over 0-355 m. Some portion of barotropic energy flux might have been included in

$\langle u'P' \rangle$ because the barotropic mode is not orthogonal to the baroclinic modes in the

upper ocean. For vertically correlated errors in u' and ζ', the formal error in energy

flux was 1.14 kW m^{-1} over 95-355 m and 1.74 kW m^{-1} over 0-355 m. Greater than 100

km from the ridge, energy flux was typically 1-2 kW m^{-1} and might have resulted from

non-tidal mesoscale features.

2.4.4 Relationships between Energy Density, Energy Flux, and Dissipation

Energy density and energy flux were correlated (Fig. 2.16a). For each vertical

mode, energy flux equals energy density multiplied by group velocity (Klymak et al.

2006; Alford and Zhao 2007). Observed vertically integrated energy flux was

regressed against vertically integrated energy density to find a horizontal group

velocity of 0.92 m s^{-1} directed away from the ridge (Fig. 2.16a). There was no obvious

difference in the magnitude of the group velocity north and south of the ridge. The

theoretical group velocity of the third mode and the average group velocity of the first

eight modes were both equal to 0.91 m s^{-1}, agreeing well with the observed 0.92 m s^{-1}.

Energy flux and dissipation varied across the ridge in different ways and are

compared through the decay length scale. Tidal beams in dissipation (Fig. 2.7b) were

less uniform than in energy flux (Fig. 2.15a) and harder to distinguish, particularly for

the beams farthest from the ridge. The minimum over the ridge crest between the tidal beams was clearer in energy flux than in dissipation. Velocity shear and dissipation fields represent smaller vertical scales than energy flux fields, which may explain some of these differences. The decay length scale, $\left|\int \langle u'P'\rangle dz\right| \Big/ \int \rho_0 \langle \varepsilon \rangle dz$, is the distance an internal wave must propagate for its total dissipation to equal initial energy flux. Energy flux was integrated over 0-355 m, and dissipation over 95-355 m because the parameterization is not valid in the mixed layer. Averaged within 52 km of the ridge, the decay length scale was 380 km with a standard deviation of 340 km. The largest decay length scales north and south of the ridge were 2550 km and 850 km, respectively, at the locations of largest energy flux. Even though the decay length scale varied across the ridge, it was similar to previous estimates at Kauai Channel of 400-1000 km for the M_2 frequency (Lee et al. 2006).

Dissipation and energy density were correlated as previously observed (Klymak et al. 2006; Lee et al. 2006; Martin and Rudnick 2007). A correlation results because dissipation is proportional to energy flux through the decay length scale and energy flux for each mode is the product of energy density with group velocity. From full depth observations and models along the Hawaiian Ridge,

$$\int \rho_0 \langle \varepsilon \rangle dz \sim \left(\int 0.5 \rho_0 \left(\langle N^2 \rangle \langle (\xi^*)^2 \rangle + \langle (u^*)^2 \rangle + \langle (v^*)^2 \rangle \right) dz \right)^P \text{ where P=1±0.5 (Klymak et }$$

al. 2006). In our observations, energy density and energy flux (Figs. 2.5, 2.15a, 2.16a) were correlated better than energy flux and dissipation (Figs. 2.7b, 2.15a). With integration over 95-355 m, P=1.3 (Fig. 2.16b). This differed from the estimate at

Kauai Channel of $P=0.7\pm0.2$ made during spring tide in 2000 (Martin and Rudnick 2007), but both were within the uncertainty of the Klymak et al. (2006) value.

Dissipation and energy flux in the upper ocean are extrapolated to the Hawaiian Ridge using a 2500 km ridge length as in Martin and Rudnick (2007). Outward energy flux was elevated near where beams were observed with maximum values in the upper 355m of 16.8 GW and 11.8 GW north and south of the ridge, respectively (Fig. 2.16c). Dissipation over 95-355 m depth was integrated from the ridge crest outward, and so increased from zero to 1.6 GW and 1.5 GW at -152 km and 152 km from the ridge, respectively. Energy flux was almost everywhere larger than total dissipation. Averaged within 52 km of the ridge crest,

$\iint \rho_0 \langle \varepsilon \rangle dxdz \Big/ \left| \int \langle u'P' \rangle dz \right|$, a measure of the radiation efficiency, was 0.16 with a

standard deviation of 0.15. The radiation efficiency was similar to previous full depth M_2 estimates of 0.10 at Kauai Channel, and 0.08-0.25 along the Hawaiian Ridge (Klymak et al. 2006; Nash et al. 2006).

The observed dissipation and outward energy flux are compared to the 20 ± 6 GW of energy believed lost from the barotropic tide at the Hawaiian Ridge (Egbert and Ray 2001). At 52 km from the ridge crest, observed outgoing energy was 15.1 GW and integrated dissipation was 2.0 GW. Thus the sum of outward internal wave energy and dissipation was 17 GW. Our vertically integrated estimates of energy density (3-6 kJ m^{-2} (Fig. 2.16a)), energy flux (1-5 kW m^{-1} (Fig. 2.15b)), and dissipation (2-10 mW m^{-2} (Fig. 2.16b)) were a factor of 2-3 smaller than previous full depth estimates at Kauai Channel (10-20 kJ m^{-2}, 4-21 kW m^{-1}, and 10-30 mW m^{-2},

respectively) (Merrifield and Holloway 2002; Rudnick et al. 2003; Klymak et al. 2006; Lee et al. 2006; Nash et al. 2006; Rainville and Pinkel 2006a; Zaron and Egbert 2006). Applying this factor of 2-3 implies a loss of 34-51 GW, or 1.5-2.5 times greater than the Egbert and Ray (2001) value, consistent with Kauai Channel being a hot spot along the ridge.

2.4.5 Momentum Flux and Mean Velocity

Mean fields of velocity and density had notable features near M_2 ray paths. Mean along-ridge velocity changed sign and mean across-ridge velocity was a maximum near M_2 ray paths (Fig. 2.17). Mean isopycnals were displaced towards the surface near M_2 ray paths (Fig. 2.4). We investigate the possibility that these correspondences were caused by internal waves forcing mean flows through momentum flux divergences. If mean fields are forced only by divergences of internal wave covariances, the governing equations are:

$$\left\langle u^* u^* \right\rangle_x + \left\langle u^* w^* \right\rangle_z = f\left\langle v \right\rangle - \frac{1}{\rho_0}\left\langle P_x \right\rangle \tag{2.7a}$$

$$\left\langle u^* v^* \right\rangle_x + \left\langle v^* w^* \right\rangle_z = -f\left\langle u \right\rangle \tag{2.7b}$$

$$0 = -\frac{1}{\rho}\left\langle P_z \right\rangle - N^2\left\langle \zeta \right\rangle \tag{2.7c}$$

$$\left\langle u^* \zeta^* \right\rangle_x + \left\langle w^* \zeta^* \right\rangle_z = \left\langle w \right\rangle \tag{2.7d}$$

$$\left\langle u \right\rangle_x + \left\langle w \right\rangle_z = 0. \tag{2.7e}$$

Observed $f^{-1}\left\langle u'u' \right\rangle_x$ was 1-4 cm s^{-1}, $f^{-1}\left\langle u'v' \right\rangle_x$ was 1-2 cm s^{-1}, and $\left\langle u'\zeta' \right\rangle_x$ was 10^{-4} m

s^{-1}. If the energy in the internal wave field is steady, $\langle w^* \zeta^* \rangle$ is zero from (2.4d) and

mean vertical velocity is given by: $\langle u^* \zeta^* \rangle_x + \langle w^* \zeta^* \rangle_z = \langle u^* \zeta^* \rangle_x$. Through mass

conservation (7e), mean across-ridge velocity is $\langle u^* \zeta^* \rangle_z$. Observed $\langle u' \zeta' \rangle_z$ was 2-3 cm

s^{-1} in rough agreement with $f^{-1} \langle u'v' \rangle_x$ (7b). Compared with observed mean velocities

along the tidal beams of 5-15 cm s^{-1} (Fig. 2.17), internal wave forcing of mean flows

was not quite an order of magnitude smaller. Momentum fluxes are partly responsible

for the relationships between mean fields and ray paths, but the relationships are not

fully understood.

Mean flows forced by the momentum flux divergences in (2.7) require

gradients along tidal beams, which are typically thought to be caused by dissipation

(Lighthill 1978), but can result from beam interactions in the absence of dissipation.

Beam interactions cause $\left(\phi_z^R, \phi_z^I \right)$ and $\left(\phi_x^R, \phi_x^I \right)$ to be disproportionate, which causes

$\langle u^* \zeta^* \rangle \neq 0$ (Section 2.4.1) forcing a mean vertical velocity (2.7d), and causes

$\langle u^* u^* \rangle_x + \langle u^* w^* \rangle_z$ and $\langle u^* v^* \rangle_x + \langle v^* w^* \rangle_z$ to be nonzero [see (2.4)-(2.6)] forcing mean

horizontal velocities (2.7a-b). Interactions between tidal beams result in mean flows in

all directions. For a knife-edge ridge with parameters as in Fig. 2.11,

$\langle u^* u^* \rangle_x + \langle u^* w^* \rangle_z$ and $\langle u^* v^* \rangle_x + \langle v^* w^* \rangle_z$ corresponded to velocities of 1-5 cm s^{-1}.

2.5 Conclusions

Notable features of this study include: 1) repeated sections intentionally

detuned from the M_2 frequency, so that M_2 phase was well sampled everywhere across the ridge, 2) observations of tidal beams in several covariances including changes in sign at the ridge and upon reflection from the surface, 3) a representative picture of the across-ridge structure of internal wave energy density, energy flux, and inferred dissipation, which allowed many of the goals of HOME to be investigated from a single set of observations, and 4) investigations of interactions between tidal beams, including effects on covariances and momentum flux divergences.

The systematic timing of sections in this study differed from previous methods of spatially surveying internal tides. Several studies have taken repeat sections and found tidal constituents by fitting (Loder et al. 1992; Petruncio et al. 1998; Kitade and Matsuyama 2002; Dale et al. 2003; Lam et al. 2004). Some studies fit to short time series taken at a number of stations (Pingree and New 1989; Kunze et al. 2002; Lee et al. 2006; Nash et al. 2006). Other studies have avoided fitting and averaged over all sections with imperfect distributions of tidal phase (Lien and Gregg 2001; Martin et al. 2006). In this study, intentionally timing sections to detune from the M_2 tide provided adequate averaging over M_2 phase, which allowed key features of the internal tide to be investigated.

Two semi-diurnal internal wave beams were evident as regions of elevated variance and covariance that coincided between many quantities including velocity and displacement variance, energy density, energy flux, $\langle u'\zeta'\rangle$, $\langle u'v_x'\rangle$, $\langle u_x'v'\rangle$, $\langle u'\zeta_x'\rangle$, and $\langle u_x'\zeta'\rangle$. Both beams were observed over 60 km horizontal distances, paralleled M_2 ray slopes, and reflected off of the surface. Beams in velocity shear and dissipation

were harder to distinguish, particularly for the downward beams. Differences between

the beam to the north of the ridge and the beam to the south were smaller than

variations within each beam. M_2 ray slopes originated from the sides of the ridge near

the ridge peak in agreement with several studies (Baines 1982; Holloway and

Merrifield 1999; Lamb 2004; Petrelis et al. 2006). Phase averaging of the observations

was adequate to observe sign changes in covariances at the ridge and when beams

reflected off of the surface. The barotropic tide was not removed from perturbation

fields, and did not appear to affect covariances. The directions of horizontal and

vertical energy flux along the beams as determined from $\langle u'v'_x \rangle$, $\langle u'_x \zeta' \rangle$, and $\langle u'P' \rangle$

corresponded to internal wave generation at the ridge.

These observations addressed some of the goals of HOME. The across-ridge

structure of internal tide energy density, energy flux, and dissipation was quantified

over a 152 km distance on both sides of the ridge. Turbulent dissipation, as

parameterized from velocity shear, was elevated relative to open ocean values along

M_2 ray paths. Averaged within 52 km of the ridge, the total energy dissipated to

mixing was $16\pm15\%$ of outward energy flux. Compared with 20 ± 6 GW of energy lost

from the barotropic tide at the Hawaiian Ridge (Egbert and Ray 2001), a 2500 km

ridge of Kauai Channel topography would have total dissipation plus outward energy

flux of 34-51 GW, consistent with Kauai Channel being a hot spot along the ridge. It

is desirable to explicitly separate the M_2, diurnal, and near-inertial frequencies, but in

order to phase average observations obtained over a 300 km distance, all frequencies

less than 18 days were included in the perturbation fields. The M_2 frequency most

likely was the dominant frequency, and only M_2 tidal beams were observed.

There are oscillating fields within and far from tidal beams allowing different beams to interact and covary with each other. Observed $\langle u'\zeta' \rangle$ was the key factor in focusing on this process because $\langle u^*\zeta^* \rangle$ is zero for isolated beams and is caused entirely by interactions between beams. Beam interactions cause gradients along beams in almost all covariances, and therefore cause momentum flux divergences and mean flows in the absence of dissipation. The observed covariances suggest wave-forced mean flows of 1-4 cm s^{-1}, about an order of magnitude smaller than observed mean flows. It was not clear whether internal wave forcing of mean flows at Kauai Channel was caused by beam interactions, dissipation, or beam interactions and dissipation. Further work on this topic could proceed with the addition of dissipation to the internal wave model used here.
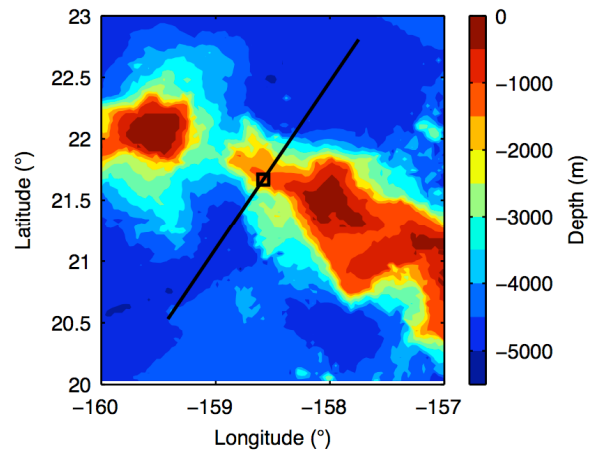
Figure 2.1 Bathymetry near Kauai Channel, Hawaii. The black line shows 304 km of the cruise track centered at 21.67°N, 158.58°W (black square). Velocity and density were measured over the upper 400-600 m along the cruise track 18 times from 2-19 October 2002.
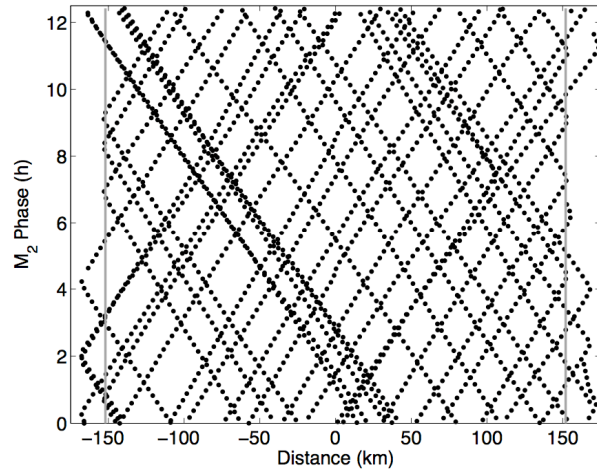
Figure 2.2 M$_2$ tidal phase as a function of distance along the cruise track. The center of the cruise track is 0 km, roughly the midpoint of the ridge. Each point shows the tidal phase at one particular location for one particular section across the ridge. Phase is relative to the tide at the beginning of data collection and does not indicate high or low tide. Subsequent plots range from ±152 km (gray vertical lines), where there was complete sampling of tidal phase.
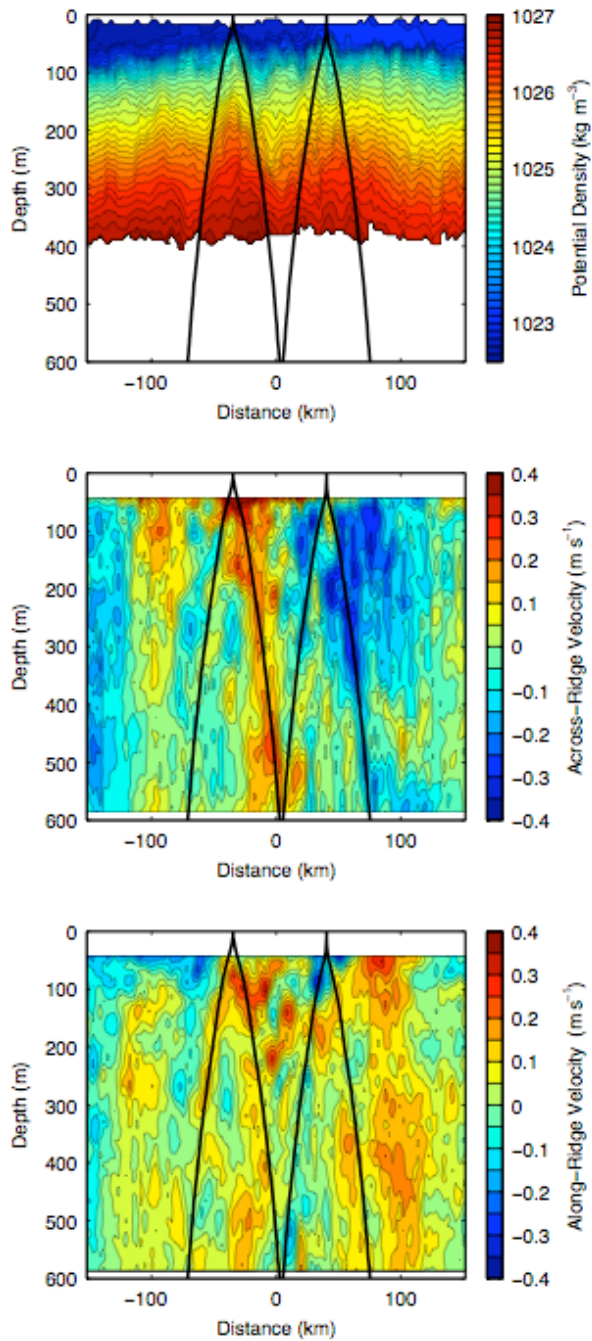
Figure 2.3 Sample section of potential density, ρ, across-ridge velocity, u, and along-ridge velocity, v, taken during spring tide (7 October 2002). Black lines are M_2 ray slopes as in Fig. 2.5.
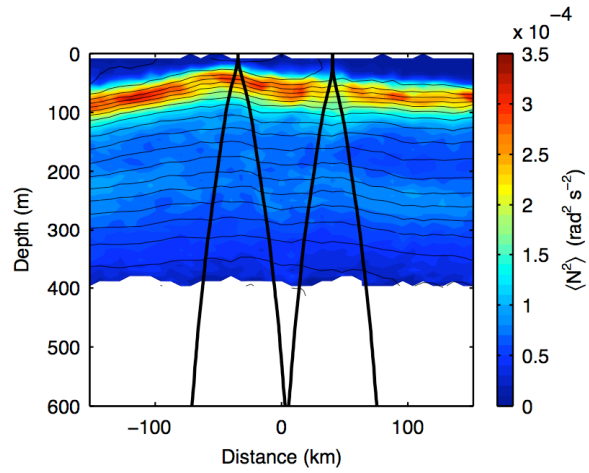
Figure 2.4 Average buoyancy frequency (color) and average density surfaces (contours). Density contours are separated by 0.2 kg m^{-3}. The average is over all 18 sections into bins with 8 km horizontal spacing and 8.6 m vertical spacing. Thick black lines are M$_2$ ray slopes as in Fig. 2.5.
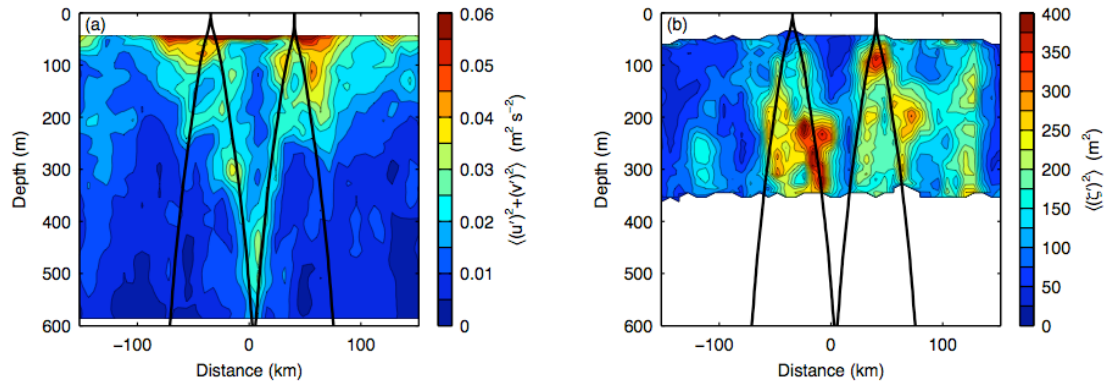
Figure 2.5 (a) Total velocity variance, $\left\langle (u')^2 + (v')^2 \right\rangle$, and (b) displacement variance, $\left\langle (\zeta')^2 \right\rangle$. Displacement is the deviation of each isopycnal from its mean depth. Black lines are M_2 ray slopes with the location of the surface reflections chosen by eye to best coincide with regions of largest velocity variance.
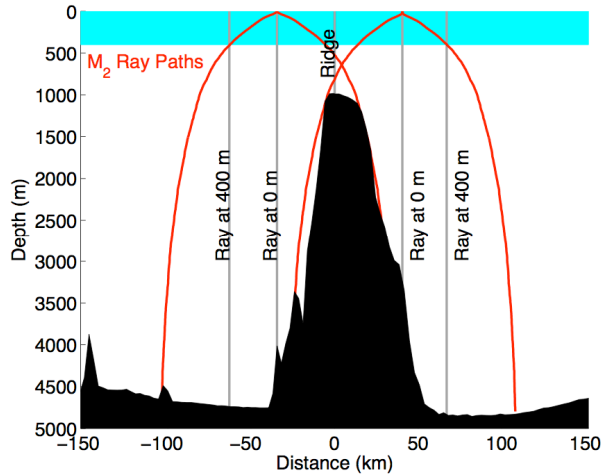
Figure 2.6 Across-ridge bathymetry and M_2 internal wave ray paths. Bathymetry is as measured along the cruise track with an echosounder. Horizontal placement of the ray paths (red) was based on velocity variance (Fig. 2.5a) and not the ridge profile. The mean buoyancy frequency of HOME was used to calculate ray slopes below 355 m. The upper 400 m where density observations were available is shaded. Ray paths reached the surface at +41 km and -35 km. Gray lines are shown at these surface reflections "Ray at 0 m," and where the reflected ray paths leave the region of available data "Ray at 400 m". The gray line at 0 km identifies the ridge crest.
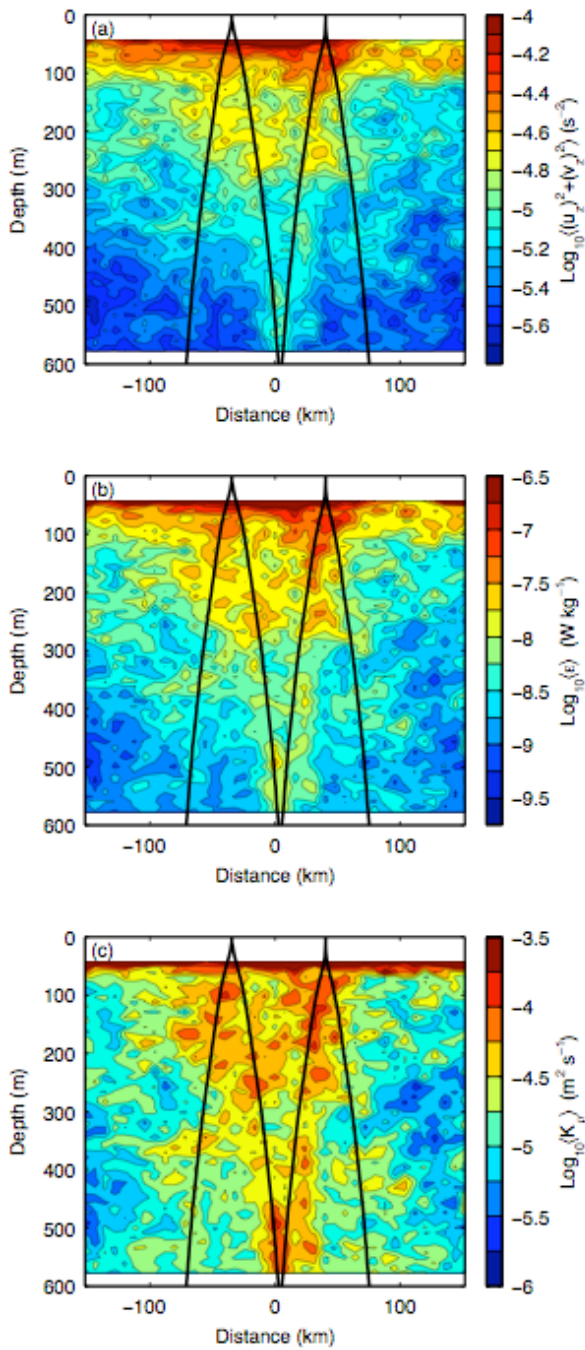
Figure 2.7 Mean (a) velocity shear squared, $\langle (u_z)^2 + (v_z)^2 \rangle$, (b) turbulent dissipation rate, $\langle \varepsilon \rangle$, and (c) diapycnal eddy diffusivity, $\langle K_\rho \rangle$. ε and K_ρ were parameterized based on velocity shear. The mean buoyancy frequency of HOME was used below 355 m in the parameterization. Ray paths as in Fig. 2.5.
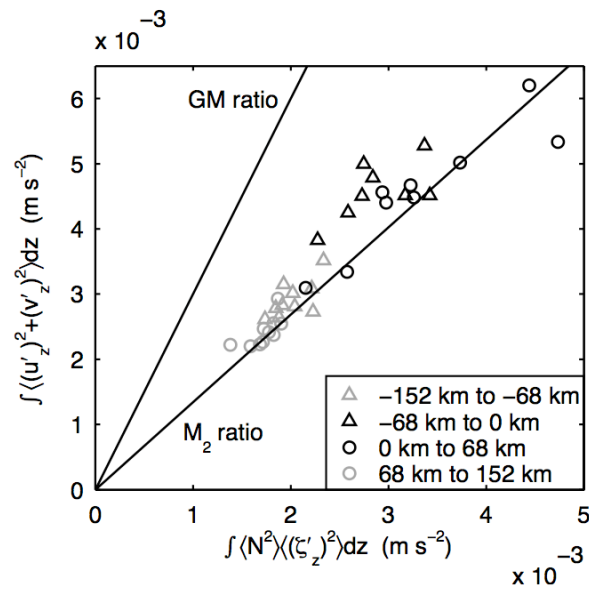
Figure 2.8 Shear-strain ratio. Each symbol represents the vertically integrated average value in an 8 km bin. Different symbols are used to distinguish between north (circles) and south (triangles) of the ridge crest as well as where tidal beams have been observed (black symbols are within 68 km of the ridge and gray symbols are greater than 68 km from the ridge). Theoretical values for the GM spectrum and inviscid M_2 plane waves are shown. $\rho_0 = 1026$ kg m^{-3} is a reference density. Vertical integration is over 95-355 m.
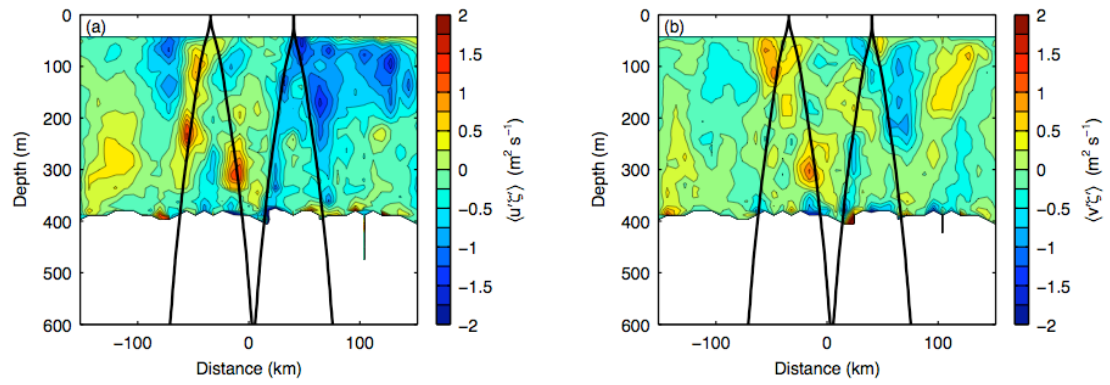
Figure 2.9 Covariance of displacement with (a) across-ridge velocity, $\langle u'\zeta' \rangle$ and (b) along-ridge velocity, $\langle v'\zeta' \rangle$. Ray paths as in Fig. 2.5.
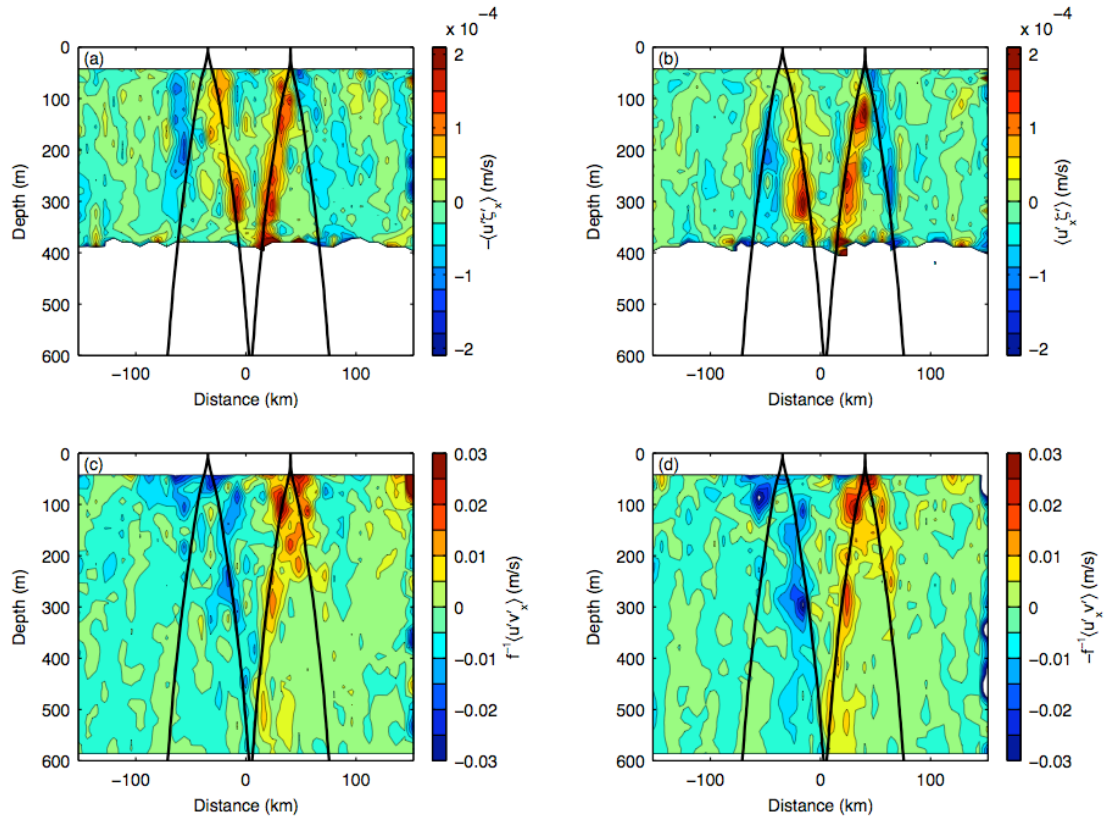
Figure 2.10 Covariances between u', v', and ζ' involving horizontal gradients. (a) $-\langle u'\zeta'_x \rangle$, (b) $\langle u'_x\zeta' \rangle$, (c) $f^{-1}\langle u'v'_x \rangle$, and (d) $-f^{-1}\langle u'_x v' \rangle$. Ray paths as in Fig. 2.5.
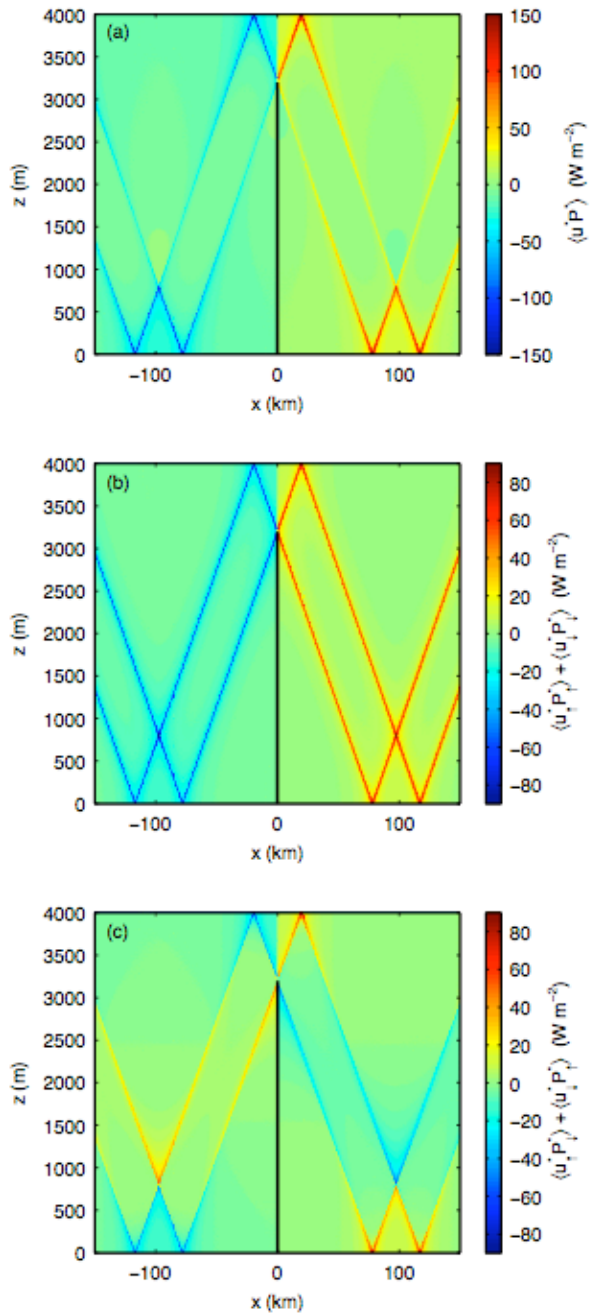
Figure 2.11 Across-ridge energy flux for a knife-edge ridge. The solid black line at $x=0$ km represents the ridge. (a) Across-ridge energy flux is the sum of (b) across-ridge energy flux from isolated beams and (c) across-ridge energy flux from beam interactions. $\langle u_\uparrow^* P_\downarrow^* \rangle = \langle u_\downarrow^* P_\uparrow^* \rangle$ and vertically integrates to zero. Parameters used in Equations 2.4-2.6 are $n=100$, $U_0=0.1$ m s^{-1}, $h_0/H=0.8$, $N^2 = 1 \cdot 10^{-5}$ rad^2 s^{-2}, and $f = 5.4 \cdot 10^{-5}$ s^{-1}.
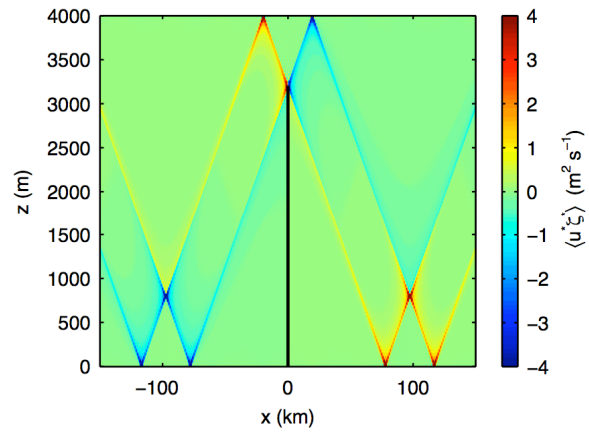
Figure 2.12 $\left\langle u^{*}\varsigma^{*}\right\rangle$ from (2.4)-(2.6) with parameters as in Fig. 2.11. The covariance is caused by interactions between tidal beams.
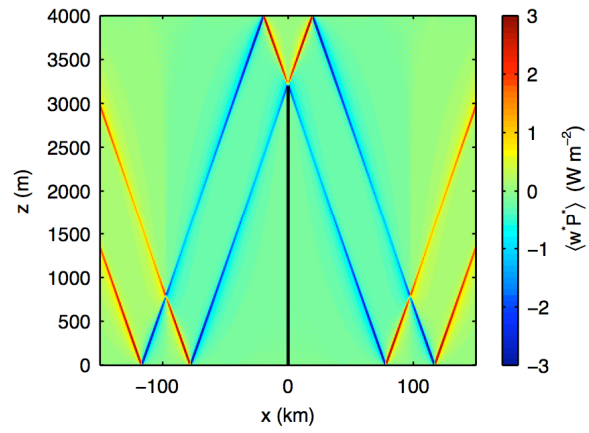
Figure 2.13 Vertical energy flux, $\langle w^* P^* \rangle$, from (2.4)-(2.6) with parameters as in Fig. 2.11.
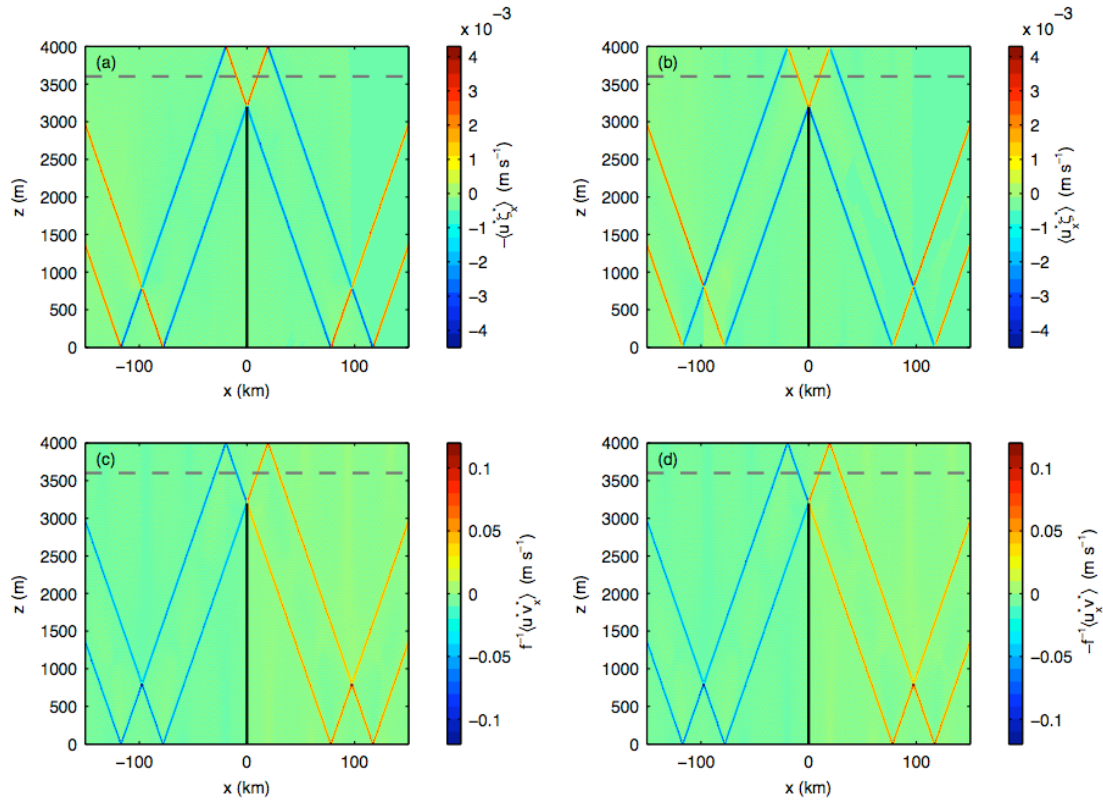
Figure 2.14 Covariances between u^*, v^*, and ζ^* involving horizontal gradients calculated from (2.4)-(2.6). (a) $-\langle u^* \zeta_x^* \rangle$, (b) $\langle u_x^* \zeta^* \rangle$, (c) $f^{-1}\langle u^* v_x^* \rangle$, and (d) $-f^{-1}\langle u_x^* v^* \rangle$. Dashed gray lines mark the upper 10% of the water column. Parameters as in Fig. 2.11. Signs should be compared to Figs. 2.11a and 2.13, and to Fig. 2.10 in the upper ocean.
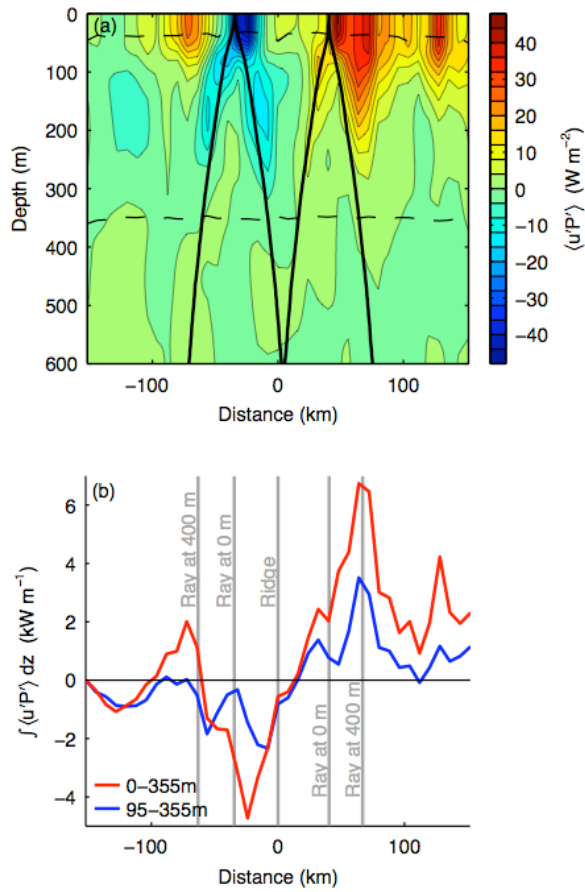
Figure 2.15 Energy flux. (a) $\langle u'P' \rangle$ as fit to ten vertical modes. Dashed lines show the average region where density was observed. Ray paths as in Fig. 2.5. (b) $\langle u'P' \rangle$ vertically integrated over 95-355 m and 0-355 m. Gray vertical lines represent changes in the sign of the ray slope in the upper 400 m as shown in Fig. 2.6.
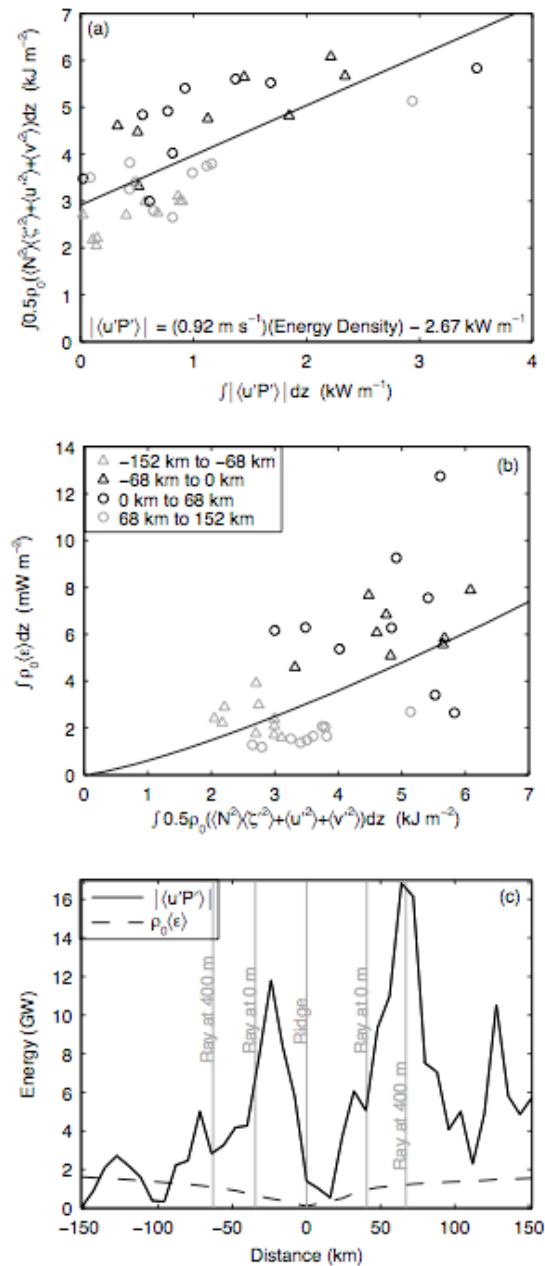
Figure 2.16 Relationships between integrated energy density, energy flux, and dissipation. (a) Energy density versus energy flux. The best linear fit is shown (black). (b) Energy density versus turbulent dissipation. The black curve is the best-fit power law of 1.3. Vertical integration in (a) and (b) is over 95-355 m. Symbols in (a) and (b) as in Fig. 2.8. (c) Integrated energy flux and dissipation. Energy flux is integrated vertically over 0-355 m and horizontally along a 2500 km ridge (solid line). Dissipation is integrated vertically over 95-355 m, horizontally from 0 km across the ridge, and horizontally along a 2500 km ridge (dashed line). Gray vertical lines as in Fig. 2.6. ρ_0 in (b) and (c) as in Fig. 2.8.
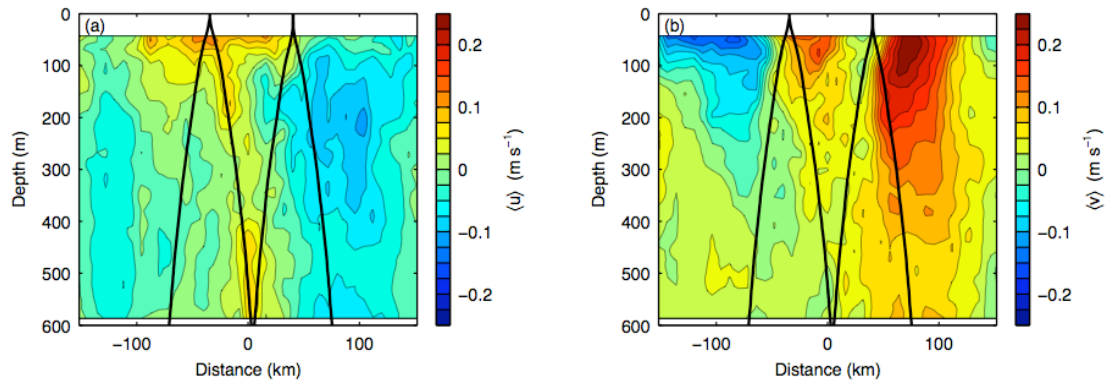
Figure 2.17 Mean (a) across-ridge velocity, $\langle u \rangle$ and (b) along-ridge velocity, $\langle v \rangle$. Ray paths as in Fig. 2.5.

Chapter 3

# Seasonal Evolution of Upper-Ocean Horizontal Structure and the Remnant Mixed Layer

Abstract of Chapter 3

We discuss the seasonal evolution of upper ocean thermohaline structure at small horizontal scales. The upper 350 m of a 1000 km long section in the subtropical North Pacific was observed in winter, spring, and summer with 3-14 km horizontal resolution. Four vertical regions had distinct density and salinity structure: the mixed layer, remnant mixed layer, high-stratification layer, and permanent thermocline. The remnant mixed layer consists of water from the winter mixed layer left over after restratification. The remnant mixed layer was most similar to the mixed layer in winter and spring, and most similar to the high-stratification layer below in summer. The high-stratification layer had elevated stratification that varied seasonally. The permanent thermocline varied little seasonally and was horizontally and vertically uniform in comparison. In all seasons, density ratios showed that mixed layer θ-S differences tended to compensate in density with the strongest tendency towards compensation in winter. Density ratios were temperature dominated in the remnant mixed layer consistent with salt-fingering. Salinity anomalies were largest at the surface and decayed with depth in all seasons. Spectra of isopycnal depth and θ-S

anomalies along isopycnals are compared between the three seasons and four vertical layers. Isopycnal depth variance at 30-46 km wavelengths decreased from winter to spring to summer by a factor of 2-10 in stratified regions. By treating salinity anomalies as a tracer, the effective isopycnal diffusivity in the remnant mixed layer was estimated to be 1.4 $m^2 s^{-1}$ over 30-46 km wavelengths.

3.1 Introduction

Seasonal changes in upper ocean horizontal structure involve vertical mixing in winter and restratification in spring. In the subtropics, the deepest mixed layers of order 100 m (Fig. 3.1) occur between December and March depending on the region (Oka et al. 2007; Ohno et al. 2009). Deep mixed layers result from mechanical mixing caused by surface winds, and convection caused by surface cooling. In spring, the mixed layer is a few tens of meters deep and less dense than in winter. The mixed layer shoals and restratifies because surface heating increases and wind forcing decreases. The shallow spring mixed layer isolates the majority of the deep winter mixed layer from the atmosphere. We refer to the water parcels left over from the winter mixed layer after restratification as the remnant mixed layer. The remnant mixed layer extends from the mixed layer base in any season to the density of the previous winter's mixed layer (Fig. 3.1). In summer, the mixed layer is still a few tens of meters deep and continues to warm, which increases stratification within the remnant mixed layer. In the fall and early winter, cooling begins and the mixed layer

deepens, which eats into the remnant mixed layer from above. This study quantifies seasonal changes in the mixed layer, remnant mixed layer, and regions just below.

We observe a single location in different seasons at small horizontal scales, which is part of a growing number of such observations. Ship-based observations with 1-10 km horizontal resolution are common, but only capture a few consecutive days or weeks of the year in any one location (Pollard 1986; Weller 1991; Ferrari and Rudnick 2000; Rudnick and Martin 2002; Hosegood et al. 2006). Seasonal observations from ship-based measurements and autonomous floats are also common, but horizontal resolution is typically 100 km or larger (Montegut et al. 2004; Roemmich et al. 2004; Ohno et al. 2009). Seasonal observations at 1-3 km scales began by using towed vehicles to study the same location at different times of the year: during 1981-1987 (Strass et al. 1992), during 1991-1993 (Joyce et al. 1998), and during 1998 (James et al. 2002). Since 1986, expendable bathythermographs have been used to obtain multi-year seasonal observations at 10-40 km scales (Hautala and Roemmich 1998; Sprintall and Roemmich 1999; Sprintall 2003). Since 2003, gliders have captured seasonal changes in a variety of locations at 3-6 km scales (Davis et al. 2008; Glenn et al. 2008; Nicholson et al. 2008; Perry et al. 2008). We add to the growing amount of seasonal small-scale observations by observing a single section in winter, spring, and summer at 3-14 km scales.

The contribution of potential temperature (θ) and salinity (S) gradients to potential density (ρ) gradients depends on depth and season. In the subtropical thermocline, vertical and horizontal temperature gradients over 0.1-1000 km

horizontal scales often exceed the corresponding salinity gradients by a factor of two in density (Schmitt 1981; Schmitt 1990; Ferrari and Rudnick 2000; Rudnick and Martin 2002). This is attributed to the different diffusive timescales of heat and salt, which cause salt-fingering (Schmitt 1994). In contrast, deep mixed layers in winter in the subtropics and potentially year round in the southern ocean often have horizontal θ and S gradients at 0.1-1000 km scales that compensate in their effect on density (Rudnick and Ferrari 1999; Rintoul and Trull 2001; James et al. 2002; Rudnick and Martin 2002). Temperature dominance has also been observed (Hosegood et al. 2006) and is typical in mixed layers shallower than 50 m (Rudnick and Martin 2002). Density compensation requires strong vertical mixing, and so varies with mixed layer depth and season. When vertical mixing is strong, horizontal density gradients at scales smaller than the Rossby radius slump out of the mixed layer leaving behind only compensated gradients (Young 1994; Young and Chen 1995; Ferrari and Young 1997; Ferrari and Paparella 2003; Boccaletti et al. 2007).

In our observations, horizontal salinity structure serves as a tracer provided by nature. Tracers intentionally injected into the ocean have been used to understand isopycnal and diapycnal diffusivity over a range of temporal and spatial scales (Okubo et al. 1971; Ledwell et al. 1998; Sundermeyer and Ledwell 2001; Messias et al. 2008). Salinity anomalies (Needler and Heath 1975; Armi and Stommel 1983; Bauer and Siedler 1988) and other naturally occurring tracers (Jenkins 1987) have also been used to estimate diffusivity. We treat salinity structure as a tracer, and estimate smaller scale effective isopycnal diffusivity on seasonal timescales.

This paper compares seasonal statistics of the upper ocean at 15-1000 km scales, including the mixed layer and remnant mixed layer. The observations and their seasonal timing are described in Section 3.2. Density and salinity sections are discussed in Section 3.3 and show four vertical regions: the mixed layer, remnant mixed layer, high-stratification layer, and permanent thermocline. Sections 3.4-3.6 discuss density compensation (Sect. 3.4), isopycnal depth variability (Sect. 3.5), and isopycnal temperature and salinity variability (Sect. 3.6). Conclusions are presented in Section 3.7.

3.2 Observations and Methods

Temperature and salinity along a 1000 km cruise track in the North Pacific (Fig. 3.2) were observed in June 2004, September 2004, and March - April 2005 as part of the North Pacific Acoustic Laboratory (NPAL) experiment (Worcester and Spindel 2005). The cruise track was along a great circle located between two acoustic moorings, was mainly zonal, and was only slightly askew from sea-surface temperature (SST) contours. Two instruments were used: an underway conductivity-temperature-depth (UCTD) probe, which is dropped and recovered from an underway ship (Rudnick and Klinke 2007), and SeaSoar, which is a towed platform (Pollard 1986). We analyze four sections: one in June and one in September taken with the UCTD, and one in March and one in April taken with SeaSoar. The UCTD profiled from the surface to 300-400 m depth, and SeaSoar cycled from 0-20 m to 300-400 m depth. Each of the four sections took 3-5 days to complete (Table 3.1).

Observations were averaged into vertical profiles at 3-14 km horizontal spacing. UCTD profiles were binned onto a 5 m vertical grid. The section average temporal spacing between profiles was 0.5 h excluding time gaps greater than three hours: two in September of 1.4 days and 1.9 days, and one in June of 1.8 days. The section average horizontal spacing between profiles, which was determined by ship speed and the frequency of profiles, was 10.5 km in June and 13.4 km in September (Table 3.1). SeaSoar took 10-15 minutes to cycle from the surface to 300-400 m depth and back. The 24-Hz raw SeaSoar observations were averaged into one-second records, and then each complete vertical cycle was averaged into a single profile with 5 m vertical spacing. Section average horizontal spacing between profiles was 3.4 km in March and 2.6 km in April.

Observations were taken in late winter, late spring, and late summer. SST averaged in a box around the cruise track, 33-35°N, 136-150°W, was similar in magnitude and timing between 2004 and 2005 (Fig. 3.3). In 2004, August-September was approximately 1°C warmer, and January-February was approximately 1-2°C cooler. March-April observations were made during the minimum SST of about 16°C, and September observations were made just after the maximum SST of 24.5°C. June SST, about 20°C, was approximately halfway between the seasonal extremes. March-April observations will be referred to as winter conditions, June as spring conditions, and September as summer conditions.

We consider statistics calculated from observed profiles with ensembles defined as follows. The spring and summer ensembles consist of the June and

September profiles at 10.5 and 13.4 km resolution, respectively. The winter ensemble combines the 3 km March and April profiles because they were observed 17 days apart at most and had similar statistics. We create a second winter ensemble with 10-14 km horizontal resolution by choosing every fourth profile in the 3km March and April sections (Table 3.1). Statistics of the subsampled ensemble are used when horizontal resolution is important and are calculated using all possible combinations of every fourth profile so that no profiles are ignored.

Isopycnal depth, Z_{iso} , temperature along isopycnals, θ_{iso}, and salinity along isopycnals, S_{iso}, are calculated by linear interpolation. Stratification along isopycnals, N^2_{iso}, is calculated from the difference in depth between two isopycnals. Quantities along isopycnals are not calculated in the mixed layer where density surfaces are difficult to define.

3.3 Density and Salinity Structure

Density and salinity sections show four vertical regions distinguished by thermohaline structure, and affected by different physical processes: the mixed layer, remnant mixed layer, high-stratification layer, and permanent thermocline (Figs. 3.4-3.6). The following sub-sections define these regions, and describe their basic properties and seasonal evolution. We use these definitions to organize subsequent discussion, as the regions are readily identifiable in the sections.

3.3.1 Mixed Layer

The mixed layer is distinguishable in density by large-scale warming from winter to spring to summer and in salinity by small-scale horizontal variability in all seasons (Figs. 3.4-3.5). The mixed layer base, MLB, is defined using a density threshold of 0.05 kg m^{-3} from the shallowest observation (Fig. 3.4). Because of warming and weak vertical mixing, the average ± standard deviation of the MLB shoaled from 80±21 m in winter to 26±6 m in spring and remained essentially the same at 36±6 m in summer. Mean salinity did not change between winter and spring, but surface warming and evaporation increased salinity by 0.4 psu between spring and summer (Fig. 3.5). Horizontal salinity and density gradients were observed in all seasons. Salinity structure was sometimes correlated with the stratified regions below, particularly in winter and spring.

3.3.2 Remnant Mixed Layer

We use the term remnant mixed layer to refer to the water left behind after deep winter mixed layers restratify, as in previous studies (Brainerd and Gregg 1993; Paillet and Arhan 1996; Alfultis and Cornillon 2001). The remnant mixed layer extends from the MLB down to the isopycnal the mixed layer reached the previous winter. We define the remnant mixed layer base as the 25.4 kg m^{-3} isopycnal based on density, stratification, and thermohaline structure. Based on density, the 25.4 kg m^{-3} isopycnal was the lightest isopycnal that was always observed (Fig. 3.4) and varied little with depth seasonally (Fig. 3.7a). In winter, the 25.4 kg m^{-3} isopycnal coincided with the MLB in some places (Fig. 3.1 is an example). In all seasons, the 25.4 kg m^{-3}

isopycnal also separates regions of different thermohaline structure (Fig. 3.5) and different stratification (Fig. 3.6).

Seasonal changes in surface heating and vertical mixing affected the thickness and density range of the remnant mixed layer. In winter, a thin remnant mixed layer with weak stratification was observed in the majority of profiles, indicating that restratification had recently occurred (Fig. 3.4a-b; 3.6a-b). Between winter and spring, decreased vertical mixing caused the remnant mixed layer to thicken (Fig. 3.4a-c), and surface heating decreased the minimum average density from 25.1 kg m^{-3} to 24.5 kg m^{-3} (Fig. 3.7b). Between spring and summer, the thickness of the remnant mixed layer remained the same, but continued surface heating further decreased the minimum average density to 24.0 kg m^{-3}.

Stratification within the remnant mixed layer increased from winter to spring to summer. In winter, stratification was smallest near the MLB and largest near the 25.4 kg m^{-3} isopycnal (Fig. 3.6-3.7). Between winter and spring, stratification increased and was largest at the MLB. Between spring and summer, the remnant mixed layer had essentially the same thickness (Fig. 3.6c-d) while continued surface heating caused additional isopycnals to restratify and stratification to increase (Fig. 3.6-3.7). Stratification increased only slightly for the 24.5-25.4 kg m^{-3} isopycnals that were present in the spring remnant mixed layer (Fig. 3.7b). The additional isopycnals restratified between spring and summer, 24.0-24.5 kg m^{-3}, had much higher stratification and were packed into the 12 m just below the MLB. Direct solar heating of the remnant mixed layer was probably small as the attenuation coefficient for light

in this region, 0.09-0.19 m^{-1} (Siegel and Dickey 1987), corresponds to a 10% light level of 12-25 m depth. Higher stratification most likely resulted from weak vertical mixing with the warmer mixed layer above.

Salinity in the remnant mixed layer inherited structure from the winter mixed layer. In winter and spring, salinity was horizontally variable with a similar magnitude and horizontal scale to salinity in the mixed layer. The correlation of vertically averaged salinity between the remnant mixed layer and mixed layer was high in both winter and spring: 0.82-0.84 (Table 3.2). This correlation suggests salinity structure is simply left behind during restratification. Between spring and summer, large scale heating and evaporation homogenized the mixed layer causing the correlation of vertically averaged salinity between the mixed layer and remnant mixed layer to decrease by a factor of 2. Salinity structure remained in the summer remnant mixed layer because it was isolated from surface forcing by the strong stratification at the MLB (Fig 3.4-3.6).

3.3.3 High-Stratification Layer

A region of high stratification was observed below the remnant mixed layer (Fig. 3.4, 3.6). Elevated stratification was observed between the base of the remnant mixed layer, the 25.4 kg m^{-3} isopycnal, and the 25.9 kg m^{-3} isopycnal in all seasons (Fig. 3.4, 3.6-3.7), so we term this region the high-stratification layer. Stratification decreased between winter and spring but remained larger than stratification above or below (Fig. 3.7b). There was no change in stratification between spring and summer.

A similar region of high stratification below the remnant mixed layer has been observed in the eastern North Atlantic subtropical gyre (Paillet and Arhan 1996).

Salinity in the high-stratification layer was horizontally variable and sometimes correlated with the remnant mixed layer above. In all seasons, the high-stratification layer was the freshest layer observed and is part of the shallow salinity minimum waters in the North Pacific (Talley 1985; Yuan and Talley 1992). In winter, the correlation of vertically averaged salinity between the high-stratification layer and remnant mixed layer was 0.33 (Table 3.2). The two layers were essentially uncorrelated verifying that salinity structure in the remnant mixed layer is set from above during restratification. Between winter and spring, the correlation of vertically averaged salinity between the high-stratification layer and remnant mixed layer doubled (Table 3.2). Most likely, the correlation increased because vertical mixing occurred between the two layers, which is consistent with decreased stratification in the high-stratification layer (Fig. 3.7b). Between spring and summer, the correlation of vertically averaged salinity decreased only slightly (Table 3.2) and mean stratification did not change. Additional vertical mixing did not occur between the two layers from spring to summer.

3.3.4 Permanent Thermocline

The permanent thermocline lies below the 25.9 kg m^{-3} isopycnal where stratification did not change seasonally (Fig. 3.4, 3.6-3.7). Salinity in the permanent thermocline was horizontally and vertically uniform in comparison to the layers above

(Fig. 3.5). In all seasons, salinity structure was correlated with the high stratification layer above and decayed with depth. The correlation of vertically averaged salinity between the permanent thermocline and high-stratification layer was 0.76-0.95 (Table 3.2). The two layers were correlated because neither was directly influenced by surface forcing, and both experienced essentially the same internal wave activity and mixing.

3.4 Density Ratios

Horizontal and vertical density ratios show the relationship between θ and S differences. θ and S differences are expressed in terms of their affect on ρ, $\alpha\Delta\theta$ and $\beta\Delta S$, where α and β are coefficients of thermal expansion and saline contraction, respectively. The horizontal and vertical density ratios are $R = \alpha\Delta_h\theta/\beta\Delta_h S$ and $R_\rho = \alpha\Delta_v\theta/\beta\Delta_v S$, respectively where Δ_h is a horizontal difference along depth surfaces and Δ_v is a vertical difference across depth surfaces. Perfect density compensation corresponds to R=1 and R_ρ=1, and temperature dominance to $|R| > 1$ and $|R_\rho| > 1$. R is most useful in the mixed layer, and R_ρ in stratified regions. Probability density functions (PDFs) of horizontal Turner angle, $\tan^{-1}(R)$ and vertical Turner angle, $\tan^{-1}(R_\rho)$, are considered. Turner angle is advantageous because it has a finite range, $-\pi/2$ to $\pi/2$, and temperature dominated and salinity dominated regions occupy equal portions of Turner angle space. We also consider the dependence of R on the

thermohaline difference, $\sqrt{\left(\alpha\Delta_h\theta\right)^2 + \left(\beta\Delta_h S\right)^2}$, which is one measure of the size of θ and S differences.

3.4.1 Mixed Layer

We first consider the relative sizes of θ, S and ρ differences and their seasonal variation. In all seasons, the standard deviation of $\beta\Delta_h S$ was 0.01-0.03 kg m^{-3} larger than $\alpha\Delta_h\theta$ and 0.01-0.05 kg m^{-3} larger than $\Delta_h\rho$ (Fig. 3.8). θ, S and ρ differences increased by 0.02-0.05 kg m^{-3} between winter and spring, and decreased by 0.01-0.03 kg m^{-3} between spring and summer because large scale heating and evaporation homogenized the mixed layer. Density compensation occurred in winter as the standard deviation of $\alpha\Delta_h\theta$ and $\beta\Delta_h S$ was more than twice as large as $\Delta_h\rho$. In spring and summer, the standard deviation of $\Delta_h\rho$ and $\alpha\Delta_h\theta$ was approximately the same indicating decreased density compensation.

Density compensation was observed in all seasons, but was most common in winter. In winter, the PDF of horizontal Turner angle had a mode corresponding to R slightly less than one (Fig. 3.9a). Most θ and S differences were nearly compensated in ρ with $\beta\Delta_h S$ slightly larger than $\alpha\Delta_h\theta$. In spring, horizontal θ and S differences were less likely to compensate in ρ because of weaker vertical mixing. The PDF of horizontal Turner angle became more uniform with fewer differences clustered near $R=1$. The mode of R remained slightly less than one, and θ and S differences were still most often approximately compensated in ρ. In summer, the PDF of horizontal Turner angle was similar to spring and more uniform than in winter, suggesting that the

processes affecting temperature and salinity in the mixed layer were similar between spring and summer.

In winter, density compensation was observed for all sizes of the thermohaline difference. The PDF of horizontal Turner angle for all thermohaline differences had a mode near $R=1$ (Fig. 3.10). Smaller thermohaline differences had more uniform PDFs of horizontal Turner angle and a mode farther from $R=1$ in agreement with previous predictions (Ferrari and Young 1997) and observations (Rudnick and Martin 2002) that the largest gradients are most likely to be compensated.

3.4.2 Remnant Mixed Layer

In all seasons, the vertical density ratio in the remnant mixed layer was temperature dominated consistent with salt-fingering (Fig. 3.9b). In winter, R_ρ was most often 2.0. Because stratification was weak, vertical S differences were sometimes larger than vertical θ differences resulting in a small preference for R_ρ slightly less than one. In spring, the vertical density ratio did not change drastically even though stratification increased and the remnant mixed layer thickened. Increased stratification caused vertical θ differences to exceed vertical S differences everywhere and there was no preference for R_ρ slightly less than one. In summer, R_ρ was more temperature dominated with a mode larger than 2.0 possibly because stratification increased.

3.4.3 High-Stratification Layer

The vertical density ratio in the high-stratification layer was most often larger than 2.0 and varied little between seasons (Fig. 3.9c). Decreased stratification between winter and spring did not change the vertical density ratio significantly. Between spring and summer, the mode of the vertical density ratio decreased slightly, but was still larger than 2.0.

3.4.4 Permanent Thermocline

The vertical density ratio in the permanent thermocline was most often larger than in the high-stratification layer (Fig. 3.9d). The mode of R_ρ was slightly higher primarily because vertical salinity differences were small (Fig. 3.5). The PDF of vertical Turner angle changed slightly between winter and spring, and remained essentially the same between spring and summer. Between winter and spring, a slightly smaller percentage of differences corresponded to R>0 indicating that salinity differences were less likely to decrease with depth (there were slightly fewer positive salinity anomalies near the high-stratification layer).

3.5 Isopycnal Depth Variability

Variance in isopycnal depth is a measure of the strength of internal waves and geostrophically balanced eddies. Internal waves may be driven by wind forcing, which is strongest in winter. Geostrophic eddies are generally the result of baroclinic instability, and a seasonal modulation is possible to the extent that background gradients have an annual cycle. Internal waves and eddies may overlap in

wavenumber, so they cannot be unambiguously separated, but the seasonal cycle in isopycnal depth variance can be quantified. Seasonal variations in internal waves and eddies are determined by calculating wavenumber spectra of isopycnal depth. Spectra are calculated using only the region observed in all four sections, from 138.22°W to 148.07°W. The non-uniformly spaced observations are interpolated onto a 0.5 km uniform grid and a trend removed so that endpoints are equal. Fourier coefficients are averaged in adjacent wavenumber bands, with more degrees of freedom at higher wavenumbers. To determine confidence limits, the number of degrees of freedom at each wavelength is taken as twice the record length, 927 km, divided by the wavelength. The wavelengths considered range from 30 km, which is an average over 27.3-33.1 km wavelengths, to 371 km. Spectra are vertically averaged within each layer with only the 25.9-26.3 kg m^{-3} isopycnals included in the permanent thermocline. We focus primarily on variability at smaller wavelengths where a clear seasonal change was observed. We do not consider Z_{iso} variability in the mixed layer.

3.5.1 Remnant Mixed Layer

Isopycnal depth variance in the remnant mixed layer was largest in winter and decreased at smaller wavelengths from winter to spring to summer. In all seasons, isopycnal depth variance over 30-371 km wavelengths approximately followed a k^{-2} power law (Fig. 3.11a) in agreement with previous observations (Katz 1975; Dugan et al. 1986). Spectral slopes of k^{-2} are consistent with a series of fronts. Between winter and spring, variance decreased at almost all wavelengths. The decrease occurred partly

because different isopycnals were in the remnant mixed layer, and partly because characteristics of the MLB changed. The winter MLB varied greatly in depth, more so than the 25.4 kg m^{-3} isopycnal, while the spring MLB was flat and varied less than the 25.4 kg m^{-3} isopycnal because of large-scale mixed layer heating (Fig. 3.4). Between spring and summer, variance at 80-371 km wavelengths increased and variance at 30-80 km wavelengths decreased. At 30-46 km wavelengths, variance decreased by a factor of 5.6 between winter and spring, which is significant at the 90% confidence level, and by a factor of 1.8 between spring and summer, which is not significant at the 90% confidence level (Table 3.3). The decrease in smaller-scale variance is consistent with previous observations of surface eddy kinetic energy in the eastern North Pacific decreasing from winter to spring to summer (Stammer and Wunsch 1999; Ducet et al. 2000).

3.5.2 High-Stratification Layer

Isopycnal depth variance in the high-stratification layer differed between winter and spring, and remained the same between spring and summer (Fig. 3.11b). In the high-stratification layer, spring and summer spectra followed a k^{-2} power law and the winter spectra was somewhat flatter. Between winter and spring, Z_{iso} variance increased at 100-371 km wavelengths and decreased at 30-60 km wavelengths. Between spring and summer, there were no significant changes in variance. Over 30-46 km wavelengths, variance decreased by a factor of 2.5 between winter and spring (Table 3.3), significant at the 90% confidence level, which is somewhat smaller than

in the remnant mixed layer. The decrease between winter and spring is again consistent with peak eddy kinetic energy in winter months (Stammer and Wunsch 1999; Ducet et al. 2000).

3.5.3 Permanent Thermocline

Isopycnal depth variance in the permanent thermocline changed seasonally by a smaller amount than in the layers above (Fig. 3.11c). Total variance increased between winter and spring, and remained essentially the same between spring and summer. Over 30-46 km wavelengths, variance decreased by a factor of 1.4 between winter and spring and by a factor of 1.5 between spring and summer, smaller than in the layers above (Table 3). Only the decrease between winter and summer is significant at the 90% confidence level.

3.6 Isopycnal Temperature-Salinity Variability

Large variations of θ and S along isopycnals occur in the remnant mixed layer and high stratification layer in all seasons (Fig. 3.5). In the remnant mixed layer, S_{iso} variability results from salinity variability in the mixed layer left behind during restratification. S_{iso} variability is smaller in the high stratification layer, and smallest in the permanent thermocline. S_{iso} variability increases because of stirring and decreases because of isopycnal mixing. Vertical mixing between isopycnals may increase or decrease S_{iso} perturbations as well. We observe only the end result of stirring, isopycnal mixing, and vertical mixing on S_{iso} perturbations. Although we observe S_{iso}

variability in all seasons, S_{iso} variability may change seasonally, particularly in the

remnant mixed layer as additional isopycnals are restratified.

Along an isopycnal, temperature changes are exactly balanced by salinity

changes and the variability of θ_{iso} and S_{iso} is the same. In the rest of this section, we

show and discuss only θ_{iso} variability. To compare stratified regions with the mixed

layer, we also consider the variability of θ on depth surfaces in the mixed layer. We

calculate spectra of θ in the mixed layer and θ_{iso} in stratified regions in the same

fashion as Z_{iso} to determine isopycnal θ-S variability as a function of wavelength. As

with isopycnal depth variance, we focus primarily on variability at smaller scales

where a clear seasonal change was observed.

θ_{iso} perturbations varied with depth and season (Fig. 3.12). In all seasons and

most horizontal scales, θ_{iso} perturbations were largest in the mixed layer and decayed

with depth confirming that variance is set at the surface. Perturbations in the

permanent thermocline were not quite an order of magnitude smaller than in the

remnant mixed layer. In the mixed layer, θ_{iso} perturbations decreased between spring

and summer over most horizontal scales because large-scale surface forcing

homogenized the mixed layer (Fig. 3.12a). In the remnant mixed layer, smaller scale

θ_{iso} perturbations increased slightly between winter and spring and decreased between

spring and summer (Fig. 3.12b). In the high-stratification layer, θ_{iso} perturbations were

similar in winter, spring, and summer (Fig. 3.12c). In the permanent thermocline, θ_{iso}

perturbations were similar in winter and spring, and slightly larger in summer (Fig.

3.12d).

3.6.1 Mixed Layer

Temperature spectra show that variance in the mixed layer increased between winter and spring and decreased between spring and summer (Fig. 3.13a). In all seasons, temperature variance at 30-371 km wavelengths approximately followed a k^{-2} power law in agreement with previous mixed layer observations (Samelson and Paulson 1988; Strass 1992; Hodges and Rudnick 2006). As with isopycnal depth spectra, spectral slopes of k^{-2} are consistent with a series of fronts. Total variance increased by a factor of 2 between winter and spring, but decreased by a factor of 4 between spring and summer because large-scale heating homogenized the mixed layer. At 30-46 km wavelengths, variance was essentially the same in winter and spring, but a factor of 4.7 smaller in summer, which is significant at the 90% confidence level (Table 3.4). The decrease in variance between spring and summer is most likely a result of large-scale surface forcing and not straining or isopycnal mixing.

3.6.2 Remnant Mixed Layer

Similar to the mixed layer, isopycnal θ-S variance in the remnant mixed layer increased between winter and spring and decreased between spring and summer over almost all wavelengths (Fig. 3.13b). θ_{iso} variance at 30-371 km wavelengths followed a k^{-2} power law as in the mixed layer, and in agreement with previous observations of the upper thermocline (Bernstein and White 1974; Strass 1992; Hodges and Rudnick 2006). Different isopycnals were in the remnant mixed layer in winter, spring, and

summer (Fig. 3.7b), and seasonal changes in θ_{iso} variance may result from isopycnals

that had recently restratified. Summer spectra were essentially identical when

vertically averaged over the density range of the spring remnant mixed layer, 24.5-

25.4 kg m^{-3}, and the summer remnant mixed layer, 24.0-25.4 kg m^{-3} (not shown).

Changes in θ_{iso} variance primarily represent changes that occurred in isolation from

surface forcing. Total variance was largest in spring, and a factor of 2 smaller in

winter and summer. At 30-46 km wavelengths, variance increased by a factor of 1.8

from winter to spring and decreased by a factor of 2.4 from spring to summer, both of

which are significant at the 90% confidence level (Table 3.4).

Effective isopycnal diffusivity is estimated by treating thermohaline structure

as a tracer. For any tracer C(x,t), we assume simple diffusion

$$\frac{dC}{dt} = \kappa_h \frac{d^2C}{dx^2} \tag{3.1}$$

with constant horizontal diffusivity κ_h. The tracer concentration at time $t+\Delta t$ is:

$$C(x,t+\Delta t) = \int \left(4\pi\kappa_h\Delta t\right)^{-1/2} \exp\left[-(x-x_0)^2/4\kappa_h\Delta t\right]C(x_0,t)dx_0 \tag{3.2}$$

Taking the Fourier transform of (3.2) simplifies the results, and the spectrum of the

tracer, $\hat{C}(k,t)$, obeys

$$\hat{C}(k,t+\Delta t) = \hat{C}(k,t)\exp\left[-2k^2\kappa_h\Delta t\right] \tag{3.3}$$

where k is wavenumber. The coefficient κ_h can be determined by a least squares fit to

(3.3) using observed spectra at two different times and knowing the time between

observations. Isopycnal diffusivity estimated in this way represents mixing along

isopycnals as well as the net effects of variance strained away to smaller scales and gained from straining at larger scales.

We use θ_{iso} as the tracer in (3.3) to estimate effective isopycnal diffusivity. Diffusivity is estimated where θ_{iso} variance decreased significantly: between spring and summer over 30-46 km wavelengths (Fig. 3.13). Over these wavelengths, the effective isopycnal diffusivity was 1.4 m^2 s^{-1} (Table 3.4), and represents the net effects of straining and isopycnal mixing between spring and summer. Estimates of isopycnal diffusivity at smaller scales in the thermocline from tracer release experiments are: 0.3-4.9 m^2 s^{-1} at 1-10 km scales along the New England continental shelf (Sundermeyer and Ledwell 2001), 0.6-6 m^2 s^{-1} at 1-30 km scales in the subtropical North Atlantic (Ledwell et al. 1998), and 15-60 m^2 s^{-1} at a 10 km scale in the subpolar North Atlantic (Messias et al. 2008). Our estimate of 1.4 m^2 s^{-1} over 30-46 km wavelengths is at the smaller end of this range.

3.6.3 High-Stratification Layer

Isopycnal θ-S variance in the high-stratification layer decreased at larger wavelengths between winter and spring and at smaller wavelengths between spring and summer (Fig. 3.13c). Between winter and spring, θ_{iso} variance was approximately constant at 30-100 km wavelengths and decreased at 100-370 km wavelengths. Between spring and summer, θ_{iso} variance decreased at 30-100 km wavelengths. Over 30-46 km wavelengths, variance increased slightly between winter and spring and decreased by a factor of 1.9 between spring and summer (Table 3.4). The decrease

between spring and summer is comparable to the remnant mixed layer but not significant at the 90% confidence level so we do not estimate effective isopycnal diffusivity in the high-stratification layer.

3.6.4 Permanent Thermocline

Isopycnal θ-S variance in the permanent thermocline was similar in winter and spring and increased between spring and summer (Fig. 3.13d). At 30-371 km wavelengths, total isopycnal θ-S variance decreased only slightly between winter and spring, and increased by a factor of 3 between spring and summer. At 30-46 km wavelengths, variance increased slightly from winter to spring to summer, but was not significant at the 90% confidence level (Table 3.4).

3.7 Summary and Conclusions

These observations show the seasonal evolution of upper-ocean thermohaline structure. Salinity and density sections showed four vertical regions with distinct properties: the mixed layer, remnant mixed layer, high-stratification layer, and permanent thermocline. The seasonal evolution of the remnant mixed layer is one of the most important results of this study. We discuss each layer below followed by final comments.

3.71. Mixed Layer

Most properties of the mixed layer varied seasonally. From winter to spring to summer, the mixed layer warmed because of surface heating and shoaled because of reduced vertical mixing. Heating causes evaporation, which increased mean salinity by 0.4 psu between spring and summer. In all seasons, salinity in the mixed layer was vertically uniform and horizontally variable. Horizontal differences increased between winter and spring, and decreased between spring and summer because large-scale surface forcing homogenized the mixed layer. Temperature variance decreased over all observed wavelengths, 30-371 km, between spring and summer because of large-scale surface forcing.

The horizontal density ratio in the mixed layer was consistent with theoretical predictions that compensation is strongest when vertical mixing is strongest and thermohaline gradients are largest (Young 1994; Young and Chen 1995; Ferrari and Young 1997; Ferrari and Paparella 2003; Boccaletti et al. 2007). Horizontal θ and S differences were approximately compensated in density in winter, and less likely to compensate in spring and summer. A strong tendency towards compensation for large thermohaline gradients was also observed.

3.7.2 Remnant Mixed Layer

Properties within the remnant mixed layer were set in winter and evolved seasonally as the remnant mixed layer became isolated from surface forcing. The remnant mixed layer was thin at the end of winter, and thickened between winter and spring as the mixed layer shoaled. Stratification within the remnant mixed layer

increased from winter to spring to summer because of weak vertical mixing with the warming mixed layer above. In summer, density surfaces were packed into the upper few meters of the remnant mixed layer effectively isolating the remnant mixed layer from surface forcing. Salinity was simply left behind during restratification causing a strong correlation between the mixed layer and remnant mixed layer in winter and spring. In summer, large-scale surface forcing changed the horizontal structure of the mixed layer so that it was no longer correlated with the remnant mixed layer. The vertical density ratio did not vary seasonally and a mode of R_ρ near 2.0 was always observed, which is consistent with salt-fingering. Isopycnal depth variance over 30-46 km wavelengths decreased from winter to spring to summer, consistent with internal waves and small eddies being most energetic in winter. Isopycnal temperature variance over 30-46 km wavelengths increased significantly between winter and spring and decreased significantly between spring and summer. Effective isopycnal diffusivity over 30-46 km wavelengths was estimated to be 1.4 m^2 s^{-1} between spring and summer, in agreement with smaller estimates from previous observations.

The remnant mixed layer is in the density range, 24.0-25.4 kg m^{-3}, and region of formation, centered at 30°N 140°W, for eastern North Pacific subtropical mode water (Hautala and Roemmich 1998; Ladd and Thompson 2000). This mode water is typically defined as a vertically uniform layer with a minimum in stratification. We observe such a minimum in stratification in the spring remnant mixed layer (compare our Fig. 3.1 to Fig. 2 of Hautala and Roemmich (1998) or to Fig. 10 of Sprintall and Roemmich (1999)). Stratification in our summer profiles is smoother with no

minimum. Our observations suggest that this mode water is re-entrained into the mixed layer each winter with permanent subduction occurring further to the south.

3.7.3 High-Stratification Layer

The high-stratification layer varied seasonally because it was influenced by the remnant mixed layer above. Like the remnant mixed layer, the high-stratification layer had horizontally variable salinity in all seasons. In winter, the high-stratification layer was isolated from and uncorrelated with the remnant mixed layer. Between winter and spring, vertical mixing occurred between the high-stratification layer and remnant mixed layer because (1) stratification within the high-stratification layer decreased and (2) the correlation of vertically averaged salinity between the two layers doubled. The vertical density ratio was always temperature dominated with a mode larger than in the remnant mixed layer, and so was not influenced by the remnant mixed layer. Isopycnal depth variance over 30-46 km wavelengths was also similar to the remnant mixed layer and decreased from winter to spring to summer. There were no significant changes in isopycnal temperature variance.

3.7.4 Permanent Thermocline

The permanent thermocline remained essentially unchanged. Salinity differences were smaller than in the layers above and correlated with the high-stratification layer as both regions experienced essentially the same internal wave activity and mixing. The vertical density ratio was temperature dominated and varied

little seasonally. Isopycnal θ-S variance did not change significantly between seasons. Only isopycnal depth variance over 30-46 km wavelengths changed seasonally and decreased from winter to summer as in the layers above.

3.7.5 Final Comments

We define four regions for convenience and to organize our discussion. These regions can be defined based solely on density and stratification, but are most useful because they correspond to changes in thermohaline structure. We used the same density surfaces in all seasons to define the remnant mixed layer and high stratification layer bases even though vertical mixing could change the densities of these surfaces. The isopycnals we chose are appropriate in all seasons (Fig. 3.4-3.6), and using a slightly different isopycnal, ± 0.1 kg m^{-3}, would not change our results significantly.

We take advantage of the thermohaline structure laid down in the winter mixed layer to estimate effective isopycnal diffusivity. Unlike a tracer release experiment where a passive tracer is released at one point in time or over a few days, there are sources and sinks of isopycnal θ-S variance throughout the year. Because isopycnal θ-S variance is simultaneously created and diffused, our estimates are minimum values. We observed a k^{-2} power law in isopycnal temperature spectra in all regions consistent with several observational (Bernstein and White 1974; Samelson and Paulson 1988; Strass 1992; Hodges and Rudnick 2006), and numerical (Capet et al. 2008; Klein et al. 2008; Bracco et al. 2009) studies. It is possible to calculate effective isopycnal diffusivity in all regions except the mixed layer, which is influenced by surface

forcing. We estimated effective isopycnal diffusivity only in the remnant mixed layer because the decrease in variance in the other layers was not significant at the 90% confidence level. Observations in all seasons and over a larger distance would allow us to verify when in the year variance is created and destroyed.

Our observations demonstrate the importance of the remnant mixed layer to large-scale subduction. Regardless of season, thermohaline structure is set at the surface and slowly homogenized as it subducts to deeper isopycnals. Surface forcing and horizontal stirring determine the characteristics of water in the mixed layer. The horizontal structure is simply left behind when the deep winter mixed layer restratifies. Water may spend many months in the remnant mixed layer, and is subsequently modified by isopycnal and vertical mixing. Only a small portion of water in the remnant mixed layer is permanently subducted to the layers below while the majority is mixed back into the mixed layer the following winter. We have shown how water is modified in the remnant mixed layer and how the relationships between the remnant mixed layer and regions above and below change seasonally, but our understanding is not complete. Multiple years of observations, including observations in fall when the remnant mixed layer is eaten away from above, would be desirable to verify seasonal changes and observe any differences between years.

Acknowledgements

Chapter 3, in full, is a

reproduction of the material as it appears in the Journal of Geophysical Research

Oceans, 2010, S. T. Cole, D. L. Rudnick, and J. A. Colosi, C04012. The dissertation

author was the primary investigator and author of this paper.

Table 3.1 Summary of Observations.

Section	Time of Observation	Instrument Platform[a]	Z_{min}[b] (m)	Z_{max}[b] (m)	Δx[c] (km)	Δt[c] (min)	Num. Profiles
June	06-10 June 2004	UCTD	5±0	389±42	10.5±2.2	30.8±5.8	96
September	15-23 Sept 2004	UCTD	5±0	342±45	13.4±5.3	32.6±7.3	72
March	24-27 March 2005	SeaSoar	21±10	323±35	3.4±0.3	14.0±1.6	293
March Subsampled	d	d	d	d	13.8±1.2	55.8±6.1	d
April	03-06 April 2005	SeaSoar	4±2	398±7	2.6±0.1	10.8±0.4	384
April Subsampled	e	e	e	e	10.3±0.3	43.3±1.5	e

[a] UCTD, underway CTD, is dropped and recovered from a moving ship, and SeaSoar is towed behind a ship.
[b] Z_{min} and Z_{max} are the section mean ± standard deviation of the minimum and maximum depths of the profiles.
[c] Δx and Δt are the section mean ± standard deviation of the distance and time between consecutive profiles. Time gaps of more than two hours are excluded.
[d] Same as March values.
[e] Same as April values.

Table 3.2 Correlations of vertically averaged salinity

Layers Correlated	Correlation of vertically averaged salinity		
	Winter	Spring	Summer
Mixed layer & Remnant mixed layer	0.82	0.84	0.40
Remnant mixed layer & High stratification layer	0.33	0.67	0.59
High stratification layer & Permanent thermocline[a]	0.95	0.88	0.76

[a] The permanent thermocline is an average over the 25.9-26.3 $kg\ m^{-3}$ isopycnals.

Table 3.3 Variance of isopycnal depth at 30-46 km wavelengths

	Z_{iso} variance (m^2)			Z_{iso} variance confidence interval[a] (m^2)		
	Winter	Spring	Summer	Winter	Spring	Summer
Remnant mixed layer	19.2	3.4	1.9	15.5-24.6	2.6-4.9	1.4-2.7
High stratification layer	8.4	3.3	3.2	6.8-10.8	2.5-4.7	2.4-4.5
Permanent thermocline[b]	9.8	6.9	4.6	7.9-12.6	5.2-9.7	3.4-6.6

[a] The 90% confidence interval for total variance over 30-46 km wavelengths.
[b] The permanent thermocline is an average over the 25.9-26.3 kg m^{-3} isopycnals.

Table 3.4 Statistics of θ_{iso} spectra at 30-46 km wavelengths.

	θ_{iso} variance ($°C^2 \times 10^3$)			θ_{iso} variance confidence interval[a] ($°C^2 \times 10^3$)			K_h[b] ($m^2 s^{-1}$)
	Winter	Spring	Summer	Winter	Spring	Summer	Spring to summer
Mixed layer	10.7	10.4	2.2	8.7-13.6	7.7-15.0	1.6-3.2	N/A
Remnant mixed layer	12.0	21.3	9.0	9.7-15.2	15.8-30.7	6.7-13.0	1.4
High stratification layer	7.3	8.2	4.4	5.9-9.3	6.1-11.7	3.2-6.3	N/A
Permanent thermocline[c]	1.9	2.0	2.2	1.5-2.4	1.5-2.9	1.6-3.1	N/A

[a] The 90% confidence interval for total variance over 30-46 km wavelengths.
[b] Diffusivity over 30-46 km wavelengths. K_h is shown only below the mixed layer where the 90% confidence levels do not overlap.
[c] The permanent thermocline is an average over the 25.9-26.3 kg m^{-3} isopycnals.
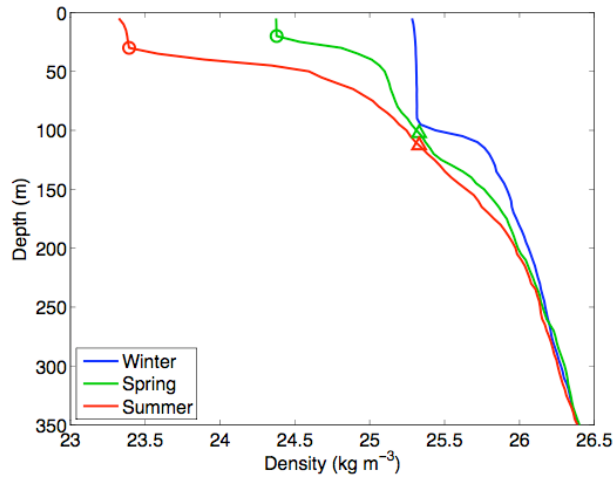
Figure 3.1 Profiles of density in the eastern North Pacific at 34.7°N, 147.0°W observed in winter, spring, and summer. Spring and summer profiles show a remnant mixed layer, which is the region between the MLB (circles) and the density of the previous winter's mixed layer (triangles). Density varies seasonally in the mixed layer, remnant mixed layer, and region just below.
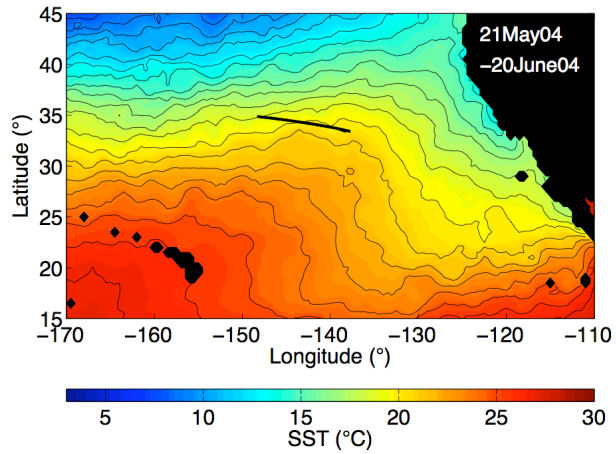
Figure 3.2 SST (color) and cruise track (black). SST is NOAA's 50 km gridded product from satellite observations given twice weekly. SST is averaged over 21 May 2004 – 20 June 2004 and contoured every 1°C.
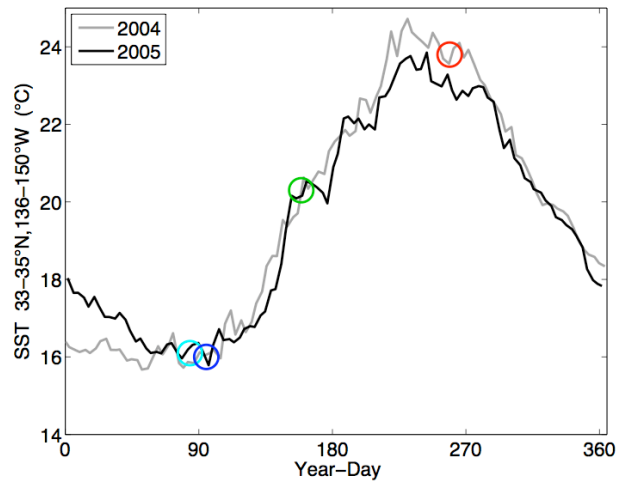
Figure 3.3 SST averaged over 33-35°N, 136-150°W for 2004 (gray) and 2005 (black). SST on 7 June 2004 (green), 17 September 2004 (red), 25 March 2005 (light blue) and 5 April 2005 (dark blue) are shown with circles.
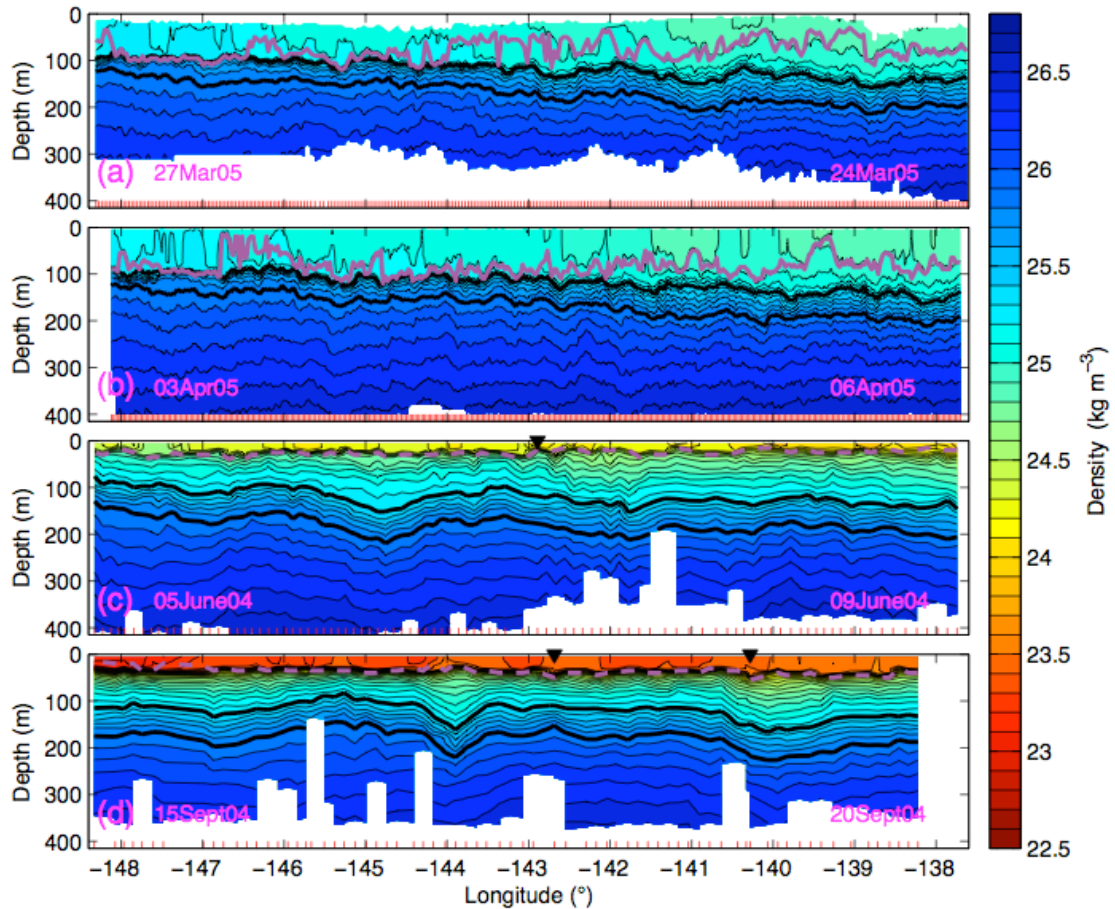
Figure 3.4 Sections of potential density in a) March, b) April, c) June, and d) September. The MLB (purple), 25.4 and 25.9 kg m^{-3} isopycnals (thick black) are indicated. The MLB is dashed in spring and summer to show the stratification. Times for the beginning and end of each section are shown in the lower corners. Gaps in time of more than three hours in June (1.8 days) and September (1.9 and 1.4 days) are indicated by black triangles at the surface. Red tick marks show the location of each profile. We define four regions: 1) the mixed layer extends from the surface to the MLB, 2) the remnant mixed layer extends from the MLB to the 25.4 kg m^{-3} isopycnal, 3) the high stratification layer is between the 25.4 and 25.9 kg m^{-3} isopycnals, and 4) the permanent thermocline lies below the 25.9 kg m^{-3} isopycnal.

Figure 3.5 Sections of salinity in a) March, b) April, c) June, and d) September. Tick marks, triangles, black and purple lines as in Figure 3.4. Times for the beginning and end of each section are shown in the lower corners. The 25.0 kg m^{-3} isopycnal (thin black line) is shown in spring and summer to illustrate that salinity varies along this isopycnal in the remnant mixed layer.
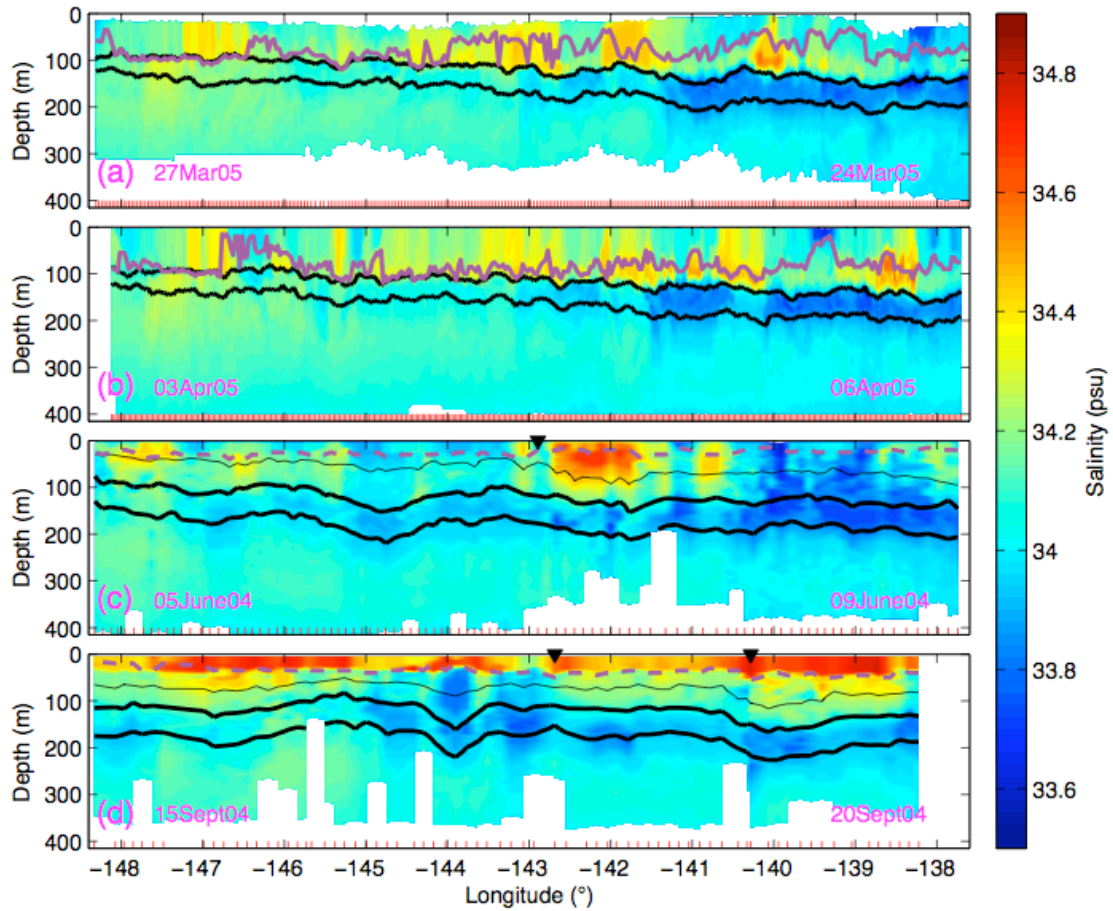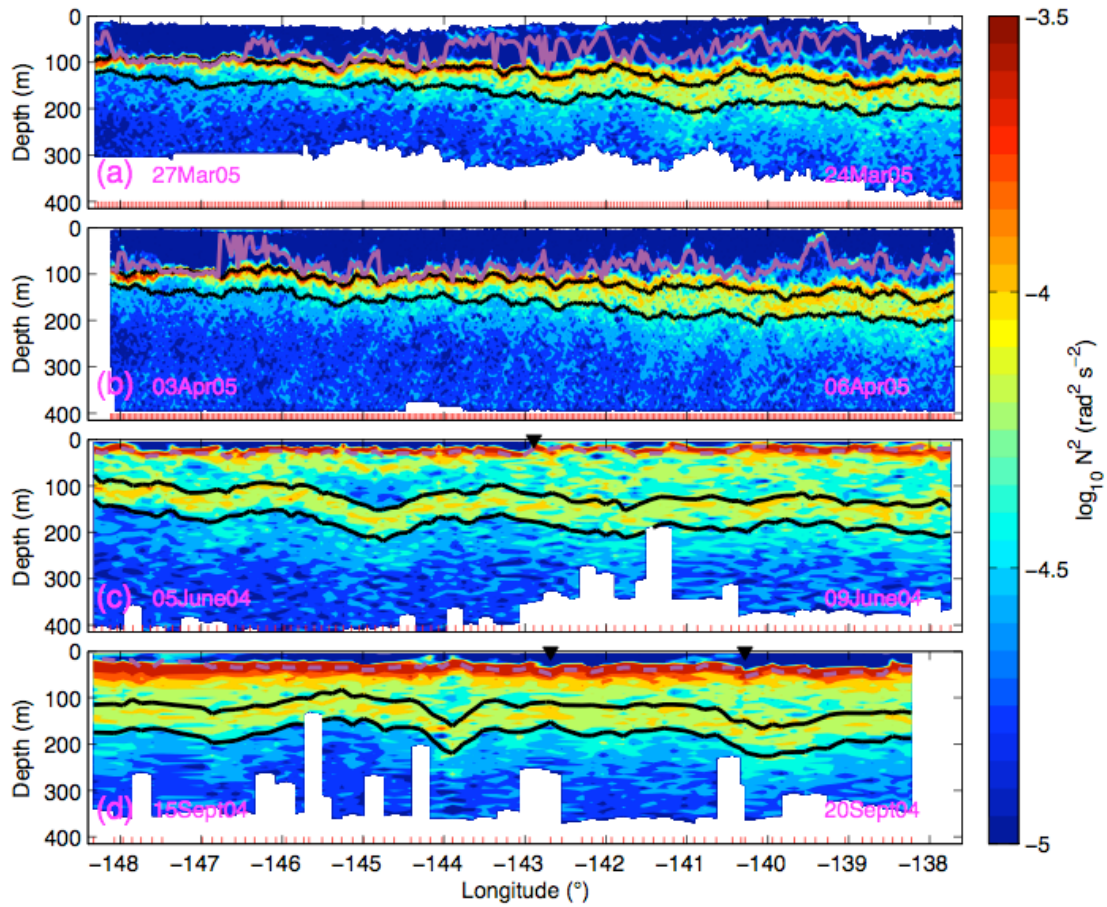
Figure 3.6 Sections of stratification in a) March, b) April, c) June, and d) September. Tick marks, triangles, black and purple lines as in Figure 3.4. Times for the beginning and end of each section are shown in the lower corners.
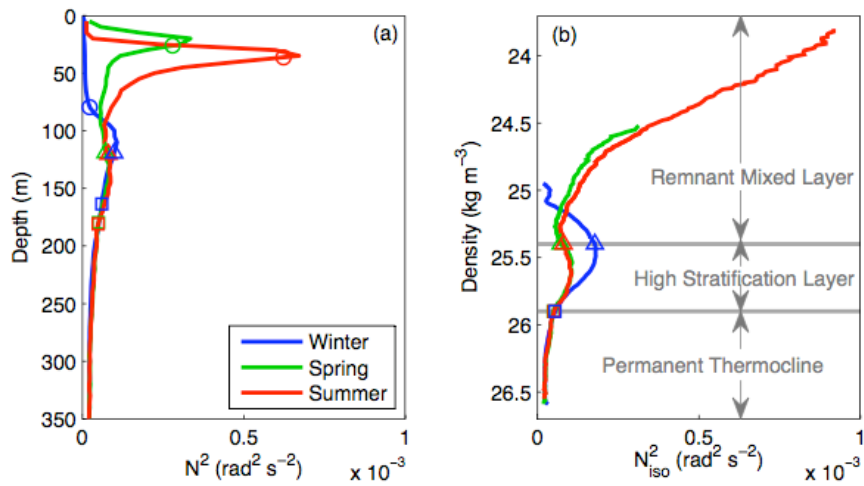
Figure 3.7 Section mean stratification a) along depth surfaces, and b) along density surfaces. March and April sections are combined into a single winter statistic. Symbols indicate the mean depth or density of the MLB (circles), 25.4 kg m^{-3} isopycnal (triangles), and 25.9 kg m^{-3} isopycnal (squares). In (b), the mixed layer is excluded from the calculation and shaded lines are at the 25.4 and 25.9 kg m^{-3} isopycnals.
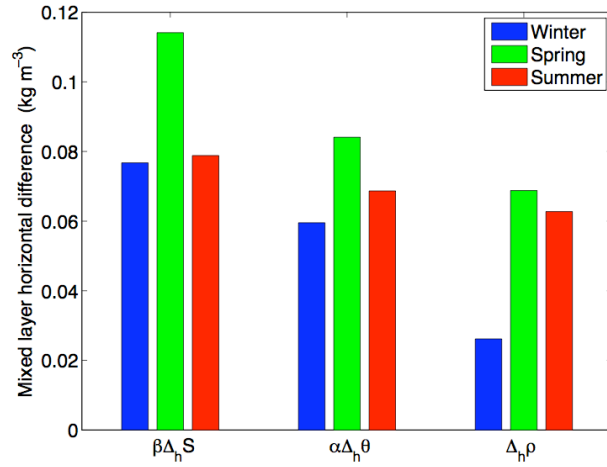
Figure 3.8 Standard deviations of $\beta\Delta_h S$, $\alpha\Delta_h\theta$, and $\Delta_h\rho$ in the mixed layer in winter, spring, and summer. March and April subsampled sections are combined into a single winter statistic.
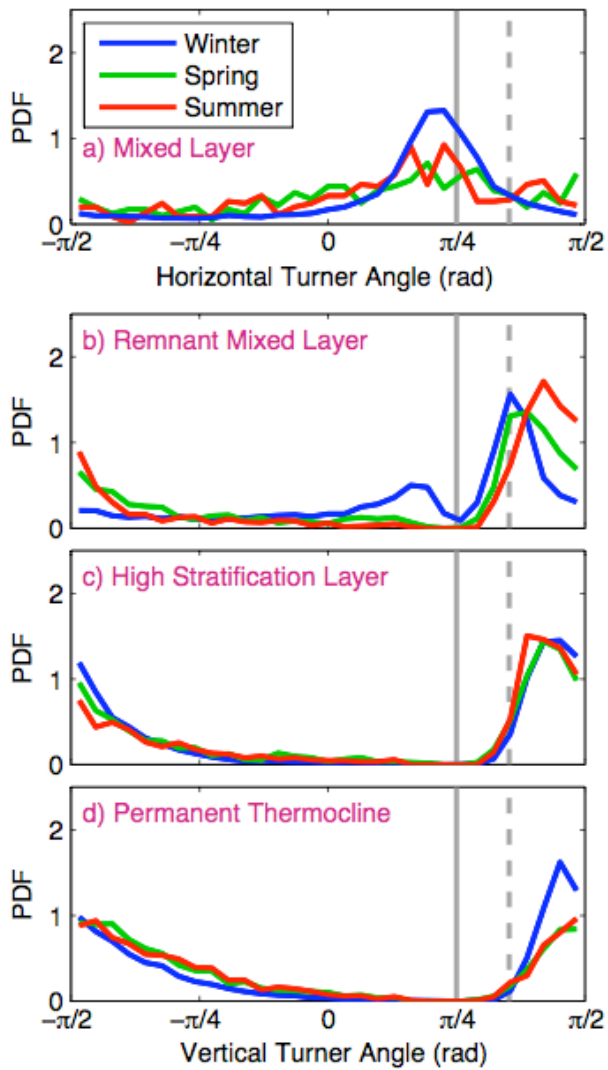
Figure 3.9 PDFs of a) horizontal Turner angle, $\tan^{-1}(R)$, in the mixed layer and b-d) vertical Turner angle, $\tan^{-1}(R_\rho)$, in the remnant mixed layer, high stratification layer, and permanent thermocline. Vertical gray lines correspond to Turner angles of $R=1$ or $R_\rho=1$ (solid) and $R=2$ or $R_\rho=2$ (dashed). March and April subsampled sections are combined into a single winter statistic. The permanent thermocline is an average over the 25.9-26.3 kg m^{-3} isopycnals.
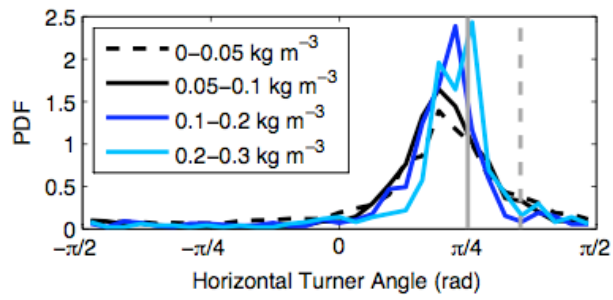
Figure 3.10 PDFs of horizontal Turner angle in the winter mixed layer for different sizes of the thermohaline difference. March and April subsampled sections are combined into a single winter statistic. Shaded lines as in Fig. 3.9.
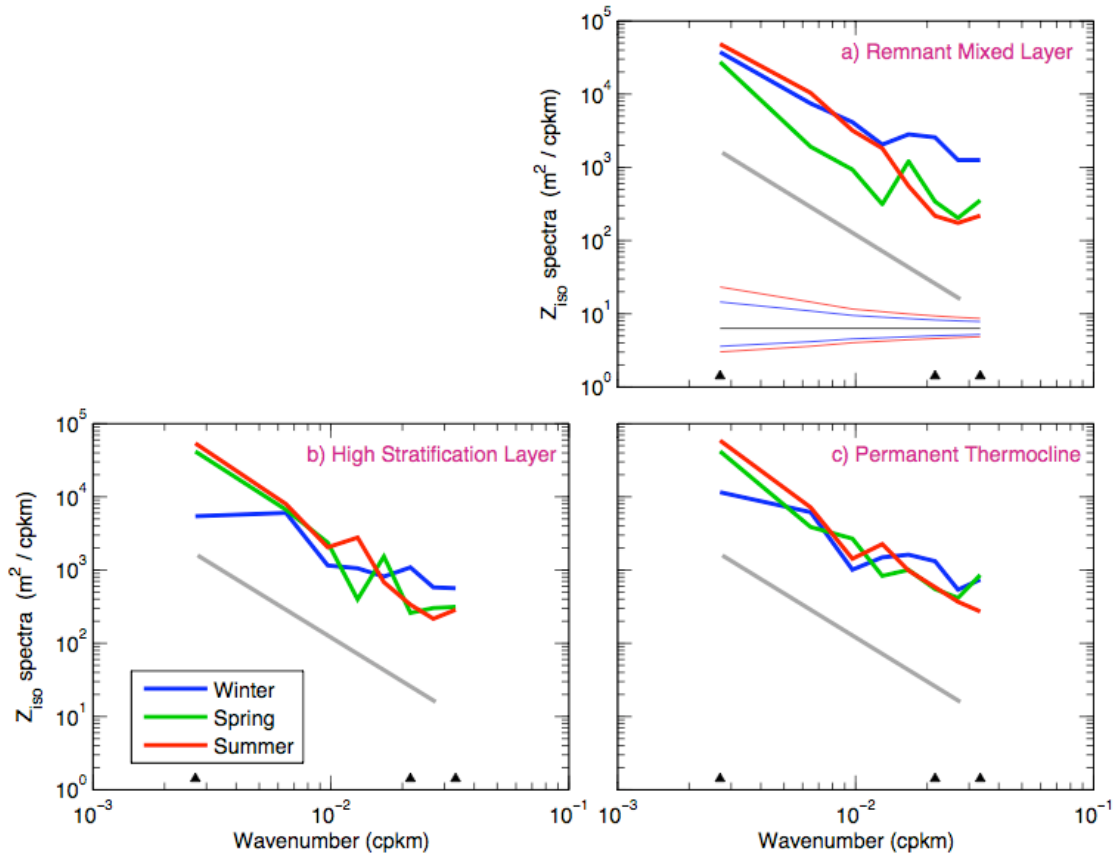
Figure 3.11 Vertically averaged spectra of isopycnal depth in a) the remnant mixed layer, b) the high stratification layer, and c) the permanent thermocline. The permanent thermocline is an average over the 25.9-26.3 kg m^{-3} isopycnals. The gray line shows a slope of k^{-2}. Winter spectra are an average of March and April spectra and have twice the degrees of freedom as spring or summer spectra. In (a), the thin lines show the 90% confidence interval in winter (blue), and in spring and summer (red). Triangles correspond to 30, 46, and 371 km wavelengths.
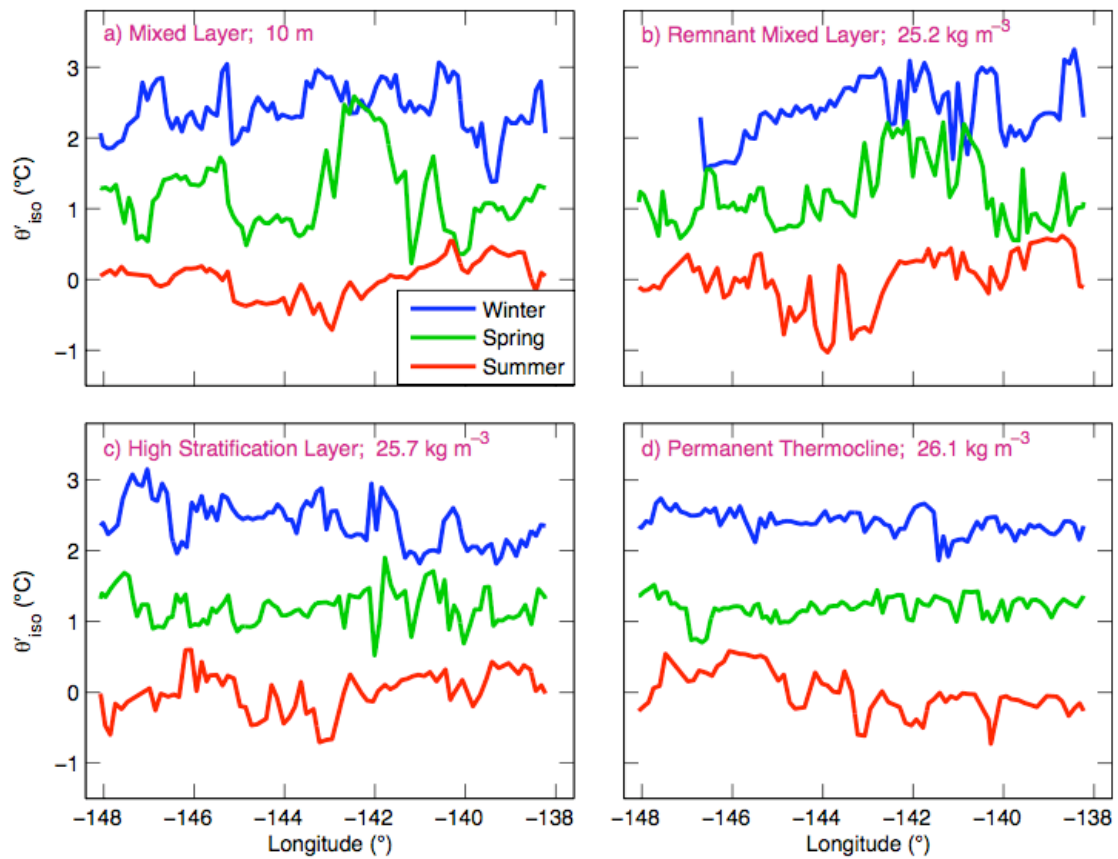
Figure 3.12 θ_{iso} perturbations, after removal of a mean and trend, for a) the mixed layer at 10 m depth, b) the remnant mixed layer along the 25.2 kg m^{-3} isopycnal, c) the high stratification layer along the 25.7 kg m^{-3} isopycnal, and d) the permanent thermocline along the 26.1 kg m^{-3} isopycnal. The vertical offset is 1.2°C in spring and 2.4°C in winter. One subsampled April section is shown for winter.
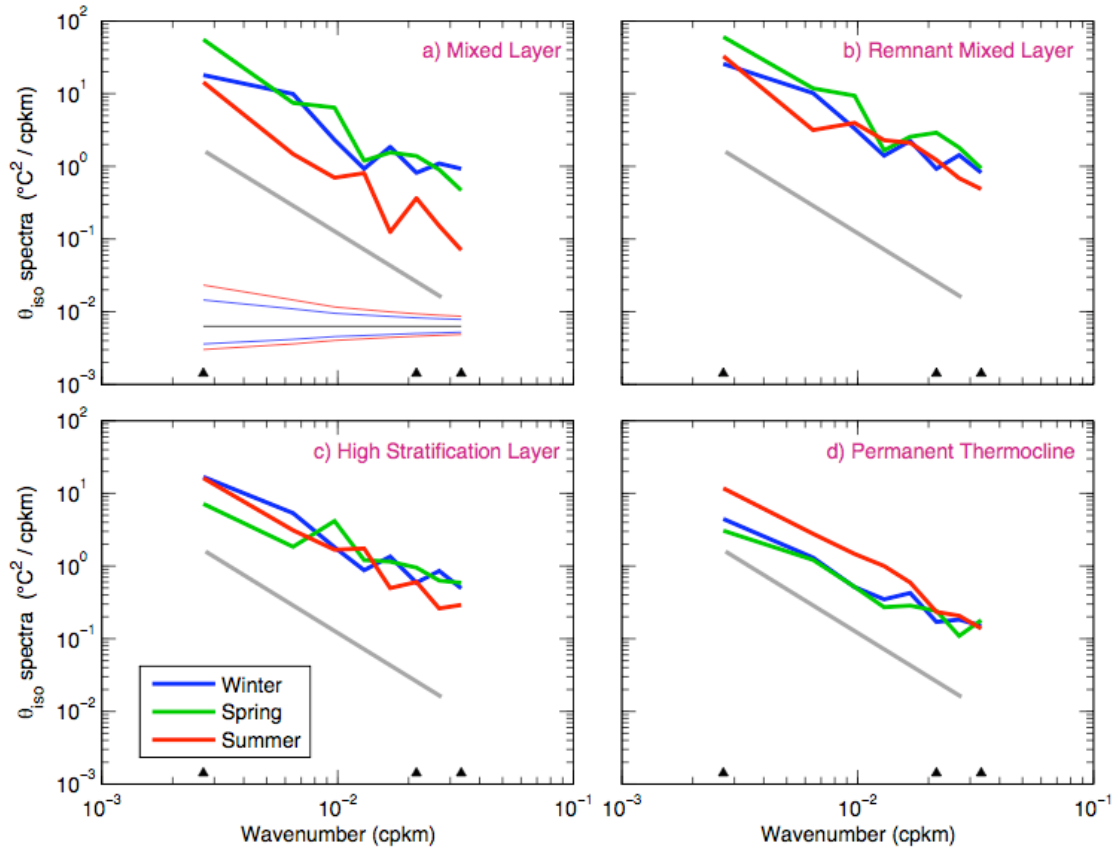
Figure 3.13 Vertically averaged spectra of temperature along depth surfaces in a) the mixed layer, and temperature along isopycnals in b) the remnant mixed layer, c) the high stratification layer, and d) the permanent thermocline. The permanent thermocline is an average over the 25.9-26.3 kg m^{-3} isopycnals. Winter spectra are an average of March and April spectra. Triangles, shaded lines, and confidence intervals as in Fig. 3.11. Above the permanent thermocline, variance decreased from winter to spring to summer at 30-60 km wavelengths.

Chapter 4

Spatial and Temporal Modulation of Thermohaline Structure

Abstract of Chapter 4

Autonomous gliders measured temperature and salinity along a north-south section in the central subtropical North Pacific for 2.5 years. Thermohaline variability was observed on depth and density surfaces at a range of horizontal scales from 5 to 1300 km. Thermohaline fluctuations along isopycnals, which are density compensated fluctuations referred to as spice, were elevated near the surface, near the subtropical frontal regions, near 300 m depth, and towards one end of the section at 500-1000 m depth. The complicated geography of these spice fluctuations persisted over the observation period and reflected the history of horizontal stirring and mixing. Spice variance had local extrema in the vertical because of differences in water age and source water properties, as well as the influence of neighboring water masses. Spice variance spanned about three orders of magnitude along deeper isopycnals with larger variance near where different water masses met. An elevated large-scale thermohaline gradient available to stir and increased stirring were also observed in the higher variance region. Thermohaline structure was temporally modulated in the mixed layer and remnant mixed layer. In the mixed layer, thermohaline structure was modulated with season and year. In the remnant mixed layer, thermohaline fluctuations were left

behind during restratification and decayed with time because of along isopycnal mixing once isolated from the mixed layer. Effective horizontal diffusivity estimates in the remnant mixed layer were 0.4 m^2 s^{-1} at 15-23 km wavelengths and 0.9 m^2 s^{-1} at 28-45 km wavelengths.

4.1 Introduction

Thermohaline structure on depth and density surfaces is affected by surface forcing, tilting isopycnals, mixing, and horizontal stirring. In the mixed layer, surface forcing and vertical mixing with water below can create thermohaline fluctuations, which are then enhanced by horizontal stirring and weakened by horizontal mixing. During restratification, thermohaline structure is left behind as temperature and salinity fluctuations along isopycnals exactly compensated in density (Cole et al. 2010). Such hot and salty or cold and fresh fluctuations are referred to as spice (Veronis 1972; Munk 1981), are enhanced by horizontal stirring, and are weakened by along isopycnal mixing. Spice fluctuations are advected throughout the ocean and serve as a tracer provided by nature. Assuming that older deeper waters have been mixed more than shallower younger waters, spice variance would simply decrease with depth. On depth surfaces, thermohaline structure results from fluctuations along isopycnals as well as tilting isopycnals that project vertical temperature and salinity gradients into horizontal fluctuations. Tilting isopycnals are caused by internal waves on order 1-10 km scales and geostrophically balanced motions on order 1-1000 km scales.

Autonomous gliders allow the geography and persistence of thermohaline structure to be studied. Gliders can sample to 1000 m depth with 5-6 km horizontal resolution over periods from months to years. Continuous glider observations in the same location for at least one year began in 2003 and focused on coastal regions (Davis et al. 2008; Perry et al. 2008; Castelao et al. 2010; Todd et al. 2010). Previous observations of 1-10 km horizontal scales have been limited to the upper 400 m of the ocean and 1-3 time periods during the year (Weller 1991; Strass et al. 1992; Joyce et al. 1998; Rudnick and Ferrari 1999; Ferrari and Rudnick 2000; James et al. 2002; Cole et al. 2010). We present 2.5 years of sustained observations from a 1300 km line north of Hawaii that represent conditions in the middle of a subtropical gyre.

Example sections of temperature along isopycnals show that spice fluctuations in the upper 1000 m and over a 1300 km distance had a complicated geography (Fig. 4.1). In both example sections, layers with elevated spice fluctuations were observed shallower than 25.0 kg m^{-3}, near 26.0 kg m^{-3}, and near 27.0 kg m^{-3} south of 28°N. Regions with small spice fluctuations surrounded these layers so that local extrema in spice variance were stacked in the vertical. Horizontal variability was also observed with spice fluctuations near 27.0 kg m^{-3} larger at 24°N than at 34°N for example. The spatial modulation of spice fluctuations, determined by the initial thermohaline structure and history of stirring and mixing, was a persistent feature of the ocean since the example sections were observed more than 1.5 years apart.

Because of the glider's 5 km horizontal resolution, submesoscale thermohaline structure is observed. The term submesoscale refers to a distinct dynamical range, with

order one Rossby and Richardson numbers, order 1-10 km horizontal scales, nearly geostrophic flow, and large vertical velocities (McWilliams 1985; Mahdevan and Tandon 2006; Klein and Lapeyre 2009). Submesoscale features include sharp frontal regions and the edges of eddies or filaments. With improvements in numerical modeling, submesoscale features are becoming the most important features to be parameterized. The abundance of spice fluctuations observed at the submesoscale (Fig. 4.1) gives information about stirring and mixing taking place at these scales.

This paper addresses the geography and persistence of thermohaline structure and its relationship to horizontal stirring and mixing. Observations and methods are described in Section 4.2. The spatial modulation of thermohaline structure is addressed in Section 4.3. The temporal modulation of thermohaline structure is addressed in Section 4.4. A summary and conclusions are in Section 4.5.

4.2 Observations and Methods

Observations were taken using Spray gliders, an autonomous platform (Sherman et al. 2001; Rudnick et al. 2004). Gliders dove to pre-programmed depths and measured temperature and salinity with 1 m vertical resolution during the ascent. While diving, gliders traveled horizontally through the water at about 0.25 m s^{-1} towards predetermined locations. While at the surface between each dive, location was determined using the global positioning system (GPS) through the iridium satellite system.

Gliders sampled north of Hawaii along 158°W from 22.75-34.5°N between July 2007 and December 2009 (Fig. 4.2). The glider section was in the center of the subtropical gyre, began at station ALOHA (22.75°N, 158°W), a site with monthly observations since 1989 (Karl and Lukas 1996), and crossed the salinity maximum region. Eight glider deployments, each lasting 3-4 months, gave 16 sections of temperature (θ) and salinity (S) to 1000 m depth and a total of 3328 profiles (Table 4.1). Each 1000 m dive had a mean ± standard deviation of 5.8±0.3 hours in time and 5.4±1.1 km in the horizontal. Raw profiles were averaged into 10 m vertical bins. Properties along isopycnals, denoted as X_{iso} for any variable X, were calculated by linear interpolation. Four deployments did not reach 34.5°N because of operational reasons including strong or opposing currents (3 July – 8 Sept 2007; 5 April – 7 Jul 2008; 13 April – 3 Jul 2008; 27 Aug – 17 Dec 2009). Two gliders occupied the line simultaneously in April – May 2008.

The section was observed almost continuously over the 2.5 year time period (Fig. 4.3). Gliders were deployed and recovered just offshore of Oahu taking slightly different paths to 22.75°N each time. The time gap with no glider north of 22.75°N was 13-28 days excluding the 72 days between the first and second deployments. Because gliders sampled with ~ 4 months between observations at either end of the section and ~ 2 months near the middle of the section, observations were more evenly spaced throughout the year near the middle of the section. Sometimes, the section was observed in different years less than one month apart (May 2008 and May 2009; Jan

2008 and Jan 2009). Statistics calculated over all sections are representative of statistics over all seasons.

Example salinity sections in winter 2007-2008 and summer 2009 show seasonal changes and variability on a range of horizontal scales (Fig. 4.4). The mixed layer was 10 m deep in June, deepened to 60 m in August, and was as deep as 100 m in Nov-Jan. The two subtropical frontal regions of the North Pacific were evident as mixed layer salinity gradients and will be referred to as the 25°N and 32°N frontal regions. In both sections, the region of highest salinity was from 25-29°N in the mixed layer between the frontal regions. The minimum in salinity from 500-650 m depth is North Pacific Intermediate Water (NPIW; Talley 1993). Horizontal salinity fluctuations were evident on depth and density surfaces, particularly in the upper 400 m. Seasonal or interannual changes in upper ocean salinity were also evident.

Gliders observe vertically averaged horizontal velocity, from which geostrophic velocity is referenced. Dead reckoning of glider position provides depth averaged horizontal currents, u and v, for each dive. Eastward geostrophic velocity, U_{geo}, is objectively mapped with a 40 km lengthscale from the density gradient with u providing a reference value. A 40 km lengthscale is used to focus on larger-scale currents and remove aliased internal wave variability. Because gliders profile relatively slowly, taking 5.8 hours between dives, the Nyquist frequency falls within the internal wave band. As gliders move 5.4 km between dives, internal waves are aliased into wavenumbers higher than about 0.03 cycles km^{-1} (Rudnick and Cole 2010). The 40 km mapping scale is sufficient to filter this aliased variability. Only

profiles north of 22.75°N are used in mapped fields. Example sections of geostrophic velocity show surface intensified flows with alternating east-west velocities across the section (Fig. 4.5).

Statistics from all sections are combined using 25 km horizontal bins on depth and density surfaces. Each bin includes 4-5 profiles with the mean and variance within each bin denoted as X_{bar} and X_{var}, respectively, for any variable X. Mean fields are the mean over all sections of X_{bar} and are denoted as ave(X_{bar}). Variance at scales greater than 25 km and one day is the variance over all sections of X_{bar}, denoted as var(X_{bar}), and referred to as mesoscale variance. Variance at scales less than 25 km and one day is the mean over all sections of X_{var}, denoted as ave(X_{var}), and referred to as submesoscale variance. Only bins with at least 5 sections in the mean or variance are considered. There are 16 sections south of 30°N, with at least 8 sections to the north. The minimum density of the mixed layer varies over the year, so there are fewer sections on isopycnals less than 25.1 kg m^{-3}.

4.3 Spatial Modulation of Thermohaline Structure

Thermohaline structure on depth surfaces (Fig. 4.4) and density surfaces (Fig. 4.1) resulted from different processes and so had different spatial modulations. On depth surfaces, tilting isopycnals caused thermohaline fluctuations on a range of horizontal scales (Fig. 4.4). The numerous 5 km scale fluctuations were associated with internal waves and geostrophically balanced submesoscale features. The order 10-100 km scale fluctuations were associated with larger internal waves, and larger

geostrophically balanced features such as eddies and the subtropical fronts. The larger-scale tilt of the general circulation was also evident. On density surfaces (Fig. 4.1), layers of elevated thermohaline fluctuations were evident and persistent over the 2.5-year observation period. Large fluctuations were near the surface, the subtropical frontal regions, the 26.0 kg m^{-3} isopycnal, and the 27.0 kg m^{-3} isopycnal south of 28°N. To show the spatial modulation of thermohaline structure, salinity variance was calculated over all sections on both depth and density surfaces (Fig. 4.6). On depth surfaces, salinity variance spanned about three orders of magnitude and had a similar spatial pattern at mesoscales and submesoscales (Fig. 4.6a-b). On density surfaces, salinity variance spanned about four orders of magnitude, and was also similar at mesoscales and submesoscales (Fig. 4.6c-d). Salinity variance on depth and density surfaces had different spatial patterns and so has been considered separately in the following two subsections. Isopycnal salinity variance above 26.2 kg m^{-3} with vertically staked layers of variance has also been considered separately from the region below where a gradual decrease in variance towards the north was observed.

4.3.1 Depth Surfaces

On depth surfaces, tilting isopycnals projected vertical salinity gradients into horizontal salinity fluctuations (Dzieciuch et al. 2004). The strength of horizontal salinity fluctuations depended on the size of the isopycnal tilt and the size of the vertical salinity gradient that was tilted. Salinity variance was similar to the vertical salinity gradient with large variance in the layer of tightly packed salinity surfaces that

outcropped in the 32°N frontal region, and small variance in the salinity minimum region where the vertical salinity gradient was weak (Fig. 4.6a-b). At scales greater than 25 km and one day, tilting isopycnals resulted from larger internal waves and geostrophically balanced motions. Seasonal changes in isopycnal depth or salinity contributed to salinity variance as well, and caused the elevated variance above the winter mixed layer base. At scales less than 25 km and one day, tilting isopycnals resulted from internal waves and geostrophically balanced motions, as well as internal waves with similar to 6 hour timescales for which temporal variability was aliased into horizontal variability. Salinity variance on depth surfaces resulted from the effects of tilting isopycnals as well as compensated fluctuations along isopycnals. Where salinity variance had comparable magnitudes on depth and density surfaces, for example below the salinity minimum near 24°N, the effects of fluctuations along isopycnals were significant. Salinity variance on depth surfaces was larger at mesoscales than submesoscales, indicating that the effects of mesoscale tilting, internal waves, and seasonal changes were larger than submesoscale tilting and internal waves, especially in the upper 300 m.

4.3.2 Density Surfaces

By considering salinity along isopycnals, internal wave effects are explicitly filtered and only compensated temperature and salinity fluctuations remain. Spice fluctuations are imprinted along isopycnals during mixed layer restratification from thermohaline fluctuations along depth surfaces (Cole et al. 2010). As spice

fluctuations are advected through the ocean, they are weakened by along-isopycnal

mixing and enhanced by horizontal stirring. The strength of the gradient available to

stir and the strength of stirring determine the resulting horizontal gradient. Vertical

mixing can also alter fluctuations where neighboring regions have different

thermohaline characteristics. The geography of spice fluctuations depends on the

thermohaline structure of the subduction region, strength of stirring and mixing, spice

gradient available to stir, and spice fluctuations of nearby water.

4.3.2.1 Shallower than 26.2 kg m^{-3}

A single layer of spice variance was observed above the base of the winter

mixed layer (Fig. 4.6c-d). The remnant mixed layer, or region left behind after

restratification, had the largest variance of any region, and had vertically correlated

fluctuations (Fig. 4.1 for example) with similar magnitudes (Fig. 4.6c-d). Large

vertically correlated spice fluctuations most likely resulted from thermohaline

structure inherited from the mixed layer during restratification. Mesoscale variance

was approximately uniform with latitude (Fig. 4.6c), while submesoscale variance was

about an order of magnitude larger near the 25°N and 32°N frontal regions than in

between (Fig. 4.6d).

Layers of spice variance were observed between the base of the remnant mixed

layer and 26.2 kg m^{-3} (Fig. 4.6c-d). South of 30°N, two layers of large variance

centered at 25.0 and 25.8 kg m^{-3} surrounded a layer of small variance centered at 25.3

kg m^{-3}. North of 30°N, a single layer of elevated variance encompassed the 25.0-26.2

kg m^{-3} density range. Variance within each layer was approximately constant with latitude, with the winter mixed layer base and uppermost layer increasing in density towards the north. The three layers of variance over 22.75-30°N had different vertical thicknesses, with the top layer of elevated variance about 100 m thick, the middle layer of low variance about 30-50 m thick, and the bottom layer of elevated variance about 150 m thick.

An empirical orthogonal function (EOF) analysis shows where salinity fluctuations were vertically correlated. The 22.75-30°N region was considered where three layers of spice variance were observed (Fig. 4.6c-d). Submesoscale perturbations were considered, where S$_{iso}$ objectively mapped with a 25 km lengthscale had been removed. The first and second EOFs of S'_{iso} peaked at 24.9 and 25.8 kg m^{-3}, respectively, and did not overlap significantly in density (Fig. 4.7a). These peaks coincided with the layers of high variance at 25.0 kg m^{-3} and 25.8 kg m^{-3} indicating that perturbations were uncorrelated between the layers. Perturbations were aligned in the vertical between the different layers as the first EOF of $\left|S'_{iso}\right|$ encompassed the entire 24.8-26.2 kg m^{-3} density range (Fig. 4.7b). Perturbations will be aligned but not correlated when they were initially different but have been stirred by the same velocity field (Ferrari and Paparella 2003; Hodges and Rudnick 2006). Over 30-34.5°N, EOFs of S'_{iso} and $\left|S'_{iso}\right|$ show that the single layer of variance was vertically correlated and aligned (not shown).

An extreme example of spice fluctuations is from an eddy observed near 30°N (Fig. 4.8). The subsurface cyclonic eddy was about 200 km in diameter and extended

to greater than 600 m depth (Fig. 4.8a). The strongest flow of more than 12 cm s^{-1} was at 300 m depth and 26.0 kg m^{-3}. The center of the eddy coincided with spice fluctuations: at 26.0 kg m^{-3}, temperature in the core of the eddy was more than 1°C colder than to either side of the eddy (Fig. 4.8b). Spice fluctuations were observed over 25.6-26.2 kg m^{-3}, coincident with the layer of elevated variance centered at 25.8 kg m^{-3}. Colder and fresher water along isopycnals suggests an origin towards the north. Eddies such as this one stir the ocean and enhance spice fluctuations.

Age differences between the spice variance layers were investigated using oxygen observations. Older water has lower spice variance because it has been mixed for a longer time period, suggesting that the low variance layer at 25.3 kg m^{-3} was older than the high variance layer below at 25.8 kg m^{-3} (Fig. 4.6c-d). Profiles of mean oxygen along isopycnals, from monthly observations at station ALOHA (22.75°N, 158°W; Karl and Lukas 1996) averaged over 2007-2009 and from a hydrographic section along 152°W (http://whpo.ucsd.edu) averaged over 23-29°N, had a local minimum at 25.3 kg m^{-3} and a local maximum at 26.0 kg m^{-3} (Fig. 4.9a). The correspondence between oxygen and spice variance extrema suggests that the spice variance layers had different histories. The oxygen minimum in particular, while close to the winter mixed layer base and possibly influenced by biological processes, is consistent with the low variance layer at 25.3 kg m^{-3} being slightly older than water below. Older water above younger water may result from a slower rate of subduction and advection for the 25.3 kg m^{-3} layer, or a longer path over which water was

advected to our section. Differences in water age may explain or contribute to the observed layering in spice variance.

The vertical component of potential vorticity, $N_{iso}^2 f/g$, from our observations also had vertical extrema coincident with the layers of spice variance (Fig. 4.9b). A local maximum in potential vorticity near 25.3 kg m^{-3} coincided with the low spice variance layer. A local minimum near 26.2 kg m^{-3} was at the base of the deeper layer of elevated spice variance, and was stronger towards the north end of the section. The extrema in $N_{iso}^2 f/g$ also indicate that the spice variance layers had different histories.

Differences in spice fluctuations at the subduction region could cause the observed layering in spice variance. From a data assimilating numerical model, salt content over 200-600 m depth at station ALOHA was most sensitive to perturbations to the east and north tracing back the gyre circulation (Stammer et al. 2008). Analyses of climatological data (Bingham et al. 2002) and ARGO float data (Oka et al., 2010) found a similar results with the 26.0 kg m^{-3} isopycnal outcrop near the Kuroshio extension. It is plausible that the 26.0 kg m^{-3} surface waters near the Kuroshio extension had larger thermohaline fluctuations than the 25.3 kg m^{-3} surface waters closer to the center of the gyre, and that this initial signal was observable some years later after subduction. The isopycnal layers identified solely from spice variance also corresponded to distinct water masses further to the north. The 24.0-25.4 kg m^{-3} water corresponded to eastern North Pacific subtropical mode water, and the 25.5-26.2 kg m^{-3} water corresponded to shallow salinity minimum water or North Pacific central water (Yuan and Talley 1992; Hautala and Roemmich 1998; Suga et al. 2004; MacDonald et

al. 2009; Oka et al. 2010). The distinction in water mass properties further to the north suggests that the 25.3 and 25.8 kg m^{-3} layers could have had different origins with different thermohaline structure. The initial spice fluctuations that were subducted may explain or contribute to the observed layering in spice variance.

Vertical mixing between two neighboring layers with uncorrelated fluctuations can result in a layer in between with smaller fluctuations. When water age initially increases with depth, the smaller fluctuation layer in the middle will not be older than water below. As the two observed layers with large spice fluctuations were uncorrelated in the vertical (Fig. 4.7a), vertical mixing may explain or contribute to the smaller spice variance near 25.3 kg m^{-3}.

In summary, three factors may have contributed to the layer of small spice variance near 25.3 kg m^{-3}. First, the initial thermohaline structure subducted over 24.8-26.2 kg m^{-3} may have been similar, but the low variance layer may benn older than water below. Older water above younger water may have resulted from advection along different paths to reach 158°W, or subduction and advection at different rates. Second, the initial spice variance subducted may have been different with smaller variance near 25.3 kg m^{-3}, which was then advected to 158°W. Third, the age and amount of spice variance subducted over 24.8-26.2 kg m^{-3} may have been similar, with the layer of low variance developing as uncorrelated fluctuations mixed in the vertical. All of these scenarios would affect mesoscale and submesoscale fluctuations and may have occurred simultaneously.

4.3.2.2 The 26.2-27.2 kg m^{-3} density range

A single layer of spice variance was observed below 26.2 kg m^{-3} with a decrease in variance towards the north (Fig. 4.6c-d). Over most latitudes, the smallest spice variance was observed below 26.2 kg m^{-3} most likely because this water was older and fluctuations had been slowly mixed away in the horizontal. The 26.2-27.2 kg m^{-3} density range is estimated to be from 10 to 50 years old (Watanabe et al. 1994; Warner et al. 1996; Fine et al. 2001; Bullister et al. 2006), with water below 26.8 kg m^{-3} formed outside the North Pacific (Reid 1997; MacDonald et al. 2009). Spice fluctuations were not correlated with the region above (Fig. 4.7a), but were correlated over the at least 26.4-27.2 kg m^{-3} (not shown), indicating that this region consists of a single layer of spice fluctuations. Fluctuations were vertically aligned, and so stirred by the same velocity field, over the entire water column (EOF$_1$ of $|S'_{iso}|$; Fig. 4.7b). The gradual decrease in spice variance from south to north that spanned three orders of magnitude (Fig. 4.6c-d) is investigated below.

Based on velocity and geostrophic vorticity fields, stirring was enhanced near the southern end of the section (Fig. 4.10). The standard deviation of vertically averaged velocity was smallest near 34.5°N and increased towards the south with a larger increase for northward velocity (Fig. 4.10a). An increase in variability towards the south is consistent with previous velocity and dynamic height observations in the region (Talley and DeSzoeke 1986; Hall et al. 1997; Chen and Qiu 2010). Variance of the observed component of geostrophic relative vorticity, dU$_{geo}$/dy, was also smallest near 34.5°N at all depths and increased towards the south (Fig. 4.10b). Variability

increased towards the south for u, v, and dU_{geo}/dy when only the 8 sections that covered the entire latitude range were considered (not shown), and was not a result of the sampling pattern. The larger amount of stirring contributed to the enhanced spice variance near the southern end of the section.

The increased spice variance near 22.75°N was associated with the weakening of the NPIW salinity minimum. Example sections of S_{iso} (Fig. 4.11) had abrupt changes in the salinity, depth, and density of the salinity minimum south of 28°N. Spice fluctuations larger than 0.07 psu (0.4°C) over 6 km were observed. The southern end of the section was where NPIW met warmer and saltier equatorial waters (Bostock et al. 2010), which caused an enhanced large-scale gradient available to stir. The same amount of stirring would produce larger fluctuations south of 28°N where mean salinity surfaces crossed mean density surfaces than to the north where mean salinity and density surfaces were nearly parallel (Fig. 4.6d).

The increased spice variance near 22.75°N resulted from a larger amount of stirring and an enhanced gradient available to stir. Water age cannot account for the observed north-south trend in spice variance because smaller fluctuations were observed towards the north where NPIW was younger (Talley 1993; Watanabe et al. 1994). Differences in the amount of spice variance subducted would probably not cause along isopycnal changes in spice variance, and had most likely been stirred and mixed away before reaching this density range and water age. The increased stirring and gradient available to stir caused the abundance of submesoscale structures that can lead to mixing and erosion of the salinity minimum.

4.4 Temporal Modulation of Thermohaline Structure

4.4.1 Mixed Layer

The mixed layer was primarily seasonally modulated with smaller interannual differences also observed (Fig. 4.12). Mixed layer depth as well as θ and S at 10 m depth were mapped with a 40 km lengthscale and 120 day timescale to focus on seasonal and interannual modulations, and eliminate temporal variability aliased into spatial variability at scales smaller than 40 km. Seasonally, the lowest temperatures and salinities at all latitudes occurred in Dec-Mar coincident with the deepest mixed layers. The shallowest mixed layers occurred in May, and the warmest temperatures in August. Salinity was also highest in August because the warm temperatures caused excess evaporation. The 32°N subtropical frontal region, as seen in salinity, extended farther north in summer during periods of maximum heating and was smaller in magnitude or more horizontally broad in winter, consistent with previous studies (White et al. 1978; Kazmin and Rienecker 1996; Dinniman and Rienecker 1999). The 25°N subtropical frontal region was evident as a salinity gradient typically from May-Dec, and was seldom evident as a temperature gradient. The largest seasonal changes in temperature and salinity, 9°C and 1.0 psu, were near the 32°N frontal region. The smallest seasonal change in temperature, 4°C, occurred at 22.75°N while the smallest seasonal change in salinity, 0.4 psu, occurred in the salinity maximum region. Interannual differences included deeper mixed layers and colder temperatures in winter 2009, a saltier salinity maximum region in summer 2009, fresher water north of

the 32°N frontal region in 2009, and fresher water south of the 25°N frontal region in 2007-2008.

4.4.2 Remnant Mixed Layer and Deeper Regions

As the mixed layer was primarily modulated with season, a composite year of average temperature and stratification with depth and density was constructed (Fig. 4.13). θ and N^2 were objectively mapped with a 40 km lengthscale and 120 day timescale onto a single year, and then averaged over 22.75-29°N, which is south of the 32°N frontal region. The average winter mixed layer was 75 m in depth and 24.5 kg m^{-3} in density, and included winter mixed layers of up to 160 m and 24.9 kg m^{-3}. A seasonal modulation of θ and N^2 was observed shallower than approximately 200 m and 25.1 kg m^{-3}, which was slightly deeper than the remnant mixed layer base. In the upper 200 m, temperature was warmest in August and coldest in March as in the mixed layer (Fig. 4.13a, c). Temperature along isopycnals was nearly constant and changed primarily as isopycnals restratified from or were entrained into the mixed layer (Fig. 4.13c). The seasonal modulation decreased on depth surfaces from 4.2°C at the surface to 0.8°C at 200 m (Fig. 4.13a), and on density surfaces from 0.3°C for lighter isopycnals to 0.1°C at 25.1 kg m^{-3} (Fig. 4.13c). For stratification, the largest seasonal modulation occurred just below the mixed layer base (Fig. 4.13b, d). The weak stratification of the mixed layer was left behind during restratification in Mar-May. Stratification then increased from May-Aug on both depth and density surfaces as the mixed layer heated causing additional isopycnals to be packed into the remnant

mixed layer and as vertical mixing eroded the minimum. The layer of high stratification below near 150 m and 24.8 kg m^{-3} from Dec-Apr was the winter transition layer (Johnston and Rudnick 2009). This high stratification was also left behind during restratification and weakened with time because of vertical mixing with surrounding water.

Seasonal modulations in smaller-scale thermohaline fluctuations were analyzed from a composite year of isopycnal salinity variance. Salinity variance over 22.75-29°N was calculated for each section and objectively mapped with a 120 day timescale (Fig. 4.14). To focus on shorter lengthscales, variance was calculated from S_{iso} perturbations where S_{iso} mapped with a 40 km lengthscale had been removed. The highest isopycnal salinity variance occurred in Mar-May near 24.7 kg m^{-3} and in Aug-Nov just below the mixed layer base. Shallower than 24.5 kg m^{-3}, low variance was left behind in May-June during restratification. Variance then increased with time because these isopycnals were not isolated from the mixed layer and were influenced by the emergence of the 25°N front. The elevated variance in Mar-May near 24.7 kg m^{-3} was consistent with large thermohaline fluctuations inherited from the mixed layer during restratification. Variance then decayed with time because of isopycnal mixing and reached a minimum in January. The low variance layer near 25.3 kg m^{-3} did not have a significant seasonal modulation, while the higher variance layer near 25.8 kg m^{-3} was largest in Feb-Mar and smallest in Oct-Nov. It is possible that the seasonal modulation at 25.8 kg m^{-3} reflects seasonal variability at the subduction region advected to our section.

S_{iso} spectra were calculated for the region of highest variance near 24.7 kg m^{-3} to determine what horizontal scales were seasonally modulated (Fig. 4.15). To calculate spectra, S_{iso} for each section was linearly interpolated to a 1 km uniform grid, a trend was removed, the resulting Fourier coefficients were averaged in adjacent wavenumber bands with more degrees of freedom at higher wavenumbers, and truncated at a 15 km wavelength. Spectra were averaged vertically over 24.6-24.8 kg m^{-3} near the bottom of the remnant mixed layer and over three sections in Apr-May when variance was largest and three sections in Nov-Dec when variance was smaller (Fig. 14-15). From Apr-May to Nov-Dec, variance decreased at all wavelengths from 15-280 km, and was significant at the 90% confidence level over 15-45 km wavelengths (Fig. 4.15; Table 4.2). Variance decreased by a factor of 4.5 over 15-23 km wavelengths and by a factor of 3.5 over 28-45 km wavelengths (Table 4.2).

Effective isopycnal diffusivity was estimated from the observed decrease in spice variance. Assuming simple diffusion of S_{iso}, $\dfrac{dS_{iso}}{dt} = \kappa_h \dfrac{d^2 S_{iso}}{dx^2}$, spectra of S_{iso} obey:

$$S_{iso}\left(k^*, t + \Delta t\right) = S_{iso}\left(k^*, t\right)\exp\left[-2k^* \kappa_h \Delta t\right] \qquad (4.1)$$

where k^* is wavelength and κ_h is a constant horizontal diffusivity (Cole et al. 2010). κ_h solved for in a least squares sense for the Apr-May to Nov-Dec decrease near 24.7 kg m^{-3} (Fig. 4.14-4.15), which corresponds to an average Δt of 215 days, was 0.4 m^2 s^{-1} over 15-23 km wavelengths and 0.9 m^2 s^{-1} 28-45 km wavelengths (Table 4.2). Wavelengths greater than 45 km were not considered because changes in variance

were not significant. κ_h previously estimated for the remnant mixed layer using this method was slightly larger at 1.4 m^2 s^{-1} over 30-46 km wavelengths (Cole et al. 2010). κ_h previously estimated from tracer release experiment was similar at approximately 0.3-6 m^2 s^{-1} over 1-30 km scales (Sundermeyer and Ledwell 2001; Ledwell et al. 1998). Unlike injected tracers, thermohaline fluctuations had sources and sinks throughout the time period considered. Our estimate of effective isopycnal diffusivity is a minimum value representing variance lost to smaller scales through mixing and variance gained from stirring at larger scales.

Using our estimated isopycnal diffusivity, the relative age of the spice variance layers considered in Sect. 4.3.2.1 was estimated. The time required for the large spice fluctuations at 25.8 kg m^{-3} to evolve into the smaller spice fluctuations at 25.3 kg m^{-3} was calculated assuming the difference in variance resulted only from age differences (Fig. 4.6c-d). To estimate this relative age, Δt, using 4.1, diffusivity, wavelength, and initial and final salinity variance had to be specified. Salinity variance averaged over the year from Fig. 4.14 was $10^{-3.7}$ psu^2 at 25.8 kg m^{-3} and $10^{-4.1}$ psu^2 at 25.3 kg m^{-3}, and consisted of salinity perturbations with 10-80 km wavelengths. The 0.9 m^2 s^{-1} diffusivity estimated for the remnant mixed layer with 30-40 km wavelengths was most appropriate to use. With these parameters, the high variance layer at 25.8 kg m^{-3} would have evolved into the low variance layer at 25.3 kg m^{-3} after 5-8 months. Absolute age estimated from tracer studies in the North Pacific was up to 12 years for 26.0 kg m^{-3} (Warner et al. 1996; Fine et al. 2001), so it is plausible that the low variance layer near 25.3 kg m^{-3} was less than a year older than water near 25.8 kg m^{-3}.

4.5 Summary and Conclusions

The sustained observations over 2.5 years and 5-1300 km scales show the spatial and temporal modulation of thermohaline structure. Thermohaline structure was set at the surface, left behind along isopycnals during restratification, weakened because of isopycnal mixing in the remnant mixed layer, and then advected throughout the ocean forming layers of spice variance. Temporal modulations were primarily seasonal and primarily above 200 m depth, including a factor of 3.5-4.5 decrease in submesoscale spice variance from spring to fall near the base of the remnant mixed layer. Spatial modulations included a factor of 3 increase in variance near the subtropical frontal regions in the remnant mixed layer, vertically stacked layers of variance that were up to four orders of magnitude smaller at 1000 m depth than at the surface, and horizontal modulations along some isopycnals where variance was up to three orders of magnitude larger near the southern end of the section.

With 2.5 years of observations, seasonal and some interannual modulations were investigated. Seasonal and interannual modulations have been studied in SST from satellites (eg. Kazmin and Rienecker 1996), and in θ and S below the surface from floats (eg. Wong and Johnson 2003; Ohno et al. 2009), long-term stations such as ALOHA (eg. Bingham and Lukas 1996), and climatologies (eg. Kara et al. 2000). Gliders are advantageous because they can remain in the same area and provide a large number of profiles over a short time period. In the mixed layer, temperature and salinity were seasonally modulated by 4-9°C and 0.4-1.0 psu with smaller interannual

differences. The 25°N frontal region was only evident from May-Dec as a salinity gradient, and the 32°N frontal region shifted north in summer with smaller gradients in winter. In the remnant mixed layer, average temperature along isopycnals was nearly constant and temperature changes resulted from isopycnals restratified from and entrained into the mixed layer. Weak stratification was inherited from the mixed layer during restratification and slowly increased with time. Spice variance left behind during restratification at the bottom of the remnant mixed layer decayed with time by a factor of 3.5-4.5 from spring to fall because of isopycnal mixing. Estimated effective diffusivities were 0.4 $m^2\,s^{-1}$ over 15-23 km wavelengths and 0.9 $m^2\,s^{-1}$ over 28-45 km wavelengths. Fluctuations near the mixed layer base increased with time because they were not isolated from the mixed layer. Deeper in the thermocline, thermohaline structure varied in time because of eddies such as the one in Fig. 4.8, but such eddies were not preferentially observed in any season or year. Near 25.8 $kg\,m^{-3}$, spice variance was seasonally modulated by a factor of 2-3, and may reflect a seasonal modulation at the subduction region advected to our section.

Thermohaline fluctuations had a complicated spatial geography and were influenced by tilting isopycnals, the initial fluctuation magnitude of the subduction region, water age, amount of stirring, and the gradient available to stir. On depth surfaces, tilting isopycnals projected the vertical salinity gradient into horizontal fluctuations so that salinity variance resembled the vertical salinity gradient. On density surfaces, three stacked layers of spice variance were observed below the remnant mixed layer that spanned about 250 m in depth and were stirred by the same

velocity field. Variance in the middle layer was about 2.5 times smaller than in the layer below, and coincided with an oxygen minimum and potential vorticity maximum. The low variance layer had a different history that possibly included 1) smaller fluctuations initially subducted, 2) a slower rate of subduction and advection or a longer path along which water was advected to our section that caused this layer to be older than water below, and 3) vertical mixing with the uncorrelated fluctuations in the surrounding higher variance layers. While tracers frequently show vertical layering of water masses, such thin layers close to the surface have not been previously studied. Near and below the NPIW salinity minimum, spice variance was three orders of magnitude larger near the southern end of the section because of 1) an enhanced isopycnal gradient available to stir caused when different water masses met, and 2) a larger amount of stirring. A larger amount of stirring was observed at all depths, but only appeared to affect variance below 26.2 kg m^{-3}, presumably because other processes near the surface had a larger effect.

The spatial and temporal modulation of thermohaline structure should be investigated further. Our observations were just long enough in time to investigate seasonal modulations or the persistence of the spatial modulation. Longer sections, or observations in different locations, will extend our picture of the spatial modulation of thermohaline structure and allow the origin, formation process, and termination of the spice variance layers near the surface to be determined. The transformation of thermohaline structure in the remnant mixed layer before permanent subduction should be investigated and included in numerical models.

Acknowledgements

Table 4.1 Summary of observations[a]

Deploymnent Dates	North Lat.[b] (°)	Δx[c] (km)	Δt[c] (h)	Num. Profiles
3 Jul 07 – 8 Sep 07	30.0	5.5±1.0	5.6±0.1	290
20 Nov 07 – 13 Mar 08	34.5	5.3±0.9	5.6±0.1	492
5 Apr 08 – 7 Jul 08	31.5	5.3±1.2	6.2±0.2	348
13 Apr 08 – 3 Jul 08	30.0	5.5±1.2	6.6±0.1	291
4 Aug 08 – 16 Nov 08	34.5	6.0±1.0	5.7±0.1	440
9 Dec 08 – 30 Mar 09	34.5	5.6±0.9	5.8±0.1	466
14 Apr 09 – 9 Aug 09	34.4	5.2±1.1	5.6±0.1	507
27 Aug 09 – 16 Dec 09	33.1	5.1±1.0	5.9±0.1	454

[a] Only 1000 m profiles are included in the statistics. There were 40 profiles to shallower depths.
[b] All sections are between 22.75°N and the north latitude specified.
[c] Δx and Δt are the mean ± standard deviation of the distance and time between all consecutive profiles in the deployment.

Table 4.2 Statistics of S_{iso} spectra over 22.75-29°N in the remnant mixed layer

Time Period[a]	Variance $(psu^2 \times 10^4)$		Variance Confidence Interval[b]		κ_h[c] $(m^2\ s^{-1})$	
	15-23 km	28-45 km	15-23 km	28-45 km	28-45 km	28-45 km
Apr-May	5.9	13.1	5.1-6.9	10.7-16.6	0.4	0.9
Nov-Dec	1.3	3.7	1.1-1.6	2.9-4.9		

[a] time periods correspond to dates listed in Fig. 4.15.
[b] 90% confidence interval.
[c] Effective horizontal diffusivity from Apr-May to Nov-Dec.
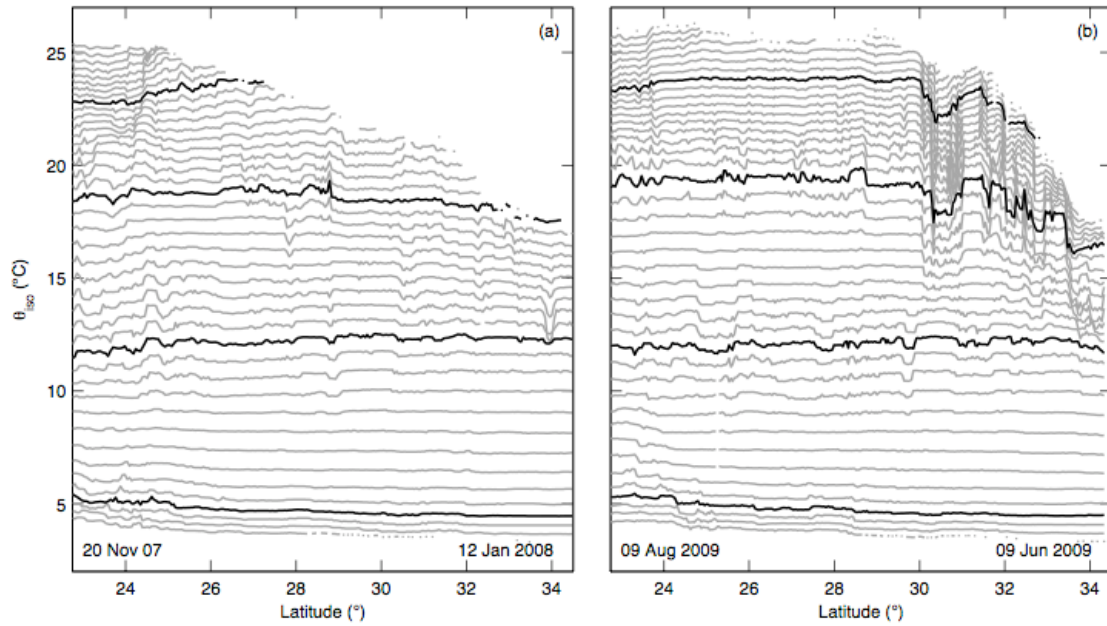
Figure 4.1 Temperature along isopycnals at 158°W in a) winter 2007-2008 and b) summer 2009. The 24.0, 25.0, 26.0 and 27.0 kg m^{-3} isopycnals are in black. Observations were made with an autonomous glider and start and end times for the section are in the lower corners. Observations cover the 0-1000 m depth range.
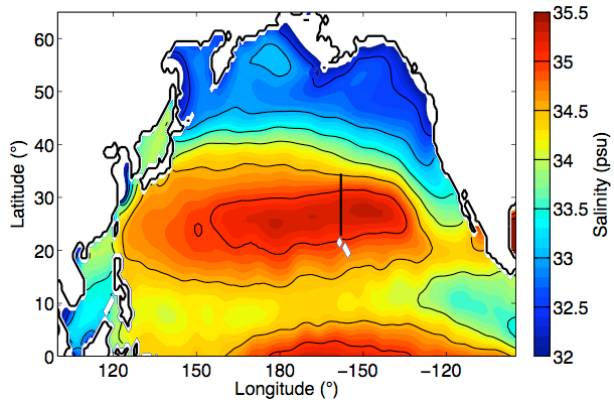
Figure 4.2 Mean surface salinity from World Ocean Atlas 2005 (Antonov et al. 2006). The glider track, 22.75-34.5°N, 158°W, is shown in black.
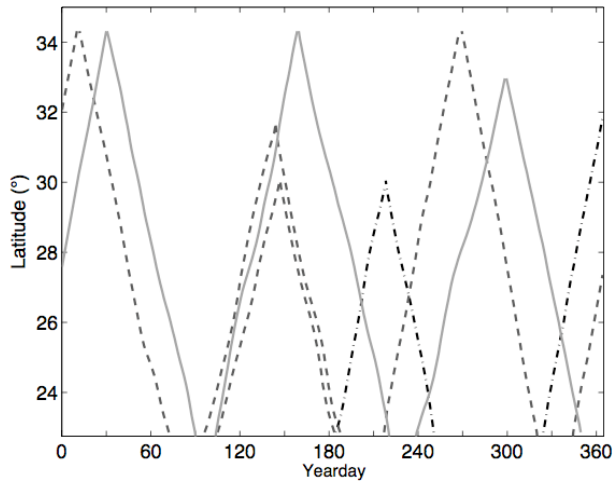
Figure 4.3 Phase sampling diagram. The different years are: 2007 (black dashed-dotted), 2008 (dark gray dashed), and 2009 (light gray solid). Statistics calculated over all glider sections are representative of statistics over all seasons.
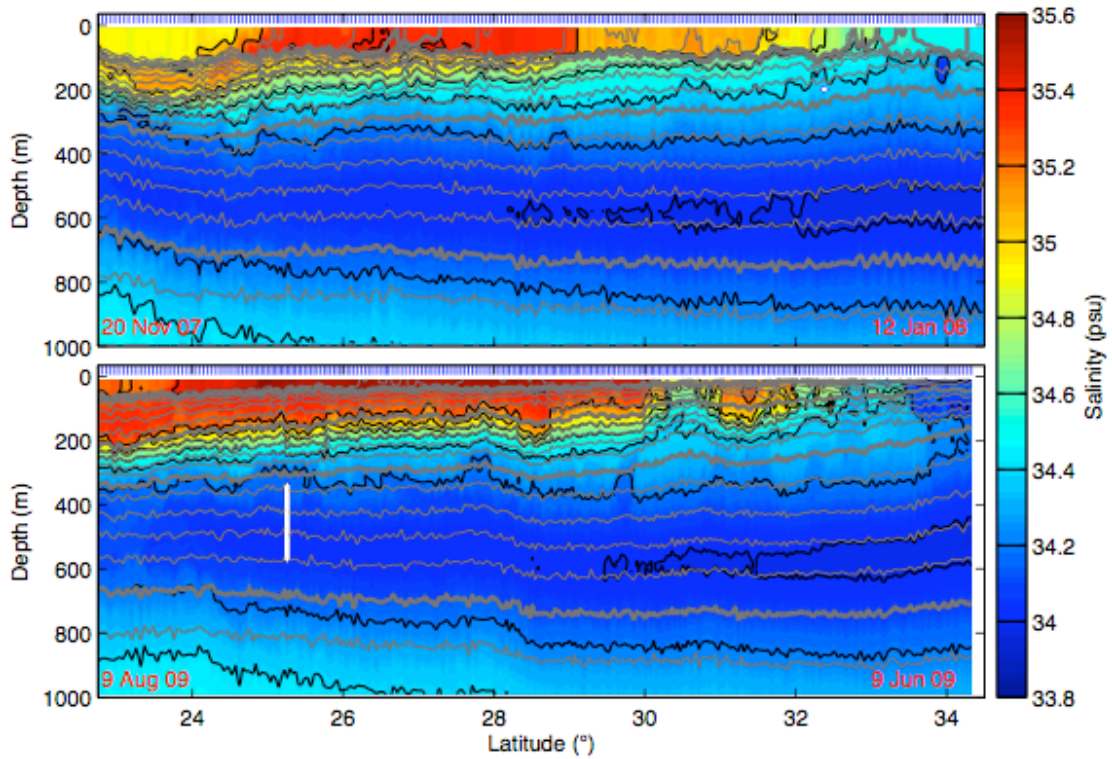
Figure 4.4 Example sections of salinity (color) with density contours (gray). The 24.0, 25.0, 26.0, and 27.0 kg m^{-3} isopycnals are emphasized. Tick marks (blue) show the location of each profile in the section. Sections are the same as in Fig. 4.1 with start and end dates in the lower corners.
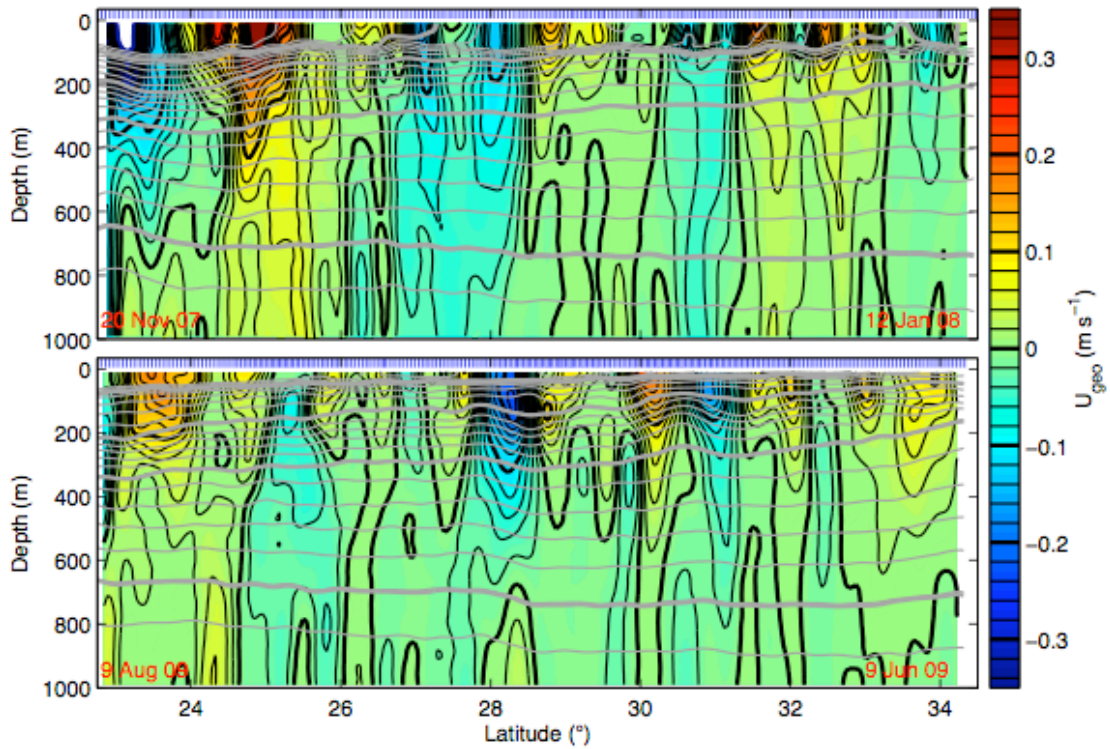
Figure 4.5 Example sections of geostrophic velocity objectively mapped with a 40 km lengthscale from density gradients and vertically averaged velocity. Positive velocity is eastward. Density contours (gray) as in Fig. 4.4 and mapped with a 40 km lengthscale. Tick marks as in Fig. 4.4. Sections are the same as in Fig. 4.1 with start and end dates in the lower corners.
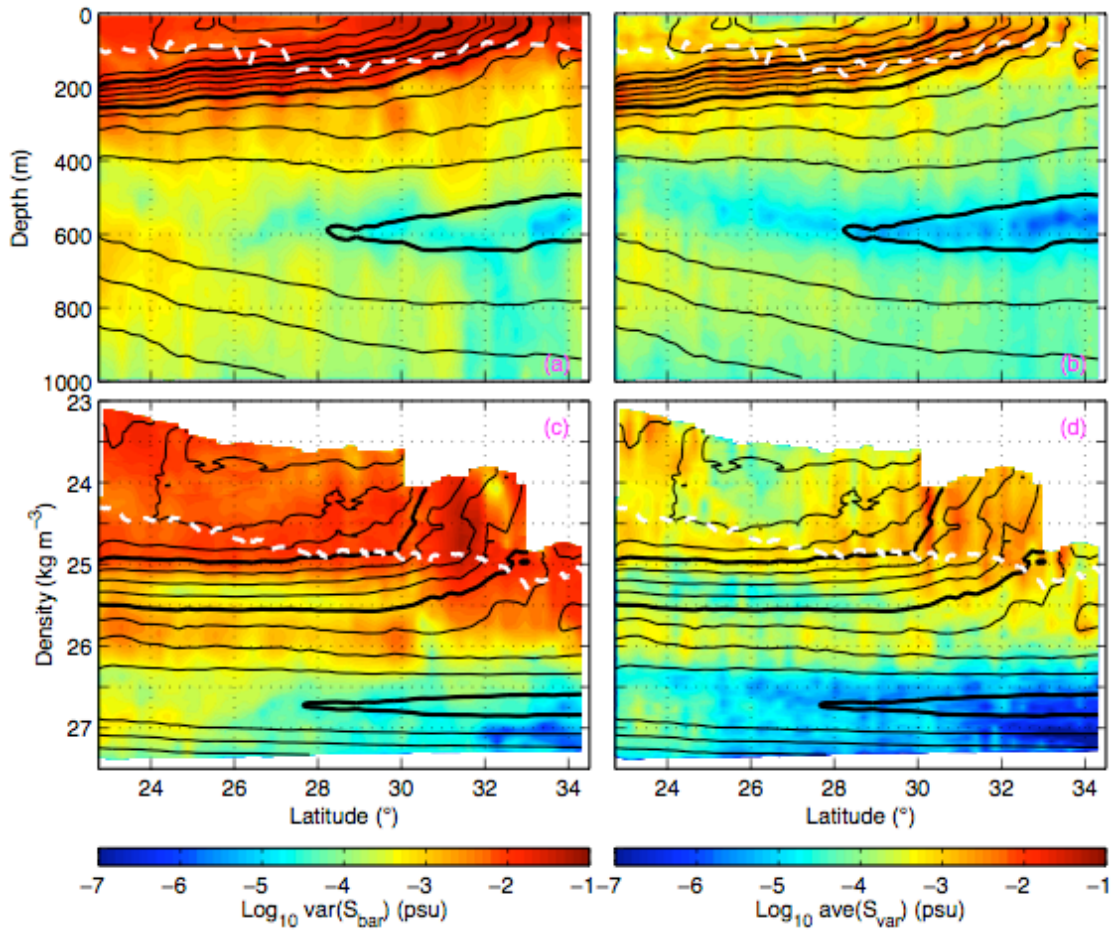
Figure 4.6 Variance of salinity on (a-b) depth surfaces and (c-d) density surfaces at (a, c) scales greater than 25 km and one day and (b, d) scales less than 25 km and one day. Contours (black) are mean salinity. Dashed white line is the deepest observed mixed layer base.
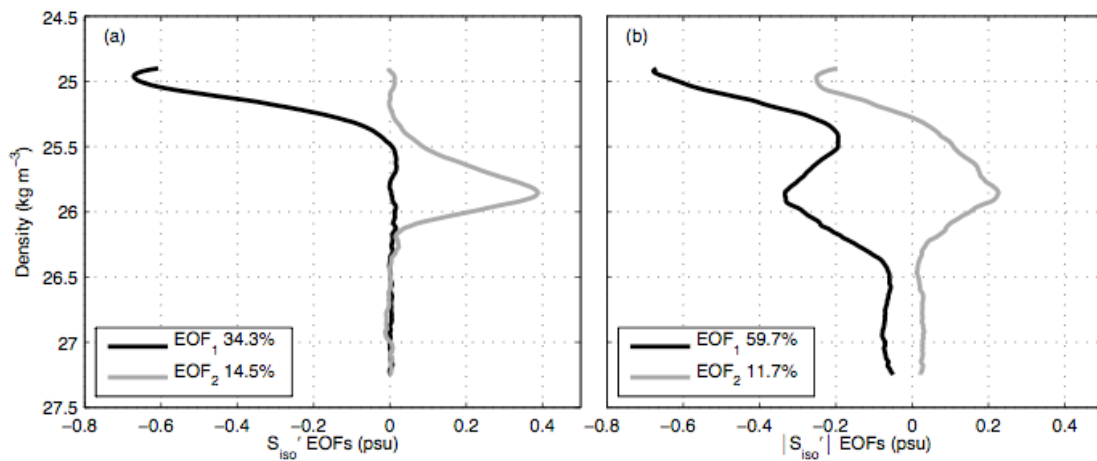
Figure 4.7 The first two EOFs of a) S_{iso} perturbations and b) the absolute value of S_{iso} perturbations over 22.75-30°N. Perturbations are calculated by subtracting S_{iso} objectively mapped with a 25 km lengthscale and are considered below the base of the winter mixed layer. The percentage of variance explained by each EOF is in the legend.
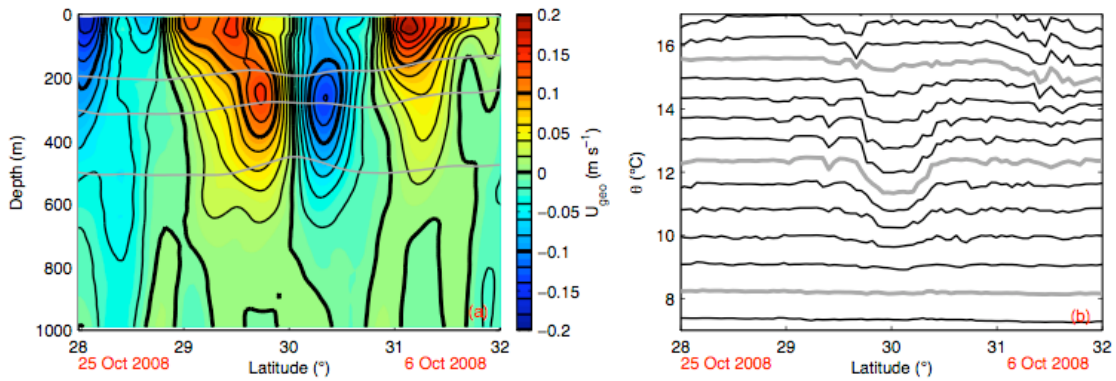
Figure 4.8 a) Geostrophic velocity and b) temperature along isopycnals in October 2008 showing an eddy at 30°N. Positive velocity is eastward. Gray contours are a) isopycnal depth objectively mapped with a 40 km lengthscale and b) isopycnal temperature for the 25.5, 26.0, and 26.5 kg m^{-3} isopycnals. In (b), the depth range shown is approximately 150-500 m. Start and end dates are in the lower corners.
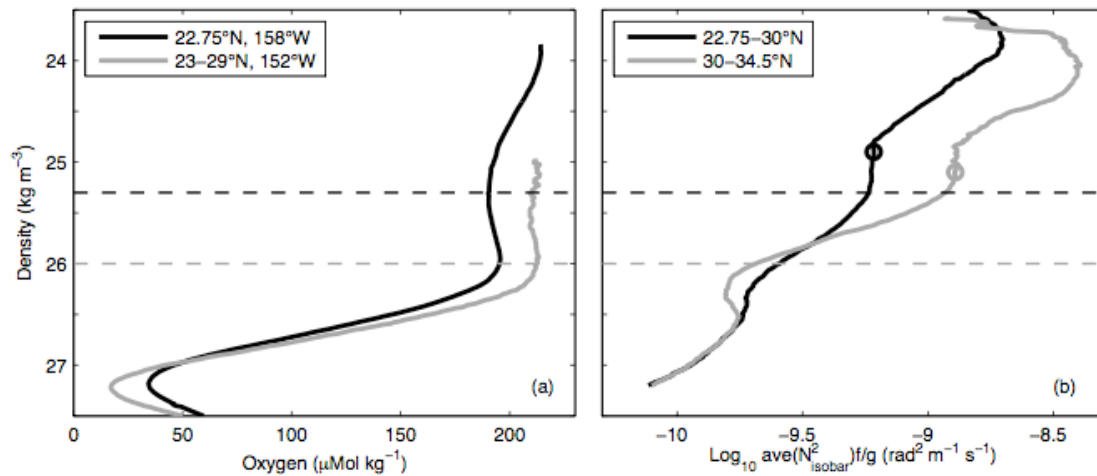
Figure 4.9 Observations of tracers. a) Mean oxygen from station ALOHA at 22.75°N, 158°W over 2007-2009 (black) and from a hydrographic section along 152°W in March 2006 over 23-29°N (gray). b) Mean vertical potential vorticity over 22.75-30°N and 30-34.5°N from glider observations. Circles correspond to the deepest observed winter mixed layer base in each region. The 25.3 kg m^{-3} isopycnal (dashed black) is a local oxygen minima and potential vorticity maxima. The 26.0 kg m^{-3} isopycnal (dashed gray) is a local oxygen maximum and just above a potential vorticity minimum.
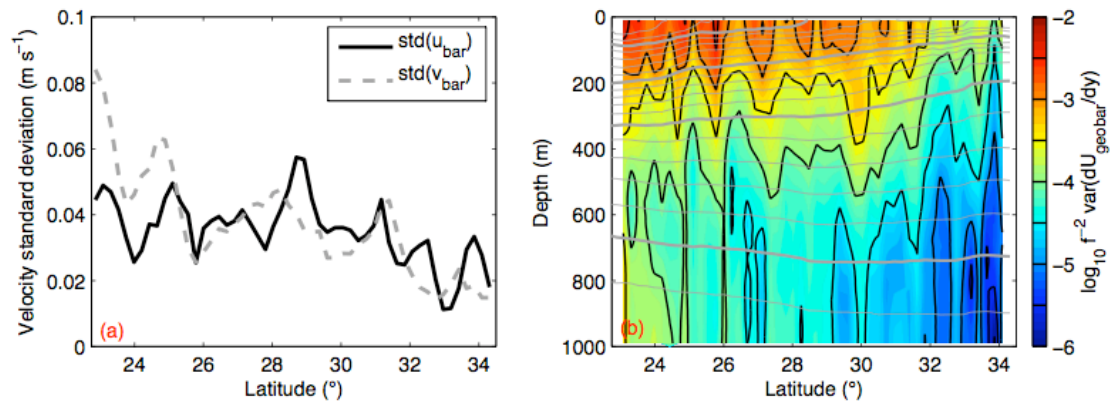
Figure 4.10 Velocity and vorticity statistics. a) Standard deviation over all glider sections of vertically averaged eastward (solid) and northward (dashed) velocity, and b) variance over all gliders sections of the 25 km gradient of mean geostrophic velocity. Contours (gray) are mean density with 24.0, 25.0, 26.0 and 27.0 kg m^{-3} emphasized. Only 1000 m profiles are included in the statistics.
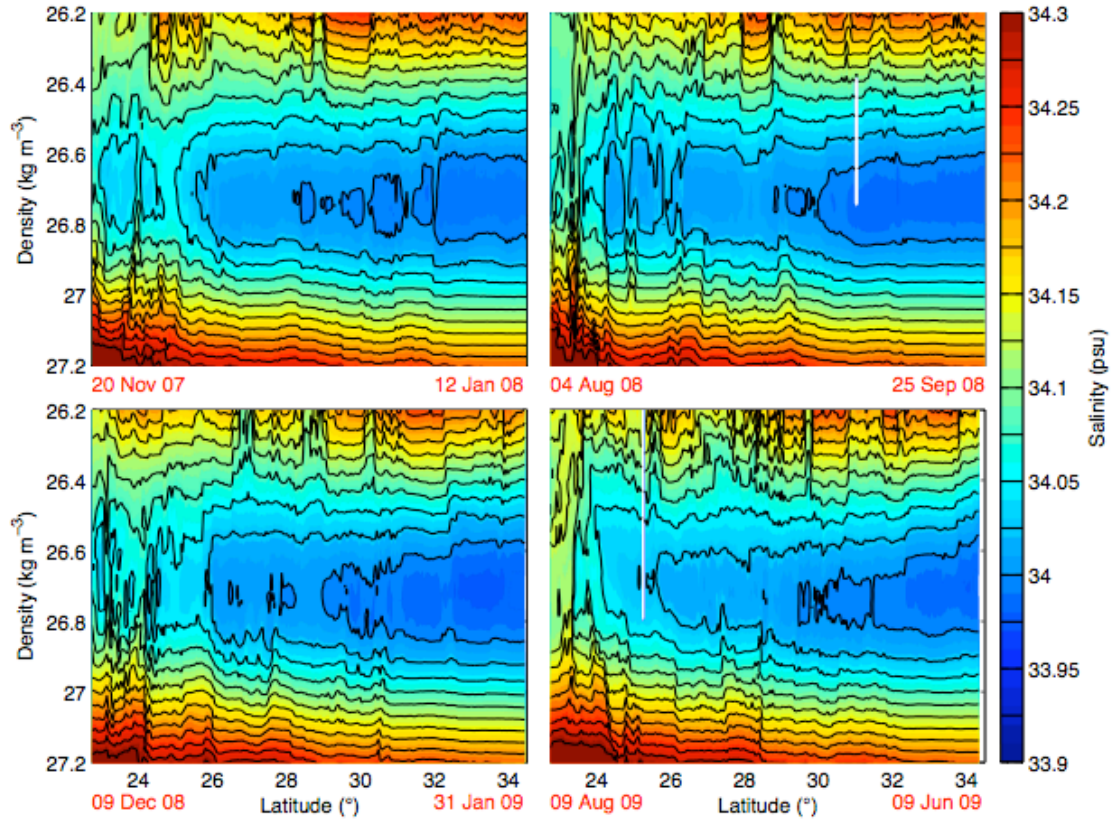
Figure 4.11 Sections of salinity along isopycnals showing the salinity minimum and increased variance towards the south. Sections are winter and summer 2008 (top) and winter and summer 2009 (bottom) including those of Fig. 4.1 (top left and bottom right) with start and end dates in the lower corners.
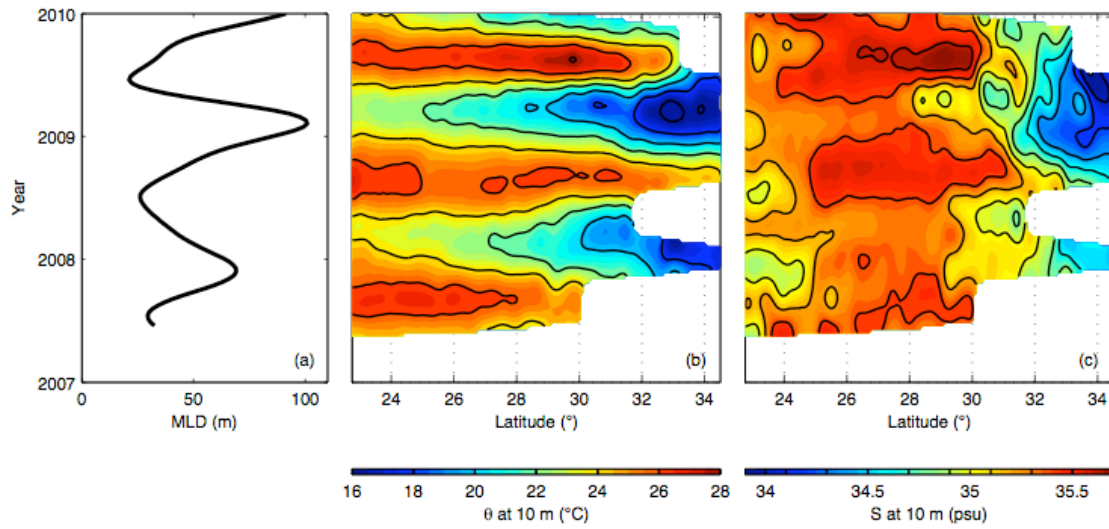
Figure 4.12 Mixed layer temporal variability. a) Mixed layer depth objectively mapped with a 40 km lengthscale and 120 day timescale and then averaged over 22.75-29°N. b) Temperature and c) salinity at 10 m depth objectively mapped with a 40 km lengthscale and 120 day timescale.
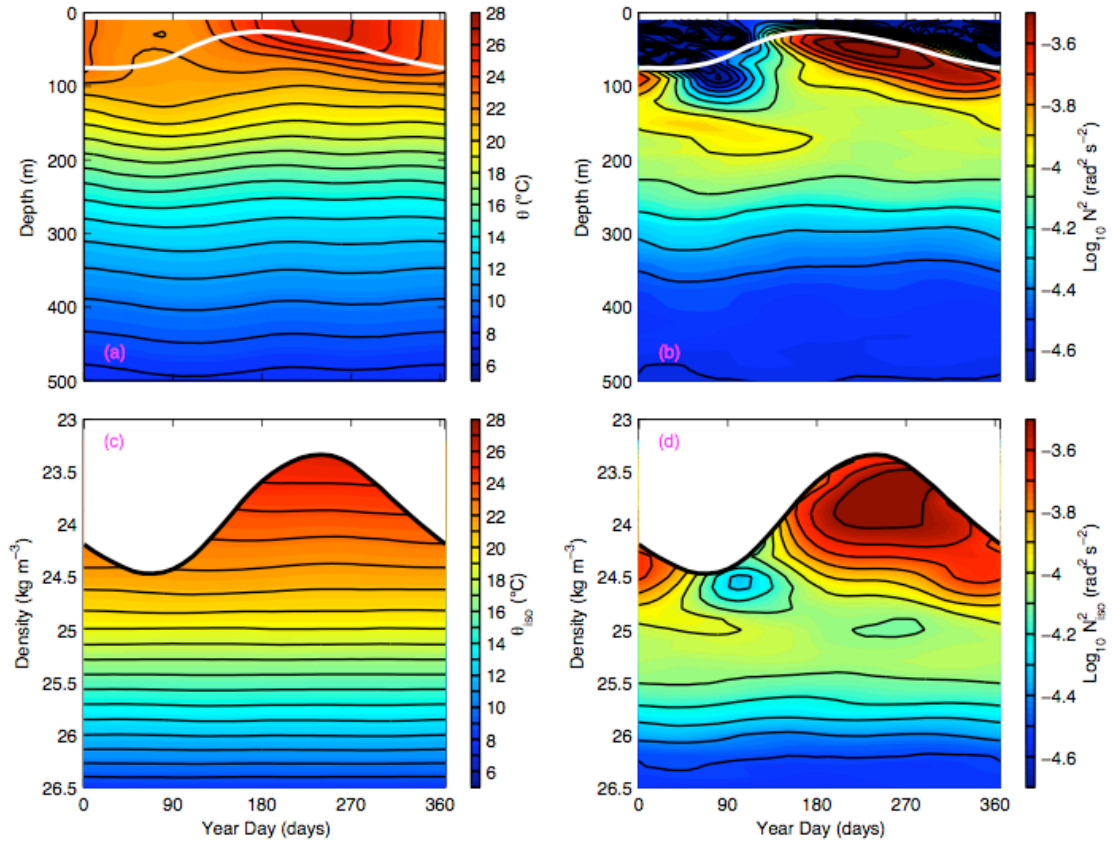
Figure 4.13 Seasonal variability with depth and density. Mean over 22.75-29°N of (a,c) temperature and (b,d) stratification on (a-b) depth surfaces and (c-d) density surfaces after objective mapping onto a single year with a 40 km lengthscale and 120 day timescale. Similarly mapped mixed layer depth (white; a-b) and mixed layer density (black; c-d) are shown.

Figure 4.14 Seasonal variability of S_{iso} fluctuations. Variance over 22.75-29°N is calculated for each section, and then objectively mapped onto a single year with a 120 day timescale. Variance is calculated from fluctuations that have S_{iso} mapped with a 40 km lengthscale removed. Black line as in Fig. 4.13.

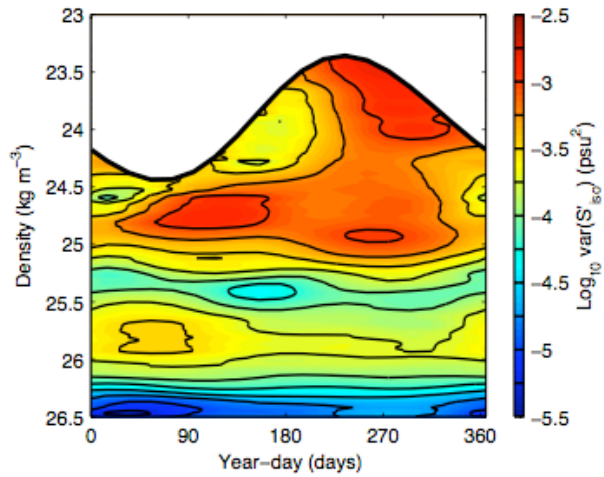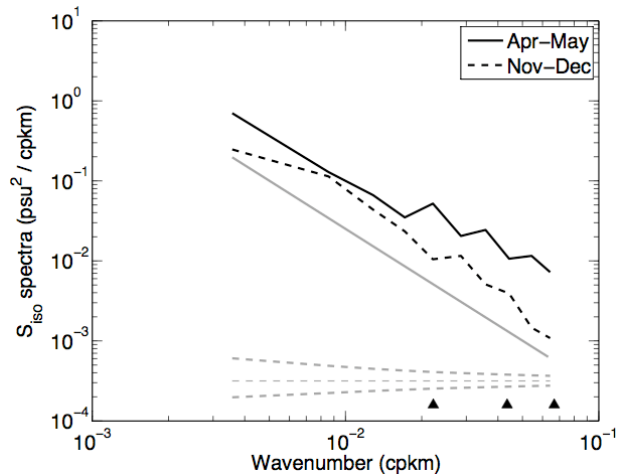**Figure 4.15** Spectra of S_{iso} over 22.75-29°N vertically averaged over 24.6-24.8 kg m^{-3} and the time periods indicated. Apr-May includes 5 Apr – 8 May 2008, 13 Apr – 20 May 2008, and 14 Apr – 15 May 2009 sections, and Nov-Dec includes 20 Oct – 16 Nov 2008, 9 Dec 2008 – 6 Jan 2009, and 12 Nov - 16 Dec 2009 sections. The gray line has a slope of k^{-2}. Error bars (dashed) show the 90% confidence interval. The number of degrees of freedom at each wavelength for each section is taken to be twice the record length, 700 km, divided by the wavelength. Triangles correspond to 15, 23, and 45 km wavelengths.

References

Alford, M. H., and Z. Zhao, 2007: "Global patterns of low mode internal wave propagation. Part II: Group Velocity." *J. Phys. Oceanogr.,* 37, 1849-1858.

Alfultis, M. A., and P. Cornillon, 2001: "A characterization of the North Atlantic STMW layer climatology using World Ocean Atlas 1994 data." *J. Atmos. Oceanic Technol.,* 18*,* 2021-2037.

Althaus, A. M., E. Kunze, and T. B. Sanford, 2003: "Internal tide radiation from Mendocino Escarpment." *J. Phys. Oceanogr., 33,* 1510-1527.

Antonov, J. I., R. A. Locarnini, T. P. Boyer, A. V. Mishonov, and H. E. Garcia, 2006: "World Ocean Atlas 2005, vol. 2, Salinity." NOAA Atlas NESDIS 62, edited by S. Levitus, U. S. Government Printing Office, Washington, D. C., 182 pp.

Armi, L., and H. Stommel, 1983: "Four views of a portion of the North Atlantic subtropical gyre." *J. Phys. Oceanog*r., *13*, 828-857.

Aucan, J., M. A. Merrifield, D. S. Luther, and P. Flament, 2006: "Tidal mixing events on the deep flanks of Kaena Ridge, Hawaii." *J. Phys. Oceanogr., 36,* 1202-1219.

Baines, P. G., 1982: "On internal tide generation models." *Deep-Sea Res., 29,* 307-338.

Bauer, E., and G. Siedler, 1988: "The relative contributions of advection and isopycnal and diapycnal mixing below the subtropical salinity maximum." *Deep Sea Res., 35,* 811-837.

Bernstein, R. L, and W. B. White, 1974: "Time and length scales of baroclinic eddies in the central North Pacific Ocean." *J. Phys. Oceanogr., 4,* 613-624.

Bingham, F. M., and R. Lukas, 1996: "Seasonal cycles of temperature, salinity, and dissolved oxygen observed in the Hawaii Ocean Time-series." *Deep Sea Res. II, 43,* 199-213.

Bingham, F. M., T. Suga, and K. Hanawa, 2002: "Origin of waters observed along 137°E." *J. Geophys. Res.*, *107,* 3073.

Boccaletti, G., R. Ferrari, and B. Fox-Kemper, 2007: "Mixed layer instabilities and restratification." *J. Phys. Oceanogr., 37,* 2228-2250.

Bostock, H. C., B. N. Opdyke, and M. J. M. Williams, 2010: "Characterizing the intermediate depth waters of the Pacific Ocean using $\delta^{13}C$ and other geochemical tracers." *Deep Sea Res., 57*, 847-859.

Bracco, A., S. Clayton, and C. Pasquero, 2009: "Horizontal advection, diffusion, and plankton spectra at the sea surface." *J. Geophys. Res., 114,* C02001.

Brainerd, K. E., and M. C. Gregg, 1993: "Diurnal restratification and turbulence in the oceanic surface mixed layer 1. Observations." *J. Geophys. Res., 98,* 22645-22656.

Bullister, J. L., D. P. Wisegarver, and R. E. Sonnerup, 2006: "Sulfer hexafluoride as a transient tracer in the North Pacific Ocean." *Geophys. Res. Lett., 33,* L18603.

Cairns, J. L., and G. O. Williams, 1976: "Internal wave observations from a midwater float 2." *J. Geophys. Res., 81,* 1943-1950.

Capet, X., J. C. McWilliams, M. J. Molemaker, and A. F. Shchepetkin, 2008: "Mesoscale to submesoscale transition in the California Current System. Part I: Flow structure, eddy flux and observational tests." *J. Phys. Oceanogr., 38,* 29-43.

Castelao, R., S. Glenn, and O. Schofield, 2010: "Temperature, salinity, and density variability in the central Mid Atlantic Bight." *J. Geophys. Res., in press.*

Chen, S., and B. Qiu, 2010: "Mesoscale eddies northeast of the Hawaiian archipelago from satellite altimeter observations." *J. Geophys. Res., 115,* C03016.

Cole, S. T., D. L. Rudnick, and J. A. Colosi, 2010: "Seasonal evolution of upper ocean horizontal structure and the remnant mixed layer." *J. Geophys. Res., 115,* C04012.

Dale, A. C., D. S. Ullman, J. A. Barth, and D. Hebert, 2003: "The front on the northern flank of George's Bank in Spring: 1. Tidal and subtidal variability." *J. Geophys. Res., 108,* 8009.

Davies, A. M., and J. X. Xing, 2003: "On the interaction between internal tides and wind-induced near-inertial currents at the shelf edge." *J. Geophys. Res., 108,* 3099.

Davis, R. E., M. D. Ohman, D. L. Rudnick, J. T. Sherman, and B. A. Hodges, 2008: "Glider surveillance of physics and biology in the southern California Current System." *Limnol. Oceanogr., 53,* 2151-2168.

Dimotakis, P. E., 2005: "Turbulent mixing." *Annu. Rev. Fluid Mech., 37,* 329-356.

Dinniman, M. S., and M. M. Rienecker, 1999: "Frontogenesis in the North Pacific oceanic frontal zones – A numerical simulation." *J. Phys. Oceanogr., 29,* 537-559.

Ducet, N., P. Y. Le Traon, and G. Reverdin, 2000: "Global high-resolution mapping of ocean circulation from TOPEX/Posseidon and ERS-1 and -2." *J. Geophys. Res., 105,* 19477-19498.

Dugan, J. P., W. D. Morris, and B. S. Okawa, 1986: "Horizontal wave number distribution of potential energy in the ocean." *J. Geophys. Res., 91,* 12993-13000.

Dushaw, B. D., B. D. Cornuelle, P. F. Worcester, B. M. Howe, and D. S. Luther, 1995: "Barotropic and baroclinic tides in the central North Pacific-Ocean determined from long-range reciprocal acoustic transmissions." *J. Phys. Oceanogr., 25,* 631-647.

Dzieciuch, M., W. Munk, and D. L. Rudnick, 2004: "Propagation of sound through a spicy ocean, the SOFAR overture." *J. Acoust. Soc. Am., 116,* 1447-1462.

Egbert, G. D., and R. D. Ray, 2001: "Estimates of M_2 tidal energy dissipation from TOPEX/Poseidon altimeter data." *J. Geophys. Res., 106,* 22475-22502.

Ferrari, R., and W. R. Young, 1997: "On the development of thermohaline correlations as a result of nonlinear diffusive parameterizations." *J. Mar. Res., 59,* 1069-1101.

Ferrari, R., and D. L. Rudnick, 2000: "Thermohaline variability in the upper ocean." *J. Geophys. Res., 105,* 16857-16883.

Ferrari, R., and F. Paparella, 2003: "Compensation and alignment of thermohaline gradients in the ocean mixed layer." *J. Phys. Oceanogr., 35,* 2214-2223.

Fine, R. A., K. A. Maillet, K. F. Sullivan, and D. Willey, 2001: "Circulation and ventilation flux of the Pacific Ocean." *J. Geophys. Res., 106,* 22159-22178.

Fofonoff, N. P., 1969: "Spectral characteristics of internal waves in the ocean." *Deep-Sea Res., 16 (Suppl.),* 58-71.

Garrett, C., and W. Munk, 1979: "Internal waves in the ocean." *Annu. Rev. Fluid Mech., 11,* 339-369.

Garrett, C., 2006: "Turbulent dispersion in the ocean." *Prog. Oceanog., 70,* 113-125.

Garrett, C., and E. Kunze, 2007: "Internal tide generation in the deep ocean." *Annu. Rev. Fluid Mech., 39,* 57-97.

Gerkema, T., C. Staquet, and P. Bouruet-Aubertot, 2006a: "Non-linear effects in internal-tide beams, and mixing." *Ocean Modelling, 12,* 302-318.

Gerkema, T., C. Staquet, and P. Bouruet-Aubertot, 2006b: "Decay of semi-diurnal

internal-tide beams due to subharmonic resonance." *Geophys. Res. Lett., 33,* L08604.

Gill, A. E., 1982: *Atmosphere-ocean dynamics.* Vol. 30. Academic Press, 662 pp.

Glenn, S., C. Jones, M Twardowski, L. Bowers, J. Kerfoot, J, Kohut, D. Webb, and O. Schofield, 2008: "Glider observations of sediment resuspension in a Middle Atlantic Bight fall transition storm." *Limnol. Oceanogr., 53,* 2180-2196.

Gregg, M. C., 1989: "Scaling turbulent dissipation in the thermocline." *J. Geophys. Res., 94,* 9686-9698.

Gregg, M. C., and Kunze, E., 1991: "Internal wave shear and strain in Santa Monica Basin." *J. Geophys. Res., 96,* 16709-16719.

Gregg, M. C., T. B. Sanford, and D. P. Winkel, 2003: "Reduced mixing from the breaking of internal waves in equatorial waters." *Nature, 422,* 513-515.

Hall, M. M., P. P. Niiler, and W. J. Schmitz, 1997: "Circulation in the eastern North Pacific: results from a current meter array along 152°W." *Deep Sea Res. I, 44,* 1127-1146.

Hautala, S. R. and D. H. Roemmich, 1998: "Subtropical mode water in the northeast Pacific Basin." *J. Geophys. Res., 103,* 13055-13066.

Hodges, B. A., and D. L. Rudnick, 2006: "Horizontal variability in chlorophyll fluorescence and potential temperature." *Deep Sea Res., 53,* 1460-1482.

Holloway, P. E., and M. A. Merrifield, 1999: "Internal tide generation by seamounts, ridges, and islands." *J. Geophys. Res., 104,* 25937-25951.

Hosegood, P., M. C. Gregg, and M. H. Alford, 2006: "Sub-mesoscale lateral density structure in the oceanic surface mixed layer." *Geophys. Res. Lett., 33,* doi:10.1029/2006GL026797.

James, C., M. Tomczak, I. Helmond, and L Pender, 2002: "Summer and winter surveys of the Subtropical Front of the southeastern Indian Ocean 1997-1998." *J. Mar. Sys., 37,* 129-149.

Jenkins, W. J., 1987: "3H and 3He in the beta triangle: Observation of gyre ventilation and oxygen utilization rates." *J. Phys. Oceanogr., 17,* 763-783.

Johnston, T. M. S., and D. L. Rudnick, 2009: "Observations of the transition layer." *J. Phys. Oceanogr., 39,* 780-797.

Joyce, T. M., J. R. Luyten, A. Kubryakov, F. B. Bahr, and J. S. Pallant, 1998: "Meso-to large-scale structure of subducting water in the subtropical gyre of the eastern North Atlantic ocean." *J. Phys. Oceanogr., 28,* 40-61.

Kara, A. B., P. A. Rochford, and H. E. Hulbert, 2000: "Mixed layer depth variability and barrier layer formation of the North Pacific Ocean." *J. Geophys. Res., 105,* 16783-16801.

Karl, D. M., and R. Lukas, 1996: "The Hawaii Ocean Time-series (HOT) program: Background, rationale, and field implementation." *Deep Sea Res. II, 43,* 129-156.

Katz, E. J., 1975: "Tow spectra from MODE." *J. Geophys. Res.*, *80,* 1163-1167.

Kazmin, A. S., and M. M. Rienecker, 1996: "Variability and frontogenesis in the large-scale oceanic frontal zones." *J. Geophys. Res., 101,* 907-921.

Khatiwala, S., 2003: "Generation of internal tides in an ocean of finite depth: analytical and numerical calculations." *Deep-Sea Res., 50,* 3-21.

Kitade, Y., and M. Matsuyama, 2002: "Semidiurnal internal tide observed over Ohmuro-Dashi, the northern part of the Izu Ridge." *Deep-Sea Res., 49,* 1309-1320.

Klein, P., B. L. Hua, G. Lapeyre, X. Capet, S. LeGentil, and H. Sasaki, 2008: "Upper ocean turbulence from high-resolution 3D simulations." *J. Phys. Oceanogr., 38,* 1748-1763.

Klein, P., and G. Lapeyre, 2009: "The oceanic vertical pump induced by mesoscale and submesoscale turbulence." *Annu. Rev. Mar. Sci.*, 1, 351-375.

Klymak, J. M., J. N. Moum, J. D. Nash, E. Kunze, J. B. Girton, G. S. Carter, C. M. Lee, T. B. Sanford, and M. C. Gregg, 2006: "An estimate of tidal energy lost to turbulence at the Hawaiian Ridge." *J. Phys. Oceanogr., 36,* 1148-1164.

Kunze, E., L. K. Rosenfeld, G. S. Carter, and M. C. Gregg, 2002: "Internal waves in Monterey Submarine Canyon." *J. Phys. Oceanogr., 32,* 1890-1913.

Ladd, C., and L. Thompson, 2000: "Formation mechanisms for North Pacific central and eastern subtropical mode waters." *J. Phys. Oceanogr., 30,* 868-887.

Lam, F. P. A., L. R. M. Maas, and T. Gerkema, 2004: "Spatial structure of tidal and residual currents as observed over the shelf break in the Bay of Biscay." *Deep-Sea Res., 51,* 1075-1096.

Lamb, K. G., 2004: "Nonlinear interaction among internal wave beams generated by tidal flow over supercritical topography." *Geophys. Res. Lett., 31,* L09313.

Ledwell, J. R., A. J. Watson, and C. S. Law, 1998: "Mixing of a tracer in the pycnocline." *J. Geophys. Res., 103,* 21499-21529.

Lee, C. M., E. Kunze, T. B. Sanford, J. D. Nash, M. A. Merrifield, and P. E. Holloway, 2006: "Internal tides and turbulence along the 3000-m isobath of the Hawaiian Ridge." *J. Phys. Oceanogr., 36,* 1165-1183.

Legg, S. and M. H. Huijts, 2006: "Preliminary simulations of internal waves and mixing generated by finite amplitude tidal flow over isolated topography." *Deep-Sea Res., 53,* 140-156.

Lien, R. C., and P. Müller, 1992: "Consistency relations for gravity and vortical modes in the ocean." *Deep-Sea Res., 39,* 1595-1612.

Lien, R. C., and M. C. Gregg, 2001: "Observations of turbulence in a tidal beam and across a coastal ridge." *J. Geophys. Res., 106,* 4575-4591.

Lighthill, J., 1978: *Waves in Fluids*. Cambridge University Press, 504 pp.

Llewellyn-Smith, S. G., and W. R. Young, 2003: "Tidal conversion at a very steep ridge." *J. Fluid Mech., 495,* 175-191.

Loder, J. W., D. Brickman, and E. P. W. Horne, 1992: "Detailed structure of currents and hydrography on the northern side of Georges Bank." *J. Geophys. Res.*, *97,* 14331-14351.

Lozovatsky, I. D., E. G. Morozov, and H. J. S. Fernando, 2003: "Spatial decay of energy density of tidal internal waves." *J. Geophys. Res.*, *108,* 3201.

Lueck, R. G., and T. D. Mudge, 1997: "Topographically induced mixing around a shallow seamount." *Science, 276,* 1831-1833.

Macdonald, A. M., S. Mecking, P. E. Robbins, J. M. Toole, G. C. Johnson, L. Talley, M. Cook, and S. E. Wijffels, 2009: "The WOCE-era 3-D Pacific ocean circulation and heat budget." *Progress in Oceanogr., 82,* 281-325.

Mahadevan, A., and A. Tandon, 2006: "An analysis of mechanisms for submesoscale vertical motions at ocean fronts." *Ocean Mod., 14*, 241-256.

Martin, J. P., D. L. Rudnick, and R. Pinkel, 2006: "Spatially broad observations of internal waves in the upper ocean at the Hawaiian Ridge." *J. Phys. Oceanogr., 36,* 1085-1103.

Martin, J. P., D. L. Rudnick, 2007: "Inferences and Observations of Turbulent

Dissipation and Mixing in the Upper Ocean at the Hawaiian Ridge." *J. Phys. Oceanogr., 37,* 476-494.

McWilliams, J. C., 1985: "Submesoscale, coherent vorticies in the ocean." *Rev. Geophys., 22*, 165-182.

Merrifield, M. A., and P. E. Holloway, 2002: "Model estimates of M_2 internal tide energetics at the Hawaiian Ridge." *J. Geophys. Res., 107,* 3179.

Messias, M. J., et al., 2008: "The Greenland sea tracer experiment 1996-2002: "Horizontal mixing and transport of Greenland sea intermediate water." *Progress in Oceanogr., 78,* 85-105.

Montegut, C., G. Madec, A. S. Fischer, A. Lazar, and D. Iudicone, 2004: "Mixed layer depth over the global ocean: An examination of profile data and profile-based climatology." *J. Geophys. Res., 109,* C12003.

Mowbray, D. E. and B. S. H. Rarity, 1967: "A theoretical and experimental investigation of the phase configuration of internal waves of small amplitude in a density stratified fluid." *J. Fluid Mech., 28,* 1-16.

Müller, P., 1976: "Diffusion of momentum and mass by internal gravity-waves." *J. Fluid Mech., 77,* 789-823.

Munk W., 1981: "Internal waves and small-scale processes." *Evolution of Physical Oceanography,* B. A. Warren and C. Wunsch, Eds., The MIT Press, 264-291.

Munk W., C. Wunsch, 1998: "Abyssal recipies II: energetics of tidal and wind mixing." *Deep-Sea Res., 45,* 1977-2010.

Munroe, J. R., and K. G. Lamb, 2005: "Topographic amplitude dependence of internal wave generation by tidal forcing over idealized three-dimensional topography." *J. Geophys. Res., 110,* C02001.

Nash, J. D., E. Kunze, C. M. Lee, and T. B. Sanford, 2006: "Structure of the baroclinic tide generated at Kaena Ridge, Hawaii." *J. Phys. Oceanogr., 36,* 1123-1135.

Neelder, G. T., and R. A. Heath, 1975: "Diffusion coefficients calculated from the Mediterranean salinity anomaly in North Atlantic ocean." *J. Phys. Oceanogr., 5,* 173-182.

Nicholson, D., S. Emerson, and C. C. Eriksen, 2008: "Net community production in the deep euphotic zone of the subtropical North Pacific gyre from glider surveys." *Limnol. Oceanogr., 53,* 2226-2236.

Ohno, Y., N. Iwasaka, F. Kobashi, and Y. Sato, 2009: "Mixed layer depth climatology of the North Pacific based on Argo observations." *J. Oceanogr., 65,* 1-16.

Oka, E., S. Kouketsu, K. Toyama, K. Uehara, T. Kobayashi, S. Hosoda, and T. Suga (2010), Formation and subduction of Central Mode Water based on profiling float data 2003-2008, *J. Phys. Oceanogr., in press.*

Oka, E., L. D. Talley, and T. Suga, 2007: "Temporal variability of winter mixed layer in the mid to high latitude North Pacific." *J. Oceanogr., 63,* 293-307.

Okubo, A., 1971: "Oceanic diffusion diagrams." *Deep Sea Res., 18,* 789-802.

Paillet, J., and M. Arhan, 1996: "Shallow pycnoclines and mode water subduction in the eastern North Atlantic." *J. Phys. Oceanogr., 25,* 96-114.

Perry, M. J., B. S. Sackmann, C. C. Eriksen, and C. M. Lee, 2008: "Seaglider observations of blooms and subsurface chlorophyll maxima off the Washington coast." *Limnol. Oceanogr., 53,* 2169-2179.

Petrelis, F., S. Llewellyn-Smith, and W. R. Young, 2006: "Tidal conversion at a submarine ridge." *J. Phys. Oceanogr., 36,* 1053-1071.

Petruncio, E. T., L. K. Rosenfeld, and J. D. Paduan, 1998: "Observations of the internal tide in Monterey Canyon." *J. Phys. Oceanogr., 28,* 1873-1903.

Pingree, R. D., and A. L. New, 1989: "Downward propagation of internal tidal energy into the Bay of Biscay." *Deep-Sea Res., 36,* 735-758.

Pingree, R. D., and A. L. New, 1991: "Abyssal Penetration and Bottom Reflection of Internal Tidal Energy in the Bay of Biscay." *J. Phys. Oceanogr., 21,* 28-39.

Pollard, R., 1986: "Frontal surveys with a towed profiling conducitivity/ temperature / depth measurement package (SeaSoar)." *Nature, 323,* 433-435.

Prinsenberg, S., W. L. Wilmot, and M. Rattray, 1974: "Generation and Dissipation of Coastal Internal Tides." *Deep-Sea Res., 21,* 263-281.

Rainville, L., and R. Pinkel, 2006a: "Baroclinic energy flux at the Hawaiian Ridge: Observations from the R/P FLIP." *J. Phys. Oceanogr., 36,* 1104-1122.

Rainville, L., and R. Pinkel, 2006b: "Propagation of low-mode internal waves through the ocean." *J. Phys. Oceanogr., 36,* 1220-1236.

Ray, R. D., and G. T. Mitchum, 1996: "Surface manifestation of internal tides generated near Hawaii." *Geophys. Res. Lett., 23,* 2101-2104.

Reid, J. L., 1997: "On the total geostrophic circulation of the Pacific Ocean: flow patterns, tracers, and transports." *Progress in Oceanogr., 39,* 263-352.

Rintoul, S. R., and T. W. Trull, 2001: "Seasonal evolution of the mixed layer in the Subantarctic Zone south of Australia." *J. Geophys. Res., 106,* 31447-31462.

Roemmich, D., S. Riser, R. Davis, and Y. Desaubies, 2004: "Autonomous profiling floats: Workhorse for broad-scale ocean observations." *Marine Technol. Soc. J., 38,* 21-29.

Rudnick, D. L., and R. Ferrari, 1999: "Compensation of horizontal temperature and salinity gradients in the ocean mixed layer." *Science, 283,* 526-529.

Rudnick, D. L., and J. P. Martin, 2002: "On the horizontal density ratio in the upper ocean." *Dyn. Atmos. Oceans, 36,* 3-21.

Rudnick, D. L., T. J. Boyd, R. E. Brainard, G. S. Carter, G. D. Egbert, M. C. Gregg, P. E. Holloway, J. M. Klymak, E. Kunze, C. M. Lee, M. D. Levine, D. S. Luther, J. P. Martin, M. A. Merrifield, J. N. Moum, J. D. Nash, R. Pinkel, L. Rainville, and T. B. Sanford, 2003: "From tides to mixing along the Hawaiian ridge." *Science, 301,* 355-357.

Rudnick, D. L., R. E. Davis, C. C. Eriksen, D. M. Fratantoni, and M. J. Perry, 2004: "Underwater gliders for ocean research." *Mar. Technol. Soc. J., 38,* 73-84.

Rudnick, D. L., and J. Klinke, 2007: "The underway conductivity-temperature-depth instrument." *J. Atmos. Oceanic Technol., 24,* 1910-1923.

Rudnick, D. L., and S. T. Cole, 2010: "On sampling the ocean using underwater gliders." *In preparation.*

Samelson, R. M., and C. A. Paulson, 1988: "Towed thermistor chain observations of fronts in the subtropical North Pacific." *J. Geophys. Res., 93,* 2237-2246.

Schmitt, R. W., 1981: "Form of the temperature-salinity relationship in the central water: Evidence for double-diffusive mixing." *J. Phys. Oceanogr., 11,* 1015-1026.

Schmitt, R. W., 1990: "On the density ratio balance in the central water." *J. Phys. Oceanogr., 20,* 900-906.

Schmitt, R. W., 1994: "Double diffusion in oceanography." *Annu. Rev. Fluid Mech., 26,* 255-285.

Sherman, J., R. E. Davis, W. B. Owens, and J. Valdes, 2001: "The autonomous underwater glider 'Spray'." *IEEE J. of Ocean Eng., 26,* 437-446.

Siegel, D. A., and T. D. Dickey, 1987: "On the parameterization of irradiance for open ocean photoprocesses." *J. Geophys. Res., 92,* 14648-14662.

Sprintall, J. and D. Roemmich, 1999: "Characterizing the structure of the surface layer in the Pacific Ocean." *J. Geophys. Res., 104,* 23297-23311.

Sprintall, J., 2003: "Seasonal to interannual upper-ocean variability in the Drake passage." *J. Mar. Res., 61,* 27-57.

Stammer, D., and C. Wunsch, 1999: "Temporal changes in eddy energy of the oceans." *Deep Sea Res., 46,* 77-108.

Stammer, D., S. Park, A. Kohl, R. Lukas, and F. Santiago-Mandujano, 2008: "Causes for large-scale hydrographic changes at the Hawaiian Ocean Time Series station." *J. Phys. Oceanogr., 38,* 1931-1948.

St. Laurent, L., S. Stringer, C. Garrett, D. Perrault-Joncas, 2003: "The generation of internal tides at abrupt topography." *Deep-Sea Res., 50,* 987-1003.

Strass, V. H., 1992: "Chlorophyll patchiness caused by mesoscale upwelling at fronts." *Deep Sea Res., 39,* 75-96.

Strass, V. H., H. Leach, and J. D. Woods, 1992: "On the seasonal development of mesoscale variability: the influence of the seasonal pycnocline formation." *Deep Sea Res., 39,* 1627-1639.

Suga, T., K. Motoki, Y. Aoki, and A. Macdonald, 2004: "The North Pacific climatology of winter mixed layer and mode waters." *J. Phys. Oceanogr., 34,* 3-22.

Sundermeyer, M. A. and J. R. Ledwell, 2001: "Lateral dispersion over the continental shelf: Analysis of dye release experiments." *J. Geophys. Res., 106,* 9603-9621.

Sutherland, B. R., 1999: "Propagation and reflection of internal waves." *Phys. Fluids, 11,* 1081-1090.

Sutherland, B. R., G. O. Hughes, S. B. Dalziel, and P. F. Linden, 2000: "Internal waves revisited." *Dyn. Atmos. Oceans, 31,* 209-232.

Tabaei, A., T. R. Akylas, and K. G. Lamb, 2005: "Nonlinear effects in reflecting and colliding internal wave beams." *J. Fluid Mech., 526,* 217-243.

Talley, L. D., 1985: "Ventilation of the subtropical North Pacific: the shallow salinity minimum." *J. Phys. Oceanogr., 15,* 633-649.

Talley, L. D., and R. A. DeSzoeke, 1986: "Spatial fluctuations north of the Hawaiian

Ridge." *J. Phys. Oceanogr., 16,* 981-984.

Talley, L. D., 1993: "Distribution and formation of North Pacific intermediate water." *J. Phys. Oceanogr., 23,* 517-537.

Thorpe, S. A., 1998: "Nonlinear reflection of internal waves at a density discontinuity at the base of the mixed layer." *J. Phys. Oceanogr., 28,* 1853-1860.

Todd, R. E., D. L. Rudnick, M. R. Mazloff, R. E. Davis, and B. D. Cornuelle, 2010: "Poleward flows in the southern California Current System: Glider observations and numerical simulation." *J. Geophys. Res.,* submitted.

Toole, J. M., R. W. Schmitt, K. L. Polzin, and E. Kunze, 1997: "Near-boundary mixing above the flanks of a midlatitude seamount." *J. Geophys. Res., 102,* 947-959.

Veronis, G., 1972: "Properties of seawater defined by temperature, salinity, and pressure." *J. Mar. Res., 30,* 227-255.

Warner, M. J., J. L. Bullister, D. P. Wisegarver, R. H. Gammon, and R. F. Weiss, 1996: "Basin-wide distributions of chlorofluorocarbons CFC-11 and CFC-12 in the North Pacific: 1985-1989." *J. Geophys. Res., 101,* 20525-20542.

Watanabe, Y. W., K. Horada, and K. Ishikawa, 1994: "Chlorofluorocarbons in the central North Pacific and southward spreading time of North Pacific intermediate water." *J. Geophys. Res., 99,* 25195-25213.

Weller, R. A., 1991: "Overview of the frontal air-sea interaction experiment (FASINEX): A study of air-sea interaction in a region of strong oceanic gradients." *J. Geophys. Res., 96,* 8501-8516.

White, W. B., K. Hasunuma, and H. Solomon, 1978: "Large-scale seasonal and secular variability of the subtropical front in the western North Pacific from 1954 to 1974." *J. Geophys. Res., 83,* 4531-4544.

Wong, A. P. S., and G. C. Johnson, 2003: "South Pacific eastern subtropical mode water." *J. Phys. Oceanogr., 33,* 1493-1509.

Worcester, P. F., and R. C. Spindel, 2005: "North Pacific Acoustic Laboratory." *J. Acoust. Soc. Am., 117,* 1499-1510.

Wunsch, C., and R. Ferrari, 2004: "Vertical mixing, energy, and the general circulation of the oceans." *Annu. Rev. Fluid Mech., 36,* 281-314.

Young, W. R., 1994: "The subinertial mixed layer approximation." *J. Phys. Oceanogr., 24,* 1812-1826.

Young, W. R., and L. Chen, 1995: "Baroclinic instability and thermohaline gradient alignment in the mixed layer." *J. Phys. Oceanogr., 25,* 3172-3185.

Yuan, X., and L. D. Talley, 1992: "Shallow salinity minima in the North Pacific." *J. Phys. Oceanogr., 22*, 1302-1316.

Zaron, E. D., and G. D. Egbert, 2006: "Estimating open-ocean barotropic tidal dissipation: The Hawaiian Ridge." *J. Phys. Oceanogr., 36,* 1019-1035.